Title

Gigavolt-per-Meter Wakefields in Annular Dielectric Structures

Author

O'Shea, Brendan Donald

Publication Date

2014

University of California
Los Angeles

Gigavolt-per-Meter Wakefields in Annular Dielectric Structures

A dissertation submitted in partial satisfaction
of the requirements for the degree
Doctor of Philosophy in Physics

by

Brendan Donald O'Shea

2014

Abstract of the Dissertation

Gigavolt-per-Meter Wakefields in Annular Dielectric Structures

by

Brendan Donald O'Shea

Doctor of Philosophy in Physics

University of California, Los Angeles, 2014

Professor James B. Rosenzweig, Chair

A wakefield accelerator uses a medium capable of sustaining appropriate electric fields to transfer energy from a drive beam to a witness beam. Examples of such systems include electron beam driven plasma wakefields [1, 2], laser driven plasma wakefields [3] and electron beam driven dielectric wakefield structures [4, 5, 6]. Dielectrics and plasmas are of particular interest because they are capable of maintaining electric fields on the order of GVm^{-1} and in the case of plasmas upwards of TVm^{-1} [7]. These systems provide a significant step beyond current radiofrequency accelerating structures capable of peak electric fields on the order of 100 MVm^{-1} and average effective electric fields of 20 MVm^{-1} [8]. Furthermore, beam driven dielectric structures produce a wakefield which is phase synchronous with the beam, these structures do not suffer from transit time or dephasing effects [9, 10]. In the case of dielectric wakefield accelerators, the structures under study in this publication, the modes generated by the driving beam are in the terahertz (THz) regime. Thus development of dielectric wakefield accelerators is seen as a path to smaller, more compact accelerating systems and as a means to generate THz radiation [11]. Here we demonstrate a beam-driven dielectric wakefield accelerating structure that produces sustained fields of 1.35 GVm^{-1} for many hundreds of thousands of drive beam pulses. In addition we show beam-driven dielectric structures have the potential to produce single mode, high spectral purity THZ radiation of unprecedented energy scale.

The dissertation of Brendan Donald O'Shea is approved.

Pietro Musumeci

Russel E. Caflisch

George J. Morales

James B. Rosenzweig, Committee Chair

University of California, Los Angeles

2014

To my parents and their unwavering support.

Table of Contents

List of Figures

List of Tables

ACKNOWLEDGMENTS

After more than a decade at UCLA in one capacity or another there are perhaps too many people to acknowledge. I reiterate my endless gratitude to my parents for their untiring support of my educational pursuits. Committing more than 10 years to the pursuit of a degree is a daunting task and I couldn't have made it through the ups and downs without them.

I must thank my fellow students and coworkers, but specifically Joe, Josh, Kristin, Erik, Ago, Gabe, Evan, Alan and Joel. Some much more senior than others. Some long gone. Each one critical to helping me advance as the years passed. Often through constructive criticism and more often through commiseration. I can't forget Harry, Craig, Ernie and everyone in the UCLA machine shop and Knudsen Facilities for making life easier.

Oliver, Sam and Gerard, who spend hours talking about important things and unimportant things, and for what seemed like days with me in the tunnels at FACET and ATF making very small adjustments to very sensitive equipment.

To my longtime officemate Josh for putting up with my eccentricities and for hundreds of fruitful conversations. For your ability to shrug off my hopeless babbling when I was bored and to provide the punctuated distraction necessary to keep running the marathon which is graduate school. This section must include Josh's advisor Pietro who has, perhaps unintentionally, taught me to be more confident.

To my brother Finn who I feel infinitely closer to after the shared experience of graduate school. Who, in excess of my parents, has provided support and the wise advice of someone who has already travelled the route to a PhD.

Sine qua non, my advisor Jamie.

VITA

2004–2005	Student Researcher, Particle Beam Physics Lab, University of California, Los Angeles.
2005	B.S. (Physics), University of California, Los Angeles.
2005–2007	Engineer III, Particle Beam Physics Lab, University of California, Los Angeles.
2008	M.S. (Physics), University of California, Los Angeles.
2007–2014	Graduate Student Researcher, Particle Beam Physics Lab University of California, Los Angeles.

PUBLICATIONS

Measurement of Self-Shaped Ellipsoidal Bunches from a Photoinjector with Post Acceleration
B. O'Shea, J.B. Rosenzweig, G. Asova, J. Bhr, M. Hnel, Y. Ivanisenko, M. Khojoyan, M. Krasilnikov, L. Staykov, F Stephan, J. Rnsch-Schulenburg
Phys. Rev. ST Accel. Beams 14, 012801

Transformer Ratio Improvement for Beam Based Plasma Accelerators
B. O'Shea, J. Rosenzweig, S. Barber, A. Fukasawa, O, Williams, P. Muggli, V. Yakimenko, K. Kusche

AIP Conference Proceedings of the 2012 Advanced Accelerator Conference, Austin, TX USA. 12/2012; 1507(1)

Demonstration of Gigavolt-per-meter Accelerating Gradients using Cylindrical Dielectric-lined Waveguides
B.D. O'Shea, G. Andonian, K.L. Fitzmorris, S.Hakimi, J. Harrison, J.B. Rosenzweig, O. Williams, M.J. Hogan, V. Yakimenko
Proceedings of the 2014 International Particle Accelerator Conference, Dresden, Germany

Observation of GV/M Decelerating Fields in Dielectric Lined Waveguides
B.D. O'Shea, G. Andonian, K.L. Fitzmorris, S.Hakimi, J. Harrison, J.B. Rosenzweig, O. Williams, M.J. Hogan, V. Yakimenko
Proceedings of the 2014 Linear Accelerator Conference, Geneva, Switzerland

Double Resonant Plasma Wakefields
B.D. O'Shea, A. Fukasawa, J.B. Rosenzweig, B Hidding, D.L. Bruhwiler
Proceedings of the 2011 International Particle Accelerator Conference, San Sebastian, Spain

Measurement of the UCLA/URLS/INFN Hybrid Gun
B. O'Shea, A. Boni, A. Fukasawa, J.B. Rosenzweig, D. Alesini, M. Ferrario, B. Spataro, L. Ficcadenti, A. Mostacci, L. Palumbo
Particle Accelerator Conference, 2007. PAC. IEEE; 07/2007

CHAPTER 1

Introduction

The cost and size of colliders has become a serious impediment to performing future high-energy particle experiments. This point is most obviously demonstrated by the ubiquitous Livingston plot [12] shown in Figure 1.1. This plot shows a bending, and eventual plateau, of the maximum beam energy of accelerating systems as a function of time. This bending of the maximum beam energy is unsurprisingly correlated with a distinct lack of new accelerating systems since the radio-frequency (RF) structure developed at Stanford in the 1940s [13].

An increase in beam energy after the initial introduction of RF cavities can be attributed to the increase in accelerator size and improvements in technologies associated with RF structures, such as klystrons. As the field matured the rate at which improvements to RF systems could be made naturally declined. With innovation stalled the only method for building higher energy machines is to build bigger machines. This leads to a synchrotron of 27 kilometer circumference known as the Large Hadron Collider.

The ultimate desire for such high beam energy machines is to study the nature of particles at a fundamental level. The advantage of ring based machines is rooted in the fact that a beam passes the same location multiple times. This allows a relatively low gradient cavity to accelerate a beam to very high energies. A one meter structure which is passed through a million times gives the experimenter, effectively, a 1000 kilometer accelerator. This works well for

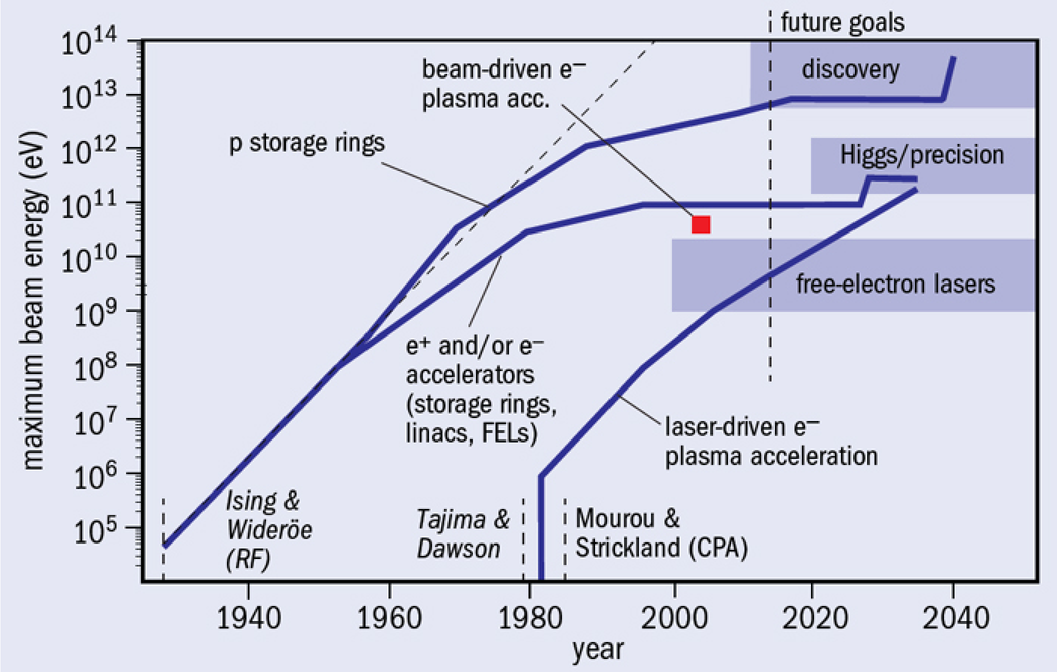

Figure 1.1: A Livingston plot showing the increase in beam energy as a function of time. Initially the beam energy of accelerators world wide is seen to double every 10 years. Current trends have been unable to keep this pace.

hadrons but limitations due to synchrotron radiation, which is inversely proportional to 1/mass^4 [14], make high energy electron rings unfeasible. This means that scientists are stuck accelerating and colliding relatively large non-elementary particles, such as protons. Collisions of particles which are not elementary result in complicated showers of constituent particles which obscure the measurement of interest. Thusly, the lack of increase in functional gradient of accelerating systems has shifted the high-energy particle physics world to use of machines which are able to access the beam energies necessary for new discoveries, but at the cost of messy collisions.

The ideal situation involves the collision of elementary particles such as electrons and positrons. At present, due to bending (or synchrotron) radiation the only way to effectively accelerate electrons and positrons is through linear accelerators, such as the three kilometer linac at the SLAC National Laboratory, the 48 km linac at the proposed Compact Linear Collider (CLIC) facility [15] and the 31 km linac at the proposed International Linear Collider (ILC) [16]. The average gradient in the RF structures used at SLAC is on the order of 20 $\mathrm{MVm^{-1}}$ [17, 18]. Assuming, arguendo, that no other systems are needed to contain the beam or focus it for the collision, in order to reach 1 a TeV collider it would be necessary to use 50 kilometers of RF structures. At 22k$ per meter [19], the cost of building a TeV collider using conventional RF technologies exceeds a trillion dollars. A less theoretical estimate of the cost of linear colliders is provided by the CLIC Conceptual Design Report [15] which estimates 10 billion U.S. dollars for a 500 GeV center of mass collider. The cost savings are based on the structures pushing to higher frequencies and gradients on the order of 100 $\mathrm{MVm^{-1}}$ but also on the use of a novel two-beam-acceleration scheme. Even so, such sticker prices understandably give funding agencies pause.

In addition to colliders, accelerators are increasingly used as particle beam sources that are later used in radiation sources such as Free-Electron Lasers (FEL) [20]. An example of which is the Linac Coherent Light Source at SLAC National Laboratory [21]. Such light sources are key to structure determination of macromolecules via coherent x-rays [22]. Other accelerator-FEL based sources in operation include FLASH in Hamburg, Germany [23] and an Energy Recovery Linac (ERL) at Jefferson Lab [24]. The former provides coherent light in the difficult to access Extreme Ultraviolet (EUV) region of 14 nm while the latter is a demonstration of Superconducting Radio-Frequency (SRF) technology and its use in FEL sources. The structures used as accelerators in this thesis can also be used as radiators as long as the wakefield in the structure is collected. As will be outlined in future sections of this work, selection of the geometric properties of the structure allows selection of the wavelength of interest, including radiation of unprecedented energy scales in the terahertz regime [25].

To overcome cost and size limits of future accelerators it is necessary to develop accelerating systems with gradients well in excess of the 20 MVm^{-1} present in RF technologies. A class of accelerators under study for use as future accelerators are known as wakefield accelerators. Such systems are configured in a "drive-witness" modality which takes advantage of the fact that a system which accelerates a beam is also capable of decelerating a beam. The term drive-witness is used to describe the situation in which one beam, the drive beam, is sent through a wakefield structure and gives up energy to that structure. This loss of energy is converted into a wakefield in the structure which a second beam, the witness, then absorbs.

While there are several options available for use as wakefield accelerators the work presented here focuses on the use of dielectric lined waveguides. These structures have shown remarkable ability to sustain fields up to $\approx$5 GVm^{-1} [26]. Fields of even one GVm^{-1} would be able to produce TeV electrons in a kilometer. This continues the assumption stated earlier that no other elements are necessary for transporting the beam. Such assumptions for nascent technologies are shaky but necessary as the difficulties involved in bringing a new technology to the maturity required to build a collider are never easy to see. It isn't until a detailed in-lab characterization and measurement of the physics in question that the proverbial devil in the details shows himself. This thesis is presented as a step in the direction of characterization of dielectric lined waveguides as an accelerating platform. Specifically we show that gradients in excess of GVm^{-1} are obtainable and sustainable.

We begin this work with a short overview of beam physics to acquaint the reader with the notation and terminology of the author. In chapter 3 we then move on to a discussion of radiation sources present in an accelerator environment and their associated uses. Chapter 4 reviews some concepts particular to wakefield accelerators. In chapter 5 we present the specifics of a dielectric based accelerator and solve for the modes and coupling of a beam-dielectric lined waveguide system. Chapter 6 presents the experiments that were conducted at the SLAC National Accelerator Laboratory and their results and relation to the previously derived theory. Chapter 7 is a summary and conclusion of the work presented here as well as future work and open questions remaining before a dielectric lined waveguide can be seriously considered a collider ready technology.

CHAPTER 2

Beam Dynamics

The design of charged particle accelerators begins with the definition of a coordinate system which reduces what can be a very complicated system in cartesian coordinates to a curvilinear system which moves along the accelerator with the so-called "design particle". This design particle is the ideal path through the accelerator, whether start to finish in a linear accelerator or repeatedly around the ring in a synchrotron. This system is useful when the accelerating system has been designed well enough such that one would expect that particles that do deviate from the design orbit do not do so drastically. As such, we are interested primarily in a set of equations which define the motion of bunches of particles through an accelerator which account only for small deviations from the design particle. This will lead us first to design a coordinate system which follows the beam along the accelerator and then to derive concomitant equations of motion in that system. The equations of motion are later written in such away that vanishingly small terms can be neglected. After writing down a suitably culled system of equations we will then transform them into a matrix notation that allows us to more easily analyze the effect of accelerator subsections such as focusing lattices or bending magnets.

2.1 Design Particle

When an accelerator is designed the goal is to connect a particle source to devices that do something with the particles produced; such as a detector or a focusing channel that directs the electrons at a tumor in a patient or at another bunch of particles in a collider. The "design particle" is used to outline the perfect path from the source to the application. It is supposed to have a precisely known position and momentum and is at all times locked to the design orbit. What this means is, for the design particle on the design orbit, no focusing optics or other beam control methods are necessary except those that steer the design particle along the design orbit to the location we desire.

With the Lorentz Force equation, Eq. 2.1, we readily see two methods for bending a single particle, an electric field $\vec{E}$ or magnetic induction $\vec{B}$[1]. For particles close to the speed of light Eq. 2.1 shows that $\vec{E}$ and $\vec{B}$ are equivalent. The conversion between the two is such that $1\ T = 3 * 10^8\ Vm^{-1}$. While 1 Tesla magnetic fields are easily created using present technology, 300 MVm^{-1} is only now becoming possible to create and at much greater expense [27, 28, 29]. Because of this we rely heavily on magnetic fields to steer the design particle and we would like to develop a system of equations equally suited to straight lines and bends. We begin by examining the motion of the design particle in a uniform magnetic field.

2.2 Particle in a Uniform Magnetic Field

$$\vec{F} = \frac{d\vec{p}}{dt} = q(\vec{E} + \frac{\vec{v}}{c} \times \vec{B}) \tag{2.1}$$

---

[1] Where choice of units is concerned, the author prefers to work in Gaussian while the literature prefers SI. This will lead to equations worked in Gaussian but individual quantities quoted in SI.

$$\frac{dE}{dt} = \frac{d}{dt}\gamma mc^2 = \vec{v} \cdot \vec{F} \tag{2.2}$$

We begin by supposing a system in which a particle at time $t = 0$ with initial velocity $\vec{v}(t = 0) = \vec{v_0} = \{0, 0, v_0\}$ is moving in a magnetic induction $\vec{B} = \{0, B_0, 0\}$ which is uniform in space and unchanging in time. Immediately from Eq. 2.1 and Eq. 2.2 it can be seen that particles in uniform magnetic fields do not gain energy and that the particle will be locked to the $\hat{x}\hat{z}$-plane; there is no force, F_y, in the $\hat{y}$ direction. We then write down the equations of motion for the design particle in the uniform magnetic field:

$$F_x = \gamma m_e \frac{dv_x}{dt} = \frac{ev_z B_0}{c}, \quad F_z = \gamma m_e \frac{dv_z}{dt} = \frac{ev_x B_0}{c}. \tag{2.3}$$

Taking the time derivative of both equations and substituting for $\dot{v}_x$ and $\dot{v}_z$ using Eqs. 2.3, we arrive at:

$$\frac{d^2 v_x}{dt^2} = -\left(\frac{eB_0}{\gamma m_e c}\right)^2 v_x, \quad \frac{d^2 v_z}{dt^2} = -\left(\frac{eB_0}{\gamma m_e c}\right)^2 v_z, \tag{2.4}$$

where we are now free to define the cyclotron frequency as $\Omega_0 \equiv \frac{eB_0}{\gamma m_e c}$ and write the solutions to these differential equations as:

$$v_x(t) = A\sin(\Omega_0 t) + B\cos(\Omega_0 t), \quad v_z(t) = C\sin(\Omega_0 t) + D\cos(\Omega_0 t). \tag{2.5}$$

Using the initial velocity as stated above $B = 0,\ D = v_0$ and the final coefficients can be found by noting that there is no energy gain, $\frac{d|v|}{dt} = 0$, leading to $A = v_0,\ C = 0$ and

$$v_x(t) = v_0 \sin(\Omega_0 t), \quad v_z(t) = v_0 \cos(\Omega_0 t). \tag{2.6}$$

Integrating these equations in time and defining the initial position of the particle to be the origin leads to the location of the design particle as a function of time:

$$x(t) = -\frac{v_0}{\Omega_0}\cos(\Omega_0 t) + \frac{v_0}{\Omega_0}, \quad z(t) = \frac{v_0}{\Omega_0}\sin(\Omega_0 t), \tag{2.7}$$

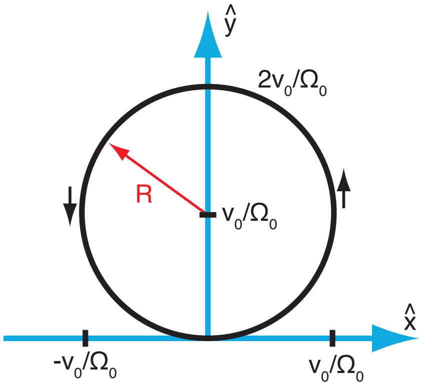

Figure 2.1: The path of a particle in a uniform magnetic induction field.

which is plotted in Fig. 2.1. The key feature of the design particle's motion in a uniform magnetic field is its radius of curvature $R = \frac{v_0}{\Omega_0} = \frac{\gamma m_e c v_0}{e B_0}$, which leads us to construct a curvilinear coordinate system similar to a cylindrical polar coordinate system [30].

2.3 A Curvilinear Coordinate System for Accelerators

With the design trajectory known we are interested in what happens to particles that follow this trajectory, but not perfectly. We need a coordinate system which keeps track of deviations from the design trajectory without the mess of a fixed origin. The previous discussion indicates that a system capable of bends and straight lines should do well. We restricted the scope of the previous design trajectory discussion to the xz-plane since traditionally linacs and circular machines are flat. This system is sometimes referred to as the "beam frame" but it is not to be confused with a relativistic boost.

We implement a system as shown in Fig. 2.2 where the new coordinate system is outlined in blue. In this system, a deviation in the xz-plane of a particle from the design radius of curvature R, away from the center of curvature, is in the $\hat{x}$

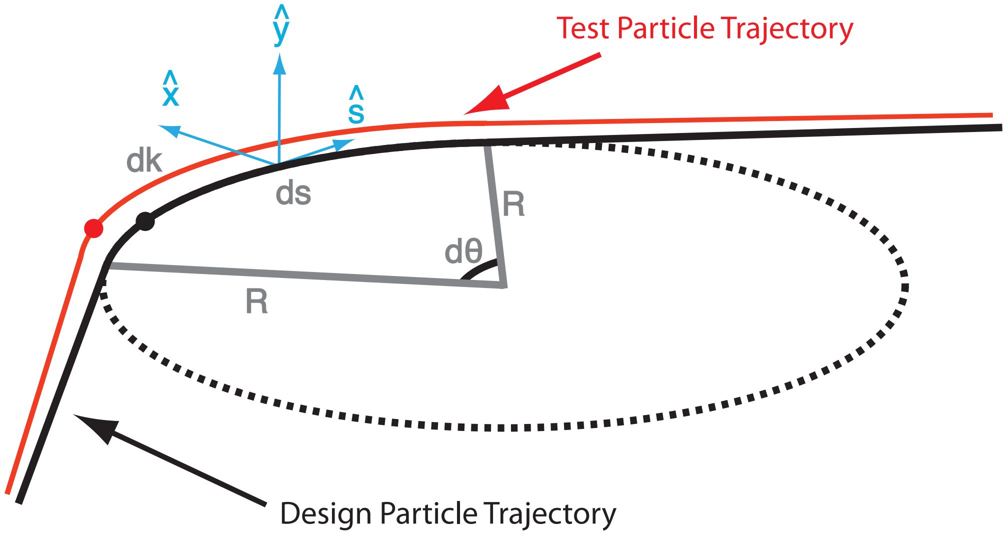

Figure 2.2: The design particle trajectory (black) with the accelerator curvilinear coordinate system (light blue) and a possible real beam particle trajectory (red).

direction. We have also chosen the the direction of motion of the design particle to be the $\hat{s}$ direction, this clears up possible confusion with a traditional cartesian coordinate system. The restriction of the problem to the xz-plane leaves the $\hat{y}$ direction, perpendicular to the plane of the bend, unchanged.

We start by defining the cartesian coordinates in terms of the the new parameters and derive expressions for infinitesimal steps ds_i in our new coordinate system:

$$z_c = (x + R)cos(\theta), \quad x_c = (x + R)sin(\theta), \quad y_c = y, \tag{2.8}$$

where the subscript c represents cartesian. It is then necessary to compute the Lamé coefficients as derived from the metric of the new coordinate system [30]:

$$h_i = \sqrt{g_{ii}} = \sqrt{\sum_L \left(\frac{\partial x_L}{\partial x_i}\right)^2} \ ; \ x_L \in x_c, y_c, z_c; \tag{2.9}$$

$$h_x = 1, \quad h_y = 1, \quad h_\theta = (x + R). \tag{2.10}$$

We are then able to write the differential elements of the new coordinate system, $ds_i = h_i dx_i$, and the total differential element $d\vec{r}$ as:

$$ds_x = dx, ds_y = dy, ds_\theta = (x+R)d\theta \tag{2.11}$$

$$d\vec{r} = dx\hat{x} + dy\hat{y} + (x+R)d\theta\hat{s}. \tag{2.12}$$

Electing now to use the design particle's progress along the arc, $s = R\theta$, as opposed to its angular progression θ we arrive at an appropriate differential element for our coordinate system:

$$d\vec{r} = dx\hat{x} + dy\hat{y} + (1+\frac{x}{R})ds\hat{s}. \tag{2.13}$$

The preceding differential, $d\vec{r}$, and the Lamé coefficients provide the tools necessary to analyze a beam moving in the beam frame. It is useful to note at this point that a particle moving in a straight line has an infinite radius of curvature, $R = \infty$, which reduces Eq. 2.13 to a standard cartesian right handed coordinate system. Finally we write down the gradient, divergence and Laplacian in the new coordinate system:

$$\vec{\nabla}\psi = \sum_i \hat{x_i}\frac{1}{h_i}\frac{\partial\psi}{\partial x_i} \tag{2.14}$$

$$\vec{\nabla}\cdot\vec{V} = \frac{1}{1+hx}\left[\frac{\partial}{\partial x}([1+hx]V_x) + \frac{\partial}{\partial y}([1+hx]V_y) + \frac{\partial}{\partial s}(V_s)\right] \tag{2.15}$$

$$\vec{\nabla}\cdot\vec{\nabla}\psi = \frac{1}{1+hx}\left[\frac{\partial}{\partial x}\left((1+hx)\frac{\partial\psi}{\partial x}\right) + (1+hx)\frac{\partial^2\psi}{\partial y^2} + \frac{\partial}{\partial s}\left(\frac{1}{1+hx}\frac{\partial\psi}{\partial s}\right)\right], \tag{2.16}$$

where we have used the relation $h = 1/R$.

2.4 Equations of Motion

The accelerator coordinate system we have just developed is a rotating coordinate system ($R \neq 0$) which means that equations like the Lorentz force equation, when

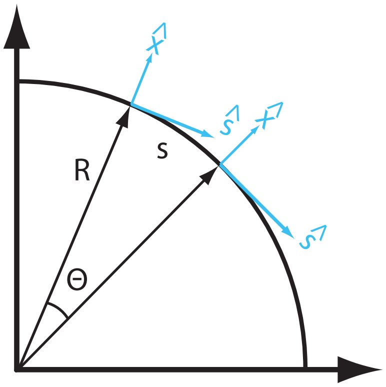

Figure 2.3: The rotation of the unit vectors of the curvilinear coordinate system. The black line is the reference trajectory, the blue lines represent the local curvilinear coordinate system at two points during a bend of radius R.

transformed to this new system, show the effects of fictitious forces. We would like to express the equations of motion in a manner that makes these forces transparent and easily ignored for the case of straight (non-bending) sections of beam line. This is particularly useful when one considers that even ostensibly circular machines are realized using straight sections connected by short, shallow bends. In addition, we wish to transform the aforementioned equations of motion from a system dependent on time t to a system dependent on a parameter that describes the beam's current position in the accelerator, s.

We begin by working out the transformation of the unit vectors $\hat{x}$ and $\hat{s}$ and use these to write down the position of a particle in the beam frame. We then convert the particle's velocity and acceleration, $\dot{\vec{r}}$ and $\ddot{\vec{r}}$, to expressions dependent on the reference particle position s, instead of t. Finally, we convert the Lorentz Force equation, Eq. 2.1, using the previously derived relations, to the new coordinate system including s dependence.

As can be seen in Figure 2.3, as time evolves the accelerator coordinate system will rotate as $ds/dt = v_0$, taking the unit vectors with it. The transformation of these unit vectors can be derived as follows:

$$\dot{\hat{s}} = \frac{d\hat{s}}{dt} = \frac{d\hat{s}}{d\theta}\frac{d\theta}{dt} = -\hat{x}\left(\frac{d}{dt}\frac{s}{R}\right) = -\frac{v_0\hat{x}}{R}, \quad \dot{\hat{x}} = \frac{v_0\hat{s}}{R}. \tag{2.17}$$

An individual particle's position in the beam frame can be written in terms of its absolute position $\vec{r}$ and the position of the reference frame $\vec{r_0}$:

$$\vec{r} - \vec{r_0} = x\hat{x} + y\hat{y} + z\hat{s}, \tag{2.18}$$

where z is used to denote the longitudinal offset, in the beam frame, of the particle of interest from the design particle. By definition all motion of the reference particle is in the $\hat{s}$-direction, giving $d\vec{r_0} = ds\ \hat{s}$ and $\dot{\vec{r_0}} = v_0\ \hat{s}$. The time derivative of the equation for the particle's beam frame position, Eq. 2.18, gives its beam frame velocity as:

$$\dot{\vec{r}} = \dot{\vec{r_0}} + \dot{x}\hat{x} + x\frac{v_0}{R}\hat{s} + \dot{y}\hat{y} + \dot{z}\hat{s} - z\frac{v_0}{R}\hat{x} \tag{2.19}$$

$$\dot{\vec{r}} = \left(\dot{x} - z\frac{v_0}{R}\right)\hat{x} + \dot{y}\hat{y} + \left(1 + \frac{x}{R} + \frac{\dot{z}}{v_0}\right)v_0\hat{s}. \tag{2.20}$$

Use of the chain rule to define the time derivative in terms of the reference particle's position in the accelerator gives:

$$\dot{x} = \frac{dx}{dt} = \frac{dx}{ds}\frac{ds}{dt} = v_0 x', \tag{2.21}$$

where we use the notation $\frac{d}{ds} = ()'$ as we are more interested in the evolution of the beam along the accelerator as opposed to as a function of time. Transforming a particle's velocity, Eq. 2.20, to a system dependent on s instead of t, by using Eq. 2.21 yields:

$$\vec{v} = \dot{\vec{r}} = \left(x' - \frac{z}{R}\right)v_0\hat{x} + y'v_0\hat{y} + \left(1 + \frac{x}{R} + z'\right)v_0\hat{s}. \tag{2.22}$$

Similarly the acceleration of a particle can be derived as:

$$\begin{aligned}
\frac{\dot{v}_x}{v_0^2} &= x'' - \frac{2z'}{R} - z\left(\frac{1}{R}\right)' - \frac{x}{R^2} - \frac{1}{R} \\
\frac{\dot{v}_y}{v_0^2} &= y'' \\
\frac{\dot{v}_z}{v_0^2} &= z'' - \frac{2x'}{R} - x\left(\frac{1}{R}\right)' - \frac{z}{R^2},
\end{aligned} \tag{2.23}$$

where the terms dependent on $\ddot{s}$ have been omitted as we have assumed a system without energy gain, $\dot{\gamma} = 0$.

The Lorentz Force equation is now written in terms of the above derived velocity and acceleration, in the accelerator curvilinear coordinate system and with the beam position coordinate s in place of time:

$$\frac{d\vec{p}}{dt} = \gamma m_e \dot{\vec{v}} = q\left(\frac{\vec{v}}{c} \times \vec{B}\right) \tag{2.24}$$

$$\begin{aligned}
\dot{v}_x &= \frac{q}{\gamma m_e c}\left(v_y B_z - v_z B_y\right) \\
\dot{v}_y &= -\frac{q}{\gamma m_e c}\left(v_x B_z - v_z B_x\right) \\
\dot{v}_z &= \frac{q}{\gamma m_e c}\left(v_x B_y - v_y B_x\right).
\end{aligned} \tag{2.25}$$

Direct substitution of Eqs. 2.22 and 2.23 leads to:

$$\begin{aligned}
x'' - \frac{2z'}{R} - z\left(\frac{1}{R}\right)' - \frac{x}{R^2} - \frac{1}{R} &= \frac{q}{\gamma m_e c v_0}\left(y' B_z - (1 + \frac{x}{R} + z')B_y)\right) \\
y'' &= -\frac{q}{\gamma m_e c v_0}\left((x' - \frac{z}{R})B_z - (1 + \frac{x}{R} + z')B_x\right) \\
z'' + \frac{2x'}{R} + x\left(\frac{1}{R}\right)' - \frac{z}{R^2} &= \frac{q}{\gamma m_e c v_0}\left((x' - \frac{z}{R})B_y - y' B_x\right).
\end{aligned} \tag{2.26}$$

2.5 Expansion of the Equations of Motion

The equations of motion of a particle in the accelerator curvilinear coordinate system, Eqs. 2.26, represent an exact description of a test particle's motion.

When building or modeling an accelerator the designer starts with a linearized version of these equations and moves to higher order effects as necessary. The nature of beams as a collection of particles which have small deviations from the design orbit validates this method of system modeling.

We begin by performing an expansion of the magnetic field in terms of the beam frame coordinates. We then proceed to expand γ, and other quantities containing γ, in terms of the beam frame coordinates and the momentum deviation δ. Finally the two are combined, the expansions and the equations of motion derived above, and by collecting terms of similar order the linearized equations of motion are derived.

2.5.1 Multipole Expansion of the B-Field

Excepting the charge of the beam itself and instances of exotic focusing schemes, such as plasma lenses [31], the region in which the beam passes is source free. If we assume a region of static magnetic field, free of electric field, it is possible to write Ampères law and the divergence of $\vec{B}$ as:

$$\nabla \times \vec{B} = -\nabla \times \nabla \phi_B \equiv 0, \quad \nabla \cdot \vec{B} = 0, -\nabla \cdot \nabla \phi_B = 0, \tag{2.27}$$

in terms of a potential $B = -\nabla \phi_B$.

Before solving the above equation, using the Laplacian as defined for this coordinate system Eq. 2.16, it is important to note that we wish a system in which the beam stays in the xs-plane. This demand means that $\phi_B(x, y, s)$ must be an odd function of the y coordinate[2]. This restriction is not entirely obvious or necessary at this point, but neglecting it in lieu of later work only serves to

---

[2] Given the Lorentz force law, forces F_y will be proportional to B_x and B_z. The potential as defined to be odd in y means that $B_{x,z}(y) = -B_{x,z}(-y)$ so that forces F_y will always force particles offset in $\hat{y}$ back to the xz-plane.

obfuscate the following derivation and results in terms which result in undesirable $x - y$ plane coupling. In light of the above it is possible to define the magnetic potential ϕ_B as:

$$\phi_B(x, y, s) = \sum_{m=0}^{\infty}\sum_{n=0}^{\infty} A_{2m+1,n}(s)\frac{x^n}{n!}\frac{y^{2m+1}}{(2m+1)!}, \tag{2.28}$$

where the restriction of y to odd powers enforces our demand that ϕ_B be odd in y. When Eq. 2.28 is substituted into Eq. 2.16 the result is a recursion relation between the A coefficients:

$$\begin{gathered} A''_{2m+1,n} + hnA''_{2m+1,n-1} - nh'A'_{2m+1,n-1} + A_{2m+1,n+2} + \\ h(3n+1)A_{2m+1,n+1} + h^2n(3n-1)A_{2m+1,n} + h^3n(n-1)^2A_{2m+1,n-1} \\ + A_{2m+3,n} + 3hnA_{2m+3,n-1} + 3h^2n(n-1)A_{2m+3,n-2} + h^3n(n-1)(n-2)A_{2m+3,n-3} = 0. \end{gathered} \tag{2.29}$$

This recursion relation allows higher order A coefficients to be written in terms of lower order coefficients. The details of the preceding derivation can be found in the appendix, the only addendum to the above relation is that when attempting to derive a relation for particular values of m and n all coefficients with one or both indexes which are negative are to be set to zero.

While the present discussion focuses on linearizing the equations of motion, future discussions will mention magnets of higher order, so we shall keep ϕ_B terms up to 4^{th} order:

$$\begin{aligned} \phi_B \simeq \left(A_{1,0} + A_{1,1}x + A_{1,2}\frac{x^2}{2!} + A_{1,3}\frac{x^3}{3!} + \ldots\right)y + \\ \left(A_{3,0} + A_{3,1}x + \ldots\right)\frac{y^3}{3!} + \ldots. \end{aligned} \tag{2.30}$$

It is now possible to write the components of the magnetic field in terms of these

A coefficients, by taking the appropriate derivative:

$$\begin{aligned} B_x = -\frac{\partial \phi_B}{\partial x} &\simeq -\left(A_{1,1} + A_{1,2}x + A_{1,3}\frac{x^2}{2!}\right)y - \left(A_{3,1}\right)\frac{y^3}{3!} \\ B_y = -\frac{\partial \phi_B}{\partial y} &\simeq -\left(A_{1,0} + A_{1,1}x + A_{1,2}\frac{x^2}{2!} + A_{1,3}\frac{x^3}{3!}\right) - \left(A_{3,0} + A_{3,1}x\right)\frac{y^2}{2!} \\ B_z = -\frac{1}{1+hx}\frac{\partial \phi_B}{\partial s} &= -\frac{1}{1+hx}\left(A'_{1,0}y + A'_{1,1}xy + \ldots\right) \end{aligned} \tag{2.31}$$

With the expressions for the magnetic field in terms of the A coefficients and a recursion relation between all the coefficients it is necessary to derive an expression relating the A coefficients to a real $\vec{B}$ field. To do so we perform a Taylor expansion of the magnetic induction in the y=0 mid-plane:

$$B_y(x,0,s) \simeq B_y\Big|_{x=y=0} + \frac{\partial B_y}{\partial x}\Big|_{x=y=0} x + \frac{\partial^2 B_y}{\partial x^2}\Big|_{x=y=0}\frac{x^2}{2} + \ldots, \tag{2.32}$$

and compare with Eq. 2.31, leading to:

$$A_{1,0} = B_y(0,0,s), \quad A_{1,1} = \frac{\partial B_y}{\partial x}\Big|_{x=y=0}, \ldots, \quad A_{1,n} = \frac{\partial^n B_y}{\partial x^n}\Big|_{x=y=0}. \tag{2.33}$$

It is also possible and advantageous to write the magnetic induction $\vec{B}$ in terms of dimensionless coefficients, to be consistent with accelerator literature:

$$B_y(x,0,s) = B_0[1 - nhx + \beta h^2x^2 + \gamma h^3x^3 \ldots], \tag{2.34}$$

where the negative sign in front of the n is by convention. Using the previous three relationships, the A coefficients are now:

$$\begin{aligned} A_{1,0} &= B_y(x,0,s) = B_0, \\ A_{1,1} &= \frac{\partial B_y}{\partial x} = -nhB_0; \quad n = -\frac{1}{hB_0}\frac{\partial B_y}{\partial x}, \\ \frac{1}{2}A_{1,2} &= \frac{1}{2}\frac{\partial B_y}{\partial x} = \beta h^2 B_0; \quad \beta = \frac{1}{2h^2B_0}\frac{\partial^2 B_y}{\partial x^2}, \\ \frac{1}{3!}A_{1,3} &= \frac{\partial^3 B_y}{\partial x^3} = \gamma h^3 B_0; \quad \gamma = \frac{1}{3!h^3B_0}\frac{\partial^3 B_y}{\partial x^3}, \end{aligned} \tag{2.35}$$

to list but a few. With these relations available for reference, we can now write the linearized form of the magnetic field, Eq. 2.31 as:

$$\begin{aligned} B_x &= -nhB_0 y, \\ B_y &= B_0(1 - nhx), \\ B_z &= B_0' y. \end{aligned} \tag{2.36}$$

2.5.2 Expansion of Gamma

In performing the expansion of the equations of motion for a particle in a magnetic field, it will be necessary to account for particles with momentum which deviates from the design momentum. As with the case of a test particle's position relative to the design particle, we are most interested in a test particle's momentum deviation from design. Our formulation until now also indicates we are interested in momentum evolution as a function of beam position along the accelerator, as opposed to time.

Analysis of the vectorial deviation of a test particle's momentum from the design momentum shows, by nature of the design momentum being entirely in the $\hat{s}$-direction, that the normalized deviation is given by:

$$\vec{\delta p} = \frac{\vec{p} - p_0 \hat{s}}{p_0} = \frac{p_x}{p_0}\hat{x} + \frac{p_y}{p_0}\hat{y} + \frac{p_z - p_0}{p_0}\hat{s}, \tag{2.37}$$

where the design particle's momentum has been explicitly shown to be only in the $\hat{s}$ direction. Using the conversion described in Eq. 2.21 to change from a time dependent to s dependent system the individual components can be written:

$$\delta = \delta p_z = \frac{p_z - p_0}{p_0} = \frac{\gamma v_z}{\gamma_0 v_0} - 1 = \frac{\gamma}{\gamma_0}\left(1 + \frac{x}{R} + z'\right) - 1, \tag{2.38}$$

where Eq. 2.22 has been used for the velocity in the $\hat{s}$-direction, v_z. If we now solve Eq. 2.38 for γ_0/γ, expanding in the small parameter δ, it leads to:

$$\frac{\gamma_0}{\gamma} = \left(z' + \frac{x}{R} + 1\right)\frac{1}{1+\delta} \simeq \left(z' + \frac{x}{R} + 1\right)\left(1 - \delta + \delta^2 - \delta^3 + \ldots\right) \tag{2.39}$$

Particle beams are by definition collections of particles which do not deviate drastically from the design trajectory. This introduces an asymmetry in the way in which transverse momentum errors and longitudinal momentum errors are handled. The former is based on the assumption that any transverse momentum deviation is small compared to the longitudinal momentum. Stated another way this means that the change in transverse position of a particle as a function of the position in the accelerator s is given by:

$$\frac{p_x}{p_z} \simeq \frac{p_x}{p_0} = \frac{dx}{dt}\frac{dt}{ds} = x'. \tag{2.40}$$

Thus, the vector which makes up the relevant momentum parameters during beam transport is: $\{x', y', \delta\}$.

2.5.3 Expansion of the Equations of Motion

With the preceding expansions it is now straight forward to write down the linearized equations of motion, by combining Eqs. 2.26, 2.36 and 2.39, keeping only the terms linear in the coordinates, to obtain:

$$\begin{aligned} x'' + h^2(1-n)x &= h\delta, \\ y'' + nh^2 y &= 0, \\ z'' + hx' + h'x &= 0. \end{aligned} \tag{2.41}$$

Where we have dropped the $h'z$ term as it is effectively nonlinear. To phrase this another way, in order for this term to be relevant the gradient in the field, h', would have to be large compared to the length of the beam, which in practical situations is not true.

2.6 Solutions to the Linear Equations of Motion

We begin now to solve the linearized equations of motion derived in Eqs. 2.41. We do not take up the more general case of when n is a function of s, $n = n(s)$, which is a form of a Mathieu-Hill equation [29]. A complete survey of beam dynamics is well beyond the subject of this work. Instead we look at small sections of the accelerator for which n is not a function of s, so the solutions are those of a simple harmonic oscillator.

Assuming a beam of minimal energy spread ($\delta \simeq 0$) the first of Eqs. 2.41 can be written as

$$x'' + h^2(1-n)x = 0, \tag{2.42}$$

with solutions, for n $<$ 1,

$$\begin{aligned} x(s) &= x_0 \cos(h\sqrt{1-n}s) + \frac{x_0'}{h\sqrt{1-n}} \sin(h\sqrt{1-n}s), \\ x'(s) &= -h\sqrt{1-n}x_0 \sin(h\sqrt{1-n}s) + x_0' \cos(h\sqrt{1-n}s), \end{aligned} \tag{2.43}$$

where we have preemptively used the correct coefficients for initial conditions (x_0, x_0').

2.6.1 Matrix Formalism

If we are interested in a series of discrete sections of an accelerating system we would solve for the particle motion by using the result of the first section as the initial conditions for the next section. This method of propagating initial conditions through many discrete solutions can be represented through matrix formalism.

As an example we solve the equation of motion in the x direction, Eq. 2.42, for the case of a drift: $R \to \infty, n \to 0$. The solution can be found through integration where the constant of integration is x'_0, with the solution $x(s) = x'_0 s$. This conforms to what we might naively expect from applying simple ray tracing methods from optics. It is worth mentioning that this isn't a coincidence: this formalism is in fact identical to optical treatments which use ray tracing. Another example is the case of a simple quadrupole for which $1 - n \to n$, the solution to which is given in Eq. 2.43, when the substitution just outlined is used.

Inspection of the previous examples shows that it is possible to write the coordinate transform Eq. 2.43 as

$$M_{QF} = \begin{pmatrix} \cos\left(h\sqrt{n}s\right) & \frac{1}{h\sqrt{n}}\sin\left(h\sqrt{n}s\right) \\ -h\sqrt{n}\sin\left(h\sqrt{n}s\right) & \cos\left(h\sqrt{n}s\right) \end{pmatrix}. \tag{2.44}$$

If we had the situation of a defocusing quadrupole we would have $1 - n \to -n$ so that the solutions could be written

$$M_{QD} = \begin{pmatrix} \cosh\left(h\sqrt{n}s\right) & \frac{1}{h\sqrt{n}}\sinh\left(h\sqrt{n}s\right) \\ h\sqrt{n}\sinh\left(h\sqrt{n}s\right) & \cosh\left(h\sqrt{n}s\right) \end{pmatrix}. \tag{2.45}$$

The aforementioned drift can be written as

$$M_D = \begin{pmatrix} 1 & L \\ 0 & 1 \end{pmatrix}. \tag{2.46}$$

There are several resource available which give a detailed accounting of the transfer matrices for different beam line elements, even up to higher orders [29, 27]. We note here that $h\sqrt{n} \equiv k_\beta = \sqrt{B'/(RB_0)}$, which we will see later is the betatron wavenumber.

To handle a series of beam line elements it suffices to apply the appropriate transfer matrices in the appropriate order. For example, if a particle with initial conditions (x_0, x'_0) were to traverse and drift of length L_1 followed by a focusing quad and another drift of length L_2, its position at the end (x_f, x'_f) would be described by

$$\begin{pmatrix} x_f \\ x'_f \end{pmatrix} = M_D M_{QD} M_D \begin{pmatrix} x_0 \\ x'_0 \end{pmatrix} = \begin{pmatrix} 1 & L_2 \\ 0 & 1 \end{pmatrix} \begin{pmatrix} 1 & 0 \\ \frac{1}{f} & 1 \end{pmatrix} \begin{pmatrix} 1 & L_1 \\ 0 & 1 \end{pmatrix} \begin{pmatrix} x_0 \\ x'_0 \end{pmatrix}. \qquad (2.47)$$

In this case we have used the thin quadrupole approximation and f is the focal length of the quadrupole.

This method of analyzing beam transport can be expanded to include all possible relations between initial states and final states. Specifically this means that we can model to first order any accelerating system using

$$\begin{pmatrix} x_f \\ x'_f \\ y_f \\ y'_f \\ z_f \\ \delta_f \end{pmatrix} = \begin{pmatrix} R_{11} & R_{12} & R_{13} & R_{14} & R_{15} & R_{16} \\ R_{21} & R_{22} & R_{23} & R_{24} & R_{25} & R_{26} \\ R_{31} & R_{32} & R_{33} & R_{34} & R_{35} & R_{36} \\ R_{41} & R_{42} & R_{43} & R_{44} & R_{45} & R_{46} \\ R_{51} & R_{52} & R_{53} & R_{54} & R_{55} & R_{56} \\ R_{61} & R_{62} & R_{63} & R_{64} & R_{65} & R_{66} \end{pmatrix} \begin{pmatrix} x_i \\ x'_i \\ y_i \\ y'_i \\ z_i \\ \delta_i \end{pmatrix}. \qquad (2.48)$$

The elements of this matrix can be derived in the same fashion as those above, it is simply a matter of keeping track of more elements or examining the physics of how the momentum deviation δ may affect the position of a particle in the $\hat{x}$ direction. As we shall see in the experimental analysis section this matrix is often block diagonal and comprised exactly of the elements derived earlier.

While it is possible to take into account higher order effects in such a formalism, the utility of such a system in relation to the experiments presented in this work is marginal so a derivation will be left to the references [32].

2.7 Particle Collections and Beam Moments

We now investigate how this formalism applies to collections of particles. We define a collection of particles by a distribution function $f(\vec{x}, \vec{v})$, where $\vec{x}$ and $\vec{v}$ represent 6D coordinates in phase space. As is traditional for these types of analyses the distribution functions are considered separable in all 6 coordinates, that is $f(\vec{x}, \vec{v}) = f(x)f(y)f(z)f(v_x)f(v_y)f(v_z),$. Each distribution function is normalized to unity so that the integral over all space is itself unity,

$$\int_{-\infty}^{\infty} \mathrm{d}^3\vec{x}\, \mathrm{d}^3\vec{v}\, f(\vec{x}, \vec{v}) = 1. \tag{2.49}$$

This means that in order to scale the function to the charge we are interested in we need only multiply by qN_e. It is of course possible to have correlated beams (and thus correlated distribution functions) but absent *a priori* reasons to assume such correlations a thermalized beam which is uncorrelated in the coordinates is usually assumed.

To characterize these collections of particles, or beams, moments of the distribution function are taken [33]. Of primary importance are the first and second moment which give the offset of the beam and the r.m.s. size of the beam. The moments of a distribution function can be found using

$$<x^n> = \int \mathrm{d}x\, x^n f(x). \tag{2.50}$$

We are interested in the evolution of the beam over the course of a section of the accelerator. To obtain a measure of the beam parameters as a function of position along the accelerator and using the matrix formalism previously defined we make use of orbit function techniques. If we know, or can estimate, the beam distribution prior to some section of our accelerator as a Gaussian the initial distribution is given by

$$f(x,x') = \frac{1}{\sqrt{2\pi}\sigma_x}\frac{1}{\sqrt{2\pi}\sigma_{x'}}e^{-\frac{x_i^2}{2\sigma_x^2}}e^{-\frac{x_i'^2}{2\sigma_{x'}^2}}. \tag{2.51}$$

We find the first two moments for the coordinates (x_i, x_i') are $< x >=< x' >= 0$ and $< x^2 >= \sigma_x^2$, $< x'^2 >= \sigma_{x'}^2$, as might have been guessed given the form of the distributions.

Using the results from the previous section we can write the integrals which define the calculation of the moments of the final coordinates as,

$$\begin{aligned} <x_f^n> &= \int_{-\infty}^{\infty} \mathrm{d}x_f\, \mathrm{d}x_f'\, x_f^n\, f(x_f, x_f') \\ &= \int_{-\infty}^{\infty} \mathrm{d}x_f\, \mathrm{d}x_f'\, x_f^n\, f(M \cdot \vec{x}_i), \end{aligned} \tag{2.52}$$

where we have represented the linear transform from the initial to the final position using the matrix notation of the previous section, $x_f = M \cdot \vec{x}_i$. If we instead look for the moments of $M \cdot \vec{x}_i$ we find

$$<\vec{x}_f^n> = <(M \cdot \vec{x}_i)^n> = \int_{\infty}^{\infty} \mathrm{d}x_i\, \mathrm{d}x_i'\, (M \cdot \vec{x}_i)^n\, f(x_i, x_i'), \tag{2.53}$$

which may have been deduced from the previous relation if we note that since det(M)=1 the Jacobian of the coordinate transform from $\mathrm{d}x_i\mathrm{d}x_i'$ to $\mathrm{d}x_f\mathrm{d}x_f'$ is unity.

If we assume the beam is well aligned to the accelerating system, and thus $< x >= 0$, then we are most interested in the evolution of the second moments along the accelerator,

$$
\begin{aligned}
\sigma_f^2 &= \int_{\infty}^{\infty} \mathrm{d}x_i \, \mathrm{d}x_i' \, (M \cdot \vec{x}_i)^2 \, f(x_i, x_i') = \int_{\infty}^{\infty} \mathrm{d}x_i \, \mathrm{d}x_i' \, (M \cdot \vec{x}_i)^2 \, f(x_i, x_i') \\
&= \int_{\infty}^{\infty} \mathrm{d}x_i \, \mathrm{d}x_i' \, (M \cdot \vec{x}_i) \cdot (M \cdot \vec{x}_i)^T \, f(x_i, x_i') \\
&= M \cdot \left(\int_{\infty}^{\infty} \mathrm{d}x_i \, \mathrm{d}x_i' \begin{pmatrix} x_i x_i & x_i x_i' \\ x_i x_i' & x_i' x_i' \end{pmatrix} f(x_i, x_i') \right) \cdot M^T \\
&= M \cdot \sigma_i^2 \cdot M^T.
\end{aligned}
\tag{2.54}
$$

In the last equation σ_i^2 is the matrix of initial second order moments of the beam. It is possible to define a beam ellipse by noting that

$$
x^T \cdot \sigma^2 \cdot x = \sigma_{x'}^2 x^2 - 2\sigma_{xx'}^2 x x' + \sigma_x^2 x'^2 = 1, \tag{2.55}
$$

is an equation for an ellipse. The area of this ellipse is $\pi \det(\sigma^2)$.

The propagation of the beam moments can be recast into an oft used notation credited to Courant-Snyder [34, 35] by setting $\sigma = \epsilon T$, where ϵ is a constant and T is defined as

$$
T \equiv \begin{pmatrix} \beta & -\alpha \\ -\alpha & \gamma \end{pmatrix}. \tag{2.56}
$$

β, α and γ are the so-called Twiss Parameters for which it can be shown that

$$
\gamma(s) x^2 + 2\alpha(s) x x' + \beta(s) x'^2 = \epsilon, \tag{2.57}
$$

which is an equation for an ellipse in phase space. Given the relation between the Twiss parameters and the beam second moment matrix, the Twiss parameters are seen to evolve along the accelerator as $T_f = M \cdot T_i \cdot M^T$. The constant quantity ϵ is a measure of the phase space area of the beam, $A_{p.s.} = \pi\epsilon$ and is called the beam "emittance".

Given the nature of the above distribution functions as infinite it is not practical in an experimental setting to keep track of all particles. As such, when measuring beam parameters *in situ* it is necessary to define a region of interest. Typically this involves constraining the parameters to be measured (e.g. β and α) by requiring the measured ellipses contain 90% of the beam charge. This means that while Liouville's theorem states that phase space area is conserved the practical area of the beam is an ellipse which contains 90% of the charge. Thus the practical area does grow when the elements in the transport are non-linear. This growth is due to the fact that the phase space captured by the ellipse contains gaps. Were we able to distinguish between the populated portions of space and the vacant portions we would see that the phase space area is conserved. A set of examples of phase spaces are plotted in Figure 2.4

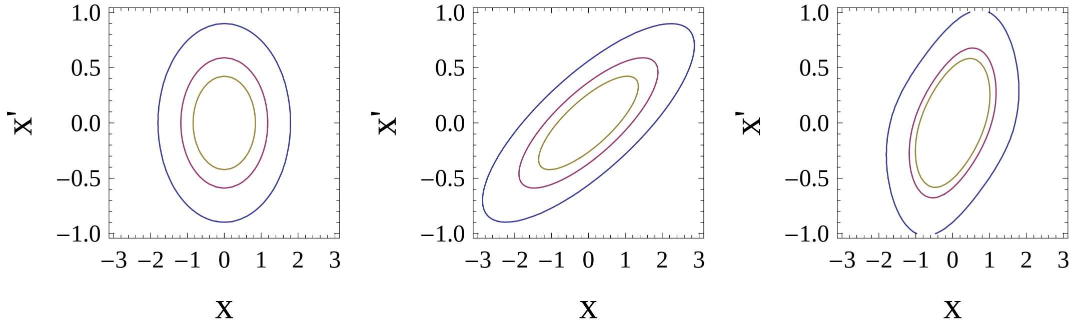

Figure 2.4: A set of examples showing (x,x') phase spaces. a) An example of a gaussian beam with $\frac{\sigma_x}{\sigma_{x'}} = 2$. b) The same distribution as a) but after a drift of 2.5m. c) The same initial phase space as a) but after an rf cavity designed to kick the beam based on transverse position, $f(x') = e^{-\frac{1}{2\sigma_{x'}}(x'-0.3\sin x)}$.

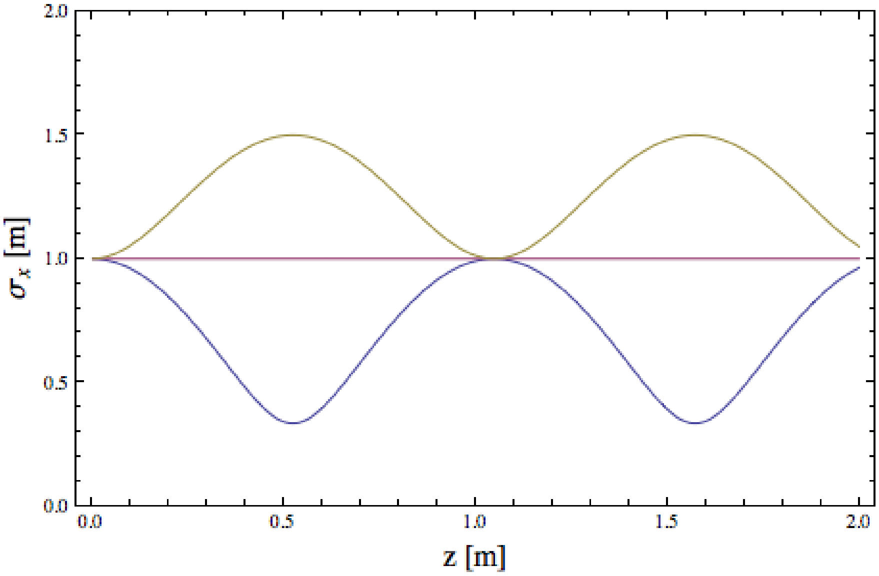

Figure 2.5: The change of σ_x as a function of position z. For this example a uniform focusing channel has been assumed with wavenumber k. The blue curve represents the case in which $k > \epsilon$, the red case is the matched case, where $\sigma_x^2 = \frac{\epsilon}{k}$ and the yellow case is where $k < \epsilon$.

2.7.1 Evolution of the Distribution

We looks now for a way to describe the evolution of the beam size σ_x in the presence of of forces. To begin we look at the change of the σ_x with z,

$$\begin{aligned} \frac{\mathrm{d}\sigma_x}{\mathrm{d}z} &= \frac{1}{2\sigma_x}\frac{\mathrm{d}\langle x^2\rangle}{\mathrm{d}z} = \frac{\sigma_{xx'}}{\sigma_x}, \\ \frac{\mathrm{d}^2\sigma_x}{\mathrm{d}^2z} &= -\frac{\sigma_{xx'}^2}{\sigma_x^3} + \frac{\sigma_{x'}^2}{\sigma_x} - k^2(z)\sigma_x, \end{aligned} \tag{2.58}$$

where we have used $x'' = k^2(z)x$. As noted in the previous section the determinant of the matrix of beam moments is a constant value, we now write it explicitly as

$$\det\begin{vmatrix} \sigma_x^2 & \sigma_{xx'} \\ \sigma_{xx'} & \sigma_{x'}^2 \end{vmatrix} = \sigma_x^2\sigma_{x'}^2 - \sigma_{xx'}^2 = \epsilon^2. \tag{2.59}$$

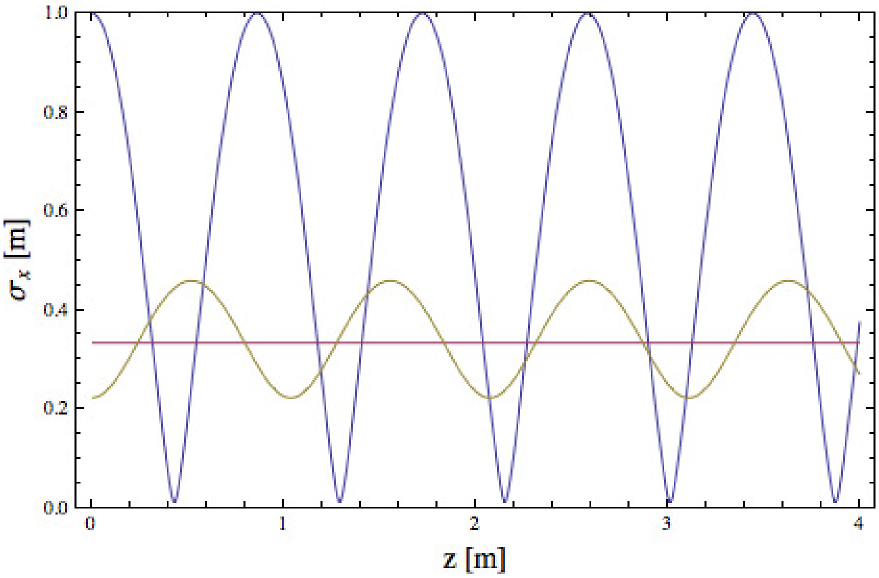

Figure 2.6: This plot uses the same values as those used in Figure 2.5. The blue curve represents the case in which $k > \epsilon$, the red case is the matched case, where $\beta_x = \frac{1}{k}$ and the yellow case is where $k < \epsilon$.

This relation allows us to rewrite the previous relation as

$$\sigma_x'' + k^2(z)\sigma_x = \frac{\epsilon^2}{\sigma_x^3}. \tag{2.60}$$

Examples of numerical solutions to this equation are shown in Figure 2.5. We see that careful selection of beam parameters when in a focusing field with associated wavenumber k creates a situation in which the beam size does not oscillate. This branding of the evolution of the beam size while accurate and useful can be a bit cumbersome to use in practice.

A more straightforward excise in determining the changes of beam size in a given accelerator lattice is the use of the matrix formalism previously developed, namely Equation 2.54. As an example we look at the case of a beam in a drift of length z, i.e. where k(z)=0. The change in beam size looks like

$$\sigma_f = \begin{pmatrix} \sigma_x^2 + z\sigma_{xx'} + z(z\sigma_{x'}^2 + \sigma_{xx'}) & z\sigma_{x'}^2 + \sigma_{xx'} \\ z\sigma_{x'}^2 + \sigma_{xx'} & \sigma_{x'}^2 \end{pmatrix}. \tag{2.61}$$

If we assume that the beam is not correlated in x-x' so that $\sigma_{xx'} = 0$ we find that

$$\sigma_x(z) = \sqrt{\sigma_x(0)^2 + z^2\sigma_{x'}^2} = \sigma_x(0)\sqrt{1 + z^2\frac{\epsilon^2}{\sigma_x(0)^4}} \tag{2.62}$$

where in the final expression we have used the emittance to relate beam spread $\sigma_{x'}$ to beam size σ_x. The similarity between the last expression and the evolution of the beam size of a light beam [36] allows us to write the equivalent beam based Rayleigh length as

$$z_{R,beam} = \frac{\sigma_x^2}{\epsilon}. \tag{2.63}$$

Examination of Equation 2.56 shows that this Rayleigh range has already been defined as β_x. We chose to denote β with a subscript here to avoid confusion with the normalized beam velocity. Equation 2.62 can then be transformed to be written as an expression defining the evolution the so-called beta function,

$$\beta_x'' + 2k(z)^2\beta_x - \frac{2}{\beta_x} = 0. \tag{2.64}$$

An example of the evolution of the beta function as a function of z in a uniform constant focusing channel is shown in Figure 2.6.

Understanding these types of oscillations in beam size will prove to be immensely useful in later sections when we discuss the effects of dipole forces and attempts to contain them using focusing systems.

CHAPTER 3

Beam Based Radiation

Radiation generated by charged particle beams is the subject of many theses; be it undulator, transition or bending. As such, a complete survey of all sources and their use is well beyond the scope of this thesis. However, there are sources of beam based radiation used in the course of the experiments presented in this work which necessitate covering their generation and application. We start with a survey of the salient details of Transition Radiation [37, 38], including Coherent Transition Radiation (CTR). The latter serves as a means of describing what it means for a radiation source to be coherent. We then move on to Coherent Diffraction Radiation (CDR) and Coherent Cherenkov Radiation (CCR) and their relation to these experiments. Finally we discuss the Kramers-Kronig relations [39, 40] and their application as a method for deriving the shape of beams from the spectral content of the radiation generated by beam-structure interactions.

3.1 Transition Radiation

Simply put, transition radiation is the radiation emitted by a charged particle as it transitions from one material to another. In the case of beam diagnostics, optical transition radiation is used to measure transverse beam size and position by impinging the beam on a metal foil [41, 42]. For the purposes of this thesis

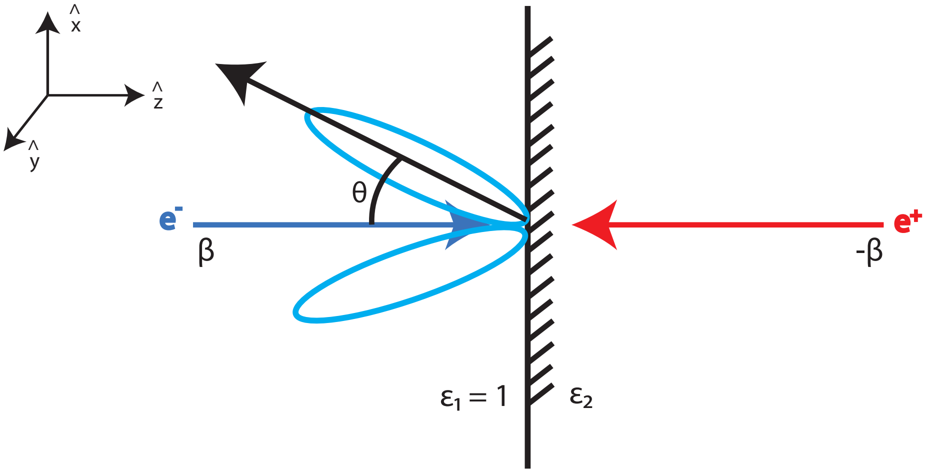

Figure 3.1: A stylistic representation of the generation of transition radiation. A free electron (blue) is incident, from the left, on a metal surface ($\epsilon_2 \to \infty$), from vacuum ($\epsilon_1 = 1$). The free particle's image charge is shown in red.

and the analysis to follow we present a succinct, if less than rigorous, derivation of transition radiation. The interested reader may find a rigorous derivation in Ref. [14, 37, 43].

We begin with a physical description of the problem at hand. As shown in Fig. 3.1 a free particle traveling along the $\hat{z}$-axis is incident (from the left) on a metal surface. Included in the diagram is the free particle's image charge, shown in red. When the particle enters the metal it is effectively shielded by the mobile charges in the conductor thus vanishing from the problem. In essence, the free charge and image charge collide at the vacuum-metal boundary and annihilate. This behavior can be modeled by an abrupt change of the velocity of the particle to zero. Abrupt in this case means any change in velocity that occurs over a period of time shorter than the formation length of the radiation [44]. With this in mind, we make the assumption that the stopping time is infinitely short and that the particle's velocity is constant for the purposes of analysis.

To quantify the above description of the source of Transition Radiation, we write an equation for the energy radiated per unit solid angle per unit frequency of a charge in motion [14]:

$$\frac{d^2I}{d\omega d\Omega} = \frac{\omega^2}{4\pi^2 c}\Big| \int_{-\infty}^{\infty} q\hat{n} \times (\hat{n} \times \boldsymbol{\beta}) e^{i\omega(t-\hat{n}\cdot\vec{r}(t)/c)} dt \Big|^2. \tag{3.1}$$

Following the discussion above and using the diagram in Fig. 3.1, we can write the velocity of the free particle as $\boldsymbol{\beta} = -\beta\hat{z}\Theta(-t)$ and the image particle as $\boldsymbol{\beta}_i = \beta\hat{z}\Theta(-t)$, where $\Theta(t)$ represents the Heaviside step function. The velocities are written such that the particles annihilate at t=0. As rectilinear motion is assumed the corresponding particle positions may be written as $\vec{r}(t) = \beta c t\Theta(-t)\hat{z}$, with a similar expression for the image charge. Substituting these equations into Eq. 3.1 yields,

$$\frac{d^2I}{d\omega d\Omega} = \frac{e^2\omega^2}{4\pi^2 c}\Big| \int_{-\infty}^{0} \hat{n}\times(\hat{n}\times\boldsymbol{\beta}) e^{i\omega t(1-\beta\cos\theta)} e^{-\eta|t|} - \hat{n}\times(\hat{n}\times\boldsymbol{\beta}_i) e^{i\omega t(1+\beta\cos\theta)} e^{-\eta|t|} dt \Big|^2. \tag{3.2}$$

Where the exponential involving η has been added to ensure proper behavior of the function at $\pm\infty$. To be more specific, η should be chosen such that the variation of $e^{-\eta|t|}$ with time is much longer than a formation length so it does not contribute to the integral. Noting that angular terms $\hat{n} \times \hat{n} \times \boldsymbol{\beta}$ differ only by a minus sign and are no longer time dependent, they can be pulled out of the square as $\beta^2 \sin^2\theta$. With this in mind we can integrate the above expression and write:

$$\frac{d^2I}{d\omega d\Omega} = \frac{e^2\beta^2\sin^2\theta}{4\pi^2 c}\left| \left(\frac{e^{i\omega t(1-\beta\cos\theta)} e^{-\eta|t|}}{1-\beta\cos\theta - \eta|t|} + \frac{e^{i\omega t(1+\beta\cos\theta)} e^{-\eta|t|}}{1+\beta\cos\theta - \eta|t|} \right)_{-\infty}^{0} \right|^2. \tag{3.3}$$

Explicitly evaluating the function at the limits of integration, and then taking $\eta \to 0$, gives:

$$\frac{d^2I}{d\omega d\Omega} = \frac{e^2\beta^2\sin^2\theta}{4\pi^2 c}\left| \frac{1}{1-\beta\cos\theta} + \frac{1}{1+\beta\cos\theta} \right|^2, \tag{3.4}$$

which after a bit of algebra results in the standard expression for single particle transition radiation,

$$\frac{d^2I}{d\omega d\Omega} = \frac{e^2}{\pi^2 c}\frac{\beta^2 \sin^2\theta}{(1-\beta^2\cos^2\theta)^2}. \tag{3.5}$$

3.2 Diffraction Radiation

We now present a derivation of the radiation generated as a beam passes through a hole of radius a in an infinite metal sheet. As we will eventually be interested in the energy radiated per unit frequency we are interested in the fields of the particle as a function of space and frequency ω, $\vec{E}(\vec{x},\omega)$. Once we have those fields we apply Kirchhoff's diffraction equation to derive the fields at some distance L from the hole, due to the beam in the hole. As this derivation contains a lot of useful expression often used in the field of accelerator physics it will be especially detailed.

3.2.1 Fields of a Moving Charge

We start with Maxwell's equations defining the potentials in a vacuum due to a moving charge as,

$$\begin{aligned}
\vec{\nabla}^2\phi - \frac{1}{c^2}\frac{\partial^2\phi}{\partial t^2} &= -\frac{\rho}{\epsilon_0} \\
\vec{\nabla}^2\vec{A} - \frac{1}{c^2}\frac{\partial^2\vec{A}}{\partial t^2} &= -\mu_0\vec{J} \\
\vec{E} &= -\vec{\nabla}\phi - \frac{\partial\vec{A}}{\partial t} \\
\rho(\vec{x},t) &= q\delta(x-x_0)\delta(y-y_0)\delta(z-vt) \\
\vec{J}(\vec{x},t) &= qv\hat{z}\delta(x-x_0)\delta(y-y_0)\delta(z-vt),
\end{aligned} \tag{3.6}$$

where q is the charge of the particle and the velocity is in the $\hat{z}$ direction. We further define the 4D Fourier transform as,

$$\tilde{f}(\vec{k},\omega) = \int f(\vec{x},t)e^{-i\vec{k}\cdot\vec{x}+i\omega t}\mathrm{d}^3\vec{x}\mathrm{d}t. \tag{3.7}$$

The system of Equations 3.6 can then be Fourier transformed into a system of algebraic equations for which the electric field can be written as,

$$\tilde{\vec{E}}(\vec{k},\omega) = \frac{iq}{2\pi\epsilon_0}\frac{\delta(\omega - k_z v)}{\frac{\omega^2}{c^2} - k^2}e^{-i\vec{k}_\perp\cdot\vec{x}_{\perp 0}}(\vec{k} - \frac{\omega}{c^2}v\hat{z}), \tag{3.8}$$

where $k^2 = k_x^2 + k_y^2 + k_z^2$ and $\vec{k}_\perp \cdot \vec{x}_{\perp 0} = k_x x_0 + k_y y_0$. We can then write the electric field in real space as,

$$\vec{E}(\vec{x},\omega) = \frac{1}{(2\pi)^{3/2}}\frac{iq}{2\pi\epsilon_0}\int_{-\infty}^{\infty}\frac{\delta(\omega - k_z v)}{\frac{\omega^2}{c^2} - k^2}e^{-i\vec{k}_\perp\cdot\vec{x}_{\perp 0}}(\vec{k} - \frac{\omega}{c^2}v\hat{z})e^{i\vec{k}\cdot\vec{x}}\mathrm{d}^3\vec{k} \tag{3.9}$$

$$\vec{E}(\vec{x},\omega) = \frac{-iq}{v(2\pi)^{5/2}\epsilon_0}e^{i\frac{\omega}{v}z}\int_{-\infty}^{\infty}\frac{k_x\hat{x} + k_y\hat{y} + \frac{\omega}{\gamma^2 v}\hat{z}}{k_x^2 + k_x^2 + \frac{\omega^2}{\gamma^2 v^2}}e^{-i\vec{k}_\perp\cdot\vec{x}_{\perp 0}}e^{i\vec{k}_\perp\cdot\vec{x}_\perp}\mathrm{d}^2\vec{k}_\perp, \tag{3.10}$$

in the latter equation we have performed the integration over k_z using the delta function. Given the nature of the problem, as stated above, we are looking for $E_\rho(\vec{x},\omega)$. As such we write

$$E_\rho(\vec{x},\omega) = \frac{-iq}{v(2\pi)^{5/2}\epsilon_0}e^{i\frac{\omega}{v}z}\int_{-\infty}^{\infty}\frac{k_x cos(\theta) + k_y sin(\theta)}{k_x^2 + k_x^2 + \frac{\omega^2}{\gamma^2 v^2}}e^{ik_\perp\cdot(\vec{x}_\perp - \vec{x}_{\perp 0})}\mathrm{d}^2\vec{k}_\perp \tag{3.11}$$

$$k_\perp \cdot (\vec{x}_\perp - \vec{x}_{\perp 0}) = k_\perp \cdot \left[(\rho cos(\theta) - \rho_0 cos(\theta_0))\hat{x} + (\rho sin(\theta) - \rho_0 sin(\theta_0))\hat{y}\right]. \tag{3.12}$$

If we further perform the $\mathrm{d}^2\vec{k}_\perp$ integral in polar coordinates using $k_x = k_\perp cos(\theta_k)$ and $k_y = k_\perp sin(\theta_k)$ we are left with,

$$E_\rho(\vec{x},\omega) = \frac{-iq}{v(2\pi)^{5/2}\epsilon_0}e^{i\frac{\omega}{v}z}\int\frac{k_\perp cos(\theta_k - \theta)}{k_\perp^2 + \frac{\omega^2}{\gamma^2 v^2}}e^{ik_\perp\rho cos(\theta_k - \theta)}e^{-ik_\perp\rho_0 cos(\theta_k - \theta_0)}k_\perp\mathrm{d}k_\perp\mathrm{d}\theta_k \tag{3.13}$$

$$E_\rho(\vec{x},\omega) = \frac{-iq}{v(2\pi)^{5/2}\epsilon_0} e^{i\frac{\omega}{v}z} \int_0^\infty \mathrm{d}k_\perp \frac{k_\perp^2}{k_\perp^2 + \frac{\omega^2}{\gamma^2 v^2}} * \\ \int_0^{2\pi} \mathrm{d}\theta_k cos(\theta_k - \theta) e^{ik_\perp \rho cos(\theta_k - \theta)} e^{-ik_\perp \rho_0 cos(\theta_k - \theta_0)}. \tag{3.14}$$

Performing the θ_k integral yields,

$$E_\rho(\vec{x},\omega) = \frac{q}{v(2\pi)^{3/2}\epsilon_0} e^{i\frac{\omega}{v}z} \int_0^\infty \mathrm{d}k_\perp \frac{k_\perp^2}{k_\perp^2 + \frac{\omega^2}{\gamma^2 v^2}} J_1\big(k_\perp(\rho - \rho_0)\big), \tag{3.15}$$

and finally the $k_\perp$ integral is performed using [45],

$$\int_0^\infty \frac{xJ_0(ax)}{x^2 + p^2} \mathrm{d}x = K_0(ap), \tag{3.16}$$

to give

$$E_\rho(\vec{x},\omega) = \frac{q}{v(2\pi)^{3/2}\epsilon_0} e^{i\frac{\omega}{v}z} \frac{\omega}{\gamma v} K_1\big(\frac{\omega}{\gamma v}(\rho - \rho_0)\big). \tag{3.17}$$

If one repeats the same procedure to attempt to calculate $E_\theta(\vec{x},\omega)$ the obliquity factor $cos(\theta_k - \theta) \rightarrow sin(\theta_k - \theta)$ in Equation 3.14 so that the integral over θ_k vanishes. For $E_z(\vec{x},\omega)$, $k_\perp cos(\theta_k - \theta) \rightarrow \frac{\omega}{\gamma^2 v}$ and one finds,

$$E_\theta(\vec{x},\omega) = 0, \tag{3.18}$$

$$E_z(\vec{x},\omega) = \frac{iq\omega}{(2\pi)^{3/2}\gamma^2 v^2 \epsilon_0} e^{i\frac{\omega}{v}z} \left[\frac{1}{\rho - \rho_0} - \frac{\pi\omega}{2\gamma v} I_0\big(\frac{\omega}{\gamma v}(\rho - \rho_0)\big) + L_0\big(\frac{\omega}{\gamma v}(\rho - \rho_0)\big)\right], \tag{3.19}$$

where I_0 is the modified Bessel function of the first kind and L_0 is the Struve function [45]. Of note is the extra factor of γ in the denominator of E_z which is consistent with the scaling of the fields derived through other methods. This is the so-called "pancaking" of the fields of a relativistic charge [14]. For the experiments conducted in this work $\gamma \sim 40000$ so E_z can be ignored.

3.2.2 Kirchhoff and Diffraction

We continue now with the generalized Kirchhoff integral for a source on a surface S_1,

$$\Psi(\vec{x}) = -\frac{ik}{2\pi}\int_{S_1}\frac{e^{ikR_{pq}}}{R_{pq}}(1+\frac{i}{kR_{pq}})\Psi(\vec{x'})\mathrm{d}a', \tag{3.20}$$

where $\Psi(\vec{x})$ is any given field component (i.e. E_x), S_1 is defined using Dirichlet boundary conditions as the surface on which the initial field $\Psi(\vec{x'})$ is non-zero and R_{pq} is the distance between the source and the point of interest. If R_{pq} is written as,

$$\vec{R}_{pq} = \vec{R} - \vec{r'}, \tag{3.21}$$

then

$$|R_{pq}|^2 = (\vec{R}-\vec{r'})\cdot(\vec{R}-\vec{r'}) = R^2 + r'^2 s - 2\vec{R}\cdot\vec{r'} \tag{3.22}$$

$$R_{pq} = R\sqrt{1+\frac{r'^2}{R^2}-\frac{2\vec{R}\cdot\vec{r'}}{R^2}}. \tag{3.23}$$

A graphical representation is shown in Figure 3.2. The last equation can be expanded for $r' \ll R$ as,

$$R_{pq} \sim R - \vec{r'}\cdot\hat{n} + \frac{r'^2}{2R} - \frac{1}{2}\frac{(\vec{r'}\cdot\hat{n})^2}{R} \tag{3.24}$$

for $\hat{n} = \vec{R}/R$. When used to replace R_{pq} in the exponential in Equation 3.20 the first two terms on the right hand side of equation 3.24 represent the Fraunhofer, or far-field, approximation and all four terms the Fresnel, or near-field, approximation. Applying the Fraunhofer approximation for the exponential and setting all other R_{pq} to R yields

$$\Psi(\vec{x}) = -\frac{ik}{2\pi}\frac{e^{ikR}}{R}(1+\frac{i}{kR})\int_{S_1}e^{-ik\hat{n}\cdot\vec{r'}}\Psi(\vec{x'})\mathrm{d}a'. \tag{3.25}$$

Some literature uses only the first three terms as the Fresnel approximation. Since it is an approximation, it is usually user's choice. The standard procedure

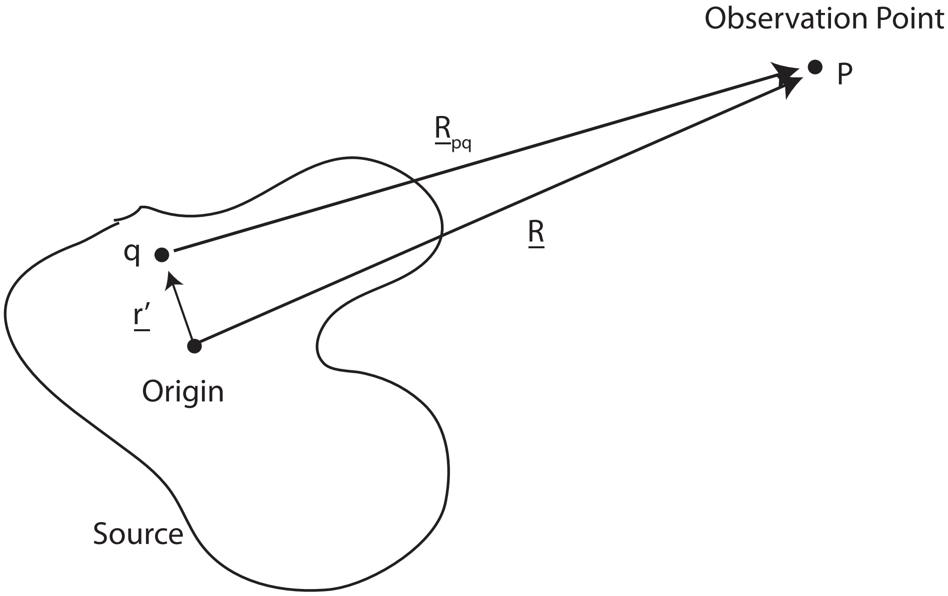

Figure 3.2: A representation of the handling of $\vec{R}_{pq}$, the distance between a point in the source, q, and the observation point P.

is to pick an approximation which is actually integrable using Kirchhoff's integral relation (Equation 3.20) and then to numerically integrate said integral with the full $\vec{R}$ and check the range of applicability.

As an example, coherent transition radiation collected at FACET is done so at a distance of 1 m from the source with an aperture of 3.8 cm. The Fresnel number $N_f = \frac{a^2}{\lambda L}$ is ∼3 so the Fresnel approximation applies. However, the angle is $\theta \sim 0.038$ so that the $\vec{r'} \cdot \hat{n}$ terms are effectively zero and one would be fine using the first and third terms only [46].

3.2.3 Diffraction Radiation from a Hole

Using the previous relation and the equation describing the radial fields of an electron, Eq. 3.51, we can now state the fields "stripped" from a particle as it passes through a hole of radius a in an otherwise infinite sheet of metal at $z = 0$

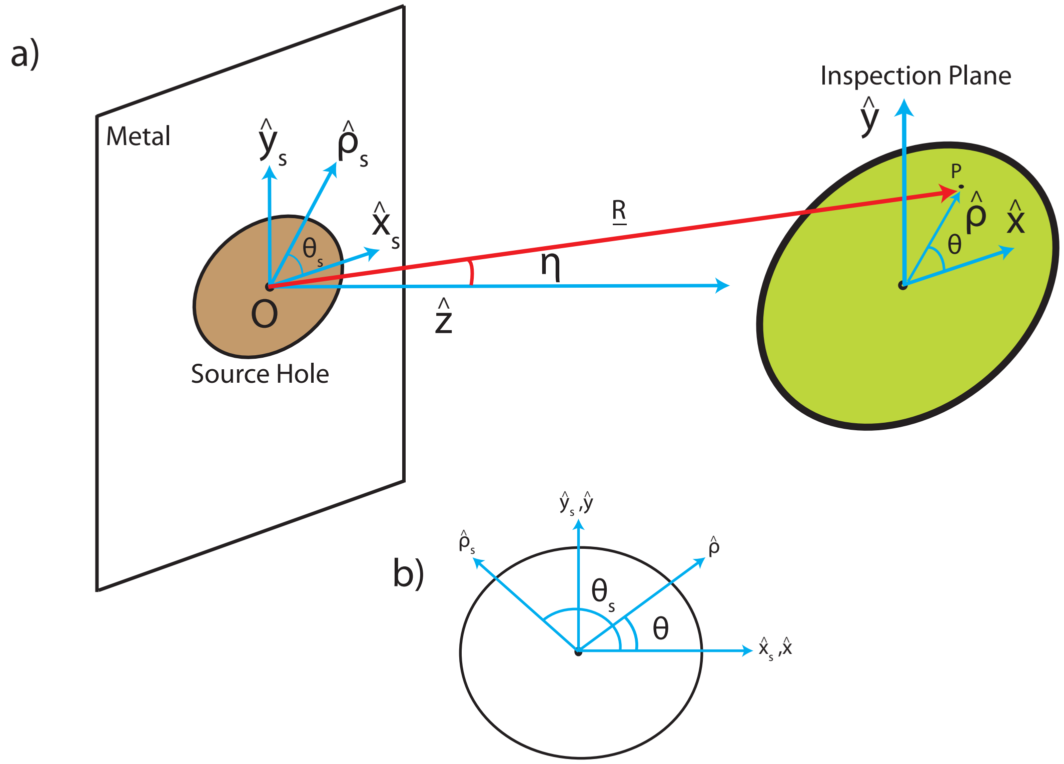

Figure 3.3: a) A diagram of the problem described in Section 3.2.3. b) The source and inspection planes as looking down the $\hat{z}$ axis.

as,

$$E_\rho(\vec{x},\omega) = -\frac{ik}{(2\pi)^{5/2}}\frac{q\omega}{\gamma v^2\epsilon_0}\frac{e^{ikR}}{R}(1+\frac{i}{kR})\int_{S_1} e^{-ik\hat{n}\cdot\vec{r'}}K_1(\frac{\omega\rho'}{\gamma v})(\hat{\rho}\cdot\hat{\rho}_s)\mathrm{d}a'. \quad (3.26)$$

In the above relation we have assumed a particle on axis, $\rho_0 = 0$, and $\hat{\rho}\cdot\hat{\rho}_s$ is defined as the obliquity factor between the field direction at the source, $\hat{\rho}_s$, and the field direction elsewhere, $\hat{\rho}$. Figure 3.3 helps elucidate the description. For this problem we explicitly define the various vectors as,

$$\hat{\rho}\cdot\hat{\rho}_s = cos(\theta_s-\theta) \tag{3.27}$$

$$\hat{n} = cos(\eta)\hat{z} + sin(\eta)\big(cos(\theta)\hat{x} + sin(\theta)\hat{y}\big) \tag{3.28}$$

$$\vec{r'} = \rho'\big(cos(\theta_s)\hat{x} + sin(\theta_s)\hat{y}\big) \tag{3.29}$$

$$\hat{n}\cdot\vec{r'} = \rho' sin(\eta) cos(\theta_s-\theta), \tag{3.30}$$

so that we can write the Kirchhoff integral as,

$$\begin{aligned} E_\rho(\vec{x},\omega) = -\frac{ik}{(2\pi)^{5/2}}\frac{q\omega}{\gamma v^2\epsilon_0}\frac{e^{ikR}}{R}(1+\frac{i}{kR})\int_{\rho_1}^{\rho_2}\rho'\mathrm{d}\rho' K_1(\frac{\omega\rho'}{\gamma v})*\\ \int_0^{2\pi}\mathrm{d}\theta_s\, cos(\theta_s-\theta)e^{-ik\rho' sin(\eta)cos(\theta_s-\theta)}. \end{aligned} \tag{3.31}$$

In the above expression we have purposefully left the limits of the ρ' integral ambiguous and will select the limits when discussing the relation between diffraction radiation and transition radiation. Continuing with the θ_s integral gives,

$$E_\rho(\vec{x},\omega) = -\frac{k\omega}{\gamma v^2}\frac{q}{(2\pi)^{3/2}\epsilon_0}\frac{e^{ikR}}{R}(1+\frac{i}{kR})\int_{\rho_1}^{\rho_2}\rho'\mathrm{d}\rho' K_1(\frac{\omega\rho'}{\gamma v})J_1\big(k\rho' sin(\eta)\big). \tag{3.32}$$

The final integral can be written as,

$$\begin{aligned} &\int_{\rho_1}^{\rho_2}\rho'\mathrm{d}\rho' K_1(\alpha\rho')J_1(\delta\rho') = \\ &\frac{\delta}{\alpha^2+\delta^2}\Big\{-\rho_1 J_2(\delta\rho_1)K_1(\alpha\rho_1) + \rho_2 J_2(\delta\rho_2)K_1(\alpha\rho_2) + \\ &\rho_1\frac{\alpha}{\delta}J_1(\delta\rho_1)K_2(\alpha\rho_1) - \rho_2\frac{\alpha}{\delta}J_1(\delta\rho_2)K_2(\alpha\rho_2)\Big\}, \end{aligned} \tag{3.33}$$

where $\alpha = \omega/(\gamma v) = k/(\gamma\beta)$ and $\delta = ksin(\eta)$. Rewriting the term outside the curly braces in the above expression gives,

$$\frac{\delta}{\alpha^2+\delta^2} = \frac{\beta}{k}\frac{\beta sin(\eta)}{1-\beta^2 cos^2(\eta)}. \tag{3.34}$$

We can write the final expression as,

$$E_\rho(\vec{x},\omega) = -\frac{k}{\gamma v}\frac{q}{(2\pi)^{3/2}\epsilon_0}\frac{e^{ikR}}{R}(1+\frac{i}{kR})\frac{\beta sin(\eta)}{1-\beta^2 cos^2(\eta)}H(\alpha,\delta,\rho_1,\rho_2), \tag{3.35}$$

where $H(\alpha,\delta,\rho_1,\rho_2)$ represents the function in the curly brackets in Eq. 3.33.

3.2.4 Energy Radiated in the Far Field

With an expression for the fields radiated by a particle passing through a hole in a metal sheet in hand we now wish to derive an expression for the energy radiated per unit solid angle. This will tell us what the distribution will look like on our detector.

We begin by noting that the total energy radiated per unit solid angle, $dW/d\Omega$, can be defined as,

$$\frac{dW}{d\Omega} = \int_{-\infty}^{\infty} \frac{dP(t)}{d\Omega}\,\mathrm{d}t, \tag{3.36}$$

and the power $P(t)$ as,

$$P(t) = \int \vec{S}(t)\cdot \mathrm{d}\vec{A} = \int R^2(\vec{S}(t)\cdot\hat{n})\mathrm{d}\Omega. \tag{3.37}$$

In the far field limit the radiation manifests as a plane wave so the time-averaged Poynting vector $\vec{S}(t)$ can be written

$$\vec{S}(t) = \frac{1}{\mu_0}\vec{E}\times\vec{B}^* = \frac{1}{2\mu_0 c}\vec{E}\times(\hat{n}\times\vec{E}^*) = \frac{1}{2\mu_0 c}|\vec{E}(t)|^2\hat{n} \tag{3.38}$$

Combining all of the above to arrive at a more useful expression for $dW/d\Omega$ gives,

$$\frac{dW}{d\Omega} = \int_{-\infty}^{\infty}\frac{R^2}{2\mu_0 c}\vec{E}(t)\cdot\vec{E}^*(t)\,\mathrm{d}t. \tag{3.39}$$

To recast the above function of $\vec{E}(\omega)$ the Fourier transform is used,

$$\frac{dW}{d\Omega} = \frac{1}{2\pi}\int_{-\infty}^{\infty}\mathrm{d}t\frac{R^2}{2\mu_0 c}\int_{-\infty}^{\infty}\mathrm{d}\omega\vec{E}(\omega)e^{i\omega t}\cdot\int_{-\infty}^{\infty}\mathrm{d}\omega'\vec{E}^*(\omega)e^{-i\omega' t}, \tag{3.40}$$

and the order of integration is reversed to give,

$$\frac{dW(\omega)}{d\Omega} = \int_{-\infty}^{\infty}\frac{R^2}{2\mu_0 c}|\vec{E}(\omega)|^2\,\mathrm{d}\omega, \tag{3.41}$$

where

$$\frac{\mathrm{d}^2 I}{\mathrm{d}\omega\mathrm{d}\Omega} = \frac{R^2}{2\mu_0 c}|\vec{E}(\omega)|^2 \tag{3.42}$$

is the energy radiated per unit solid angle per unit frequency as in the sections above.

We are now able to write an expression for the energy radiated per unit solid angle per unit frequency for a particle passing through a hole in a metal sheet as

$$\frac{\mathrm{d}^2 I}{\mathrm{d}\omega \mathrm{d}\Omega} = \frac{k^2}{\gamma^2 v^2} \frac{q^2 c}{16\pi^3 \epsilon_0} (1 + \frac{1}{k^2 R^2}) \frac{\beta^2 sin^2(\eta)}{\left(1 - \beta^2 cos^2(\eta)\right)^2} H^2(\alpha, \delta, \rho_1, \rho_2), \tag{3.43}$$

where we note $\frac{k^2}{\gamma^2 v^2} = \frac{\alpha^2}{c^2}$. If the source is then integrated from $\rho_1 = 0$ to $\rho_2 = a$ which is the case in which a particle enters a region through a metal disc of radius a, thus the source of radiation is the disc, gives

$$\lim_{\rho_1 \to 0} \alpha H(\alpha, \delta, \rho_1, a) = 1 + a\alpha J_2(\delta a) K_1(\alpha a) - \frac{a\alpha^2}{\delta} J_1(\delta a) K_2(a\alpha), \tag{3.44}$$

and thus

$$\frac{\mathrm{d}^2 I}{\mathrm{d}\omega \mathrm{d}\Omega} = \frac{q^2}{16\pi^3 c \epsilon_0} (1 + \frac{1}{k^2 R^2}) \frac{\beta^2 sin^2(\eta)}{\left(1 - \beta^2 cos^2(\eta)\right)^2} * \\ \left\{ 1 + a\alpha J_2(\delta a) K_1(\alpha a) - \frac{a\alpha^2}{\delta} J_1(\delta a) K_2(a\alpha) \right\}^2. \tag{3.45}$$

This is seen to be the same as the case for which a particle leaves the region of interest through a metal disc of radius a, which "strips" the fields from the particle as it leaves. In the case that we further allow $\rho_2 \to \infty$ the single particle transition radiation spectrum previously derived is found [47, 48].

If we are instead interested in a particle as it enters or leaves the region of interest through a hole of radius a in an other wise infinite metal sheet, we take $\rho_1 \to a$ and $\rho_2 \to \infty$ and find

$$\lim_{\rho_2 \to \infty} \alpha H(\alpha, \delta, a, \rho_2) = -a\alpha J_2(\delta a) K_1(\alpha a) + \frac{a\alpha^2}{\delta} J_1(\delta a) K_2(a\alpha), \tag{3.46}$$

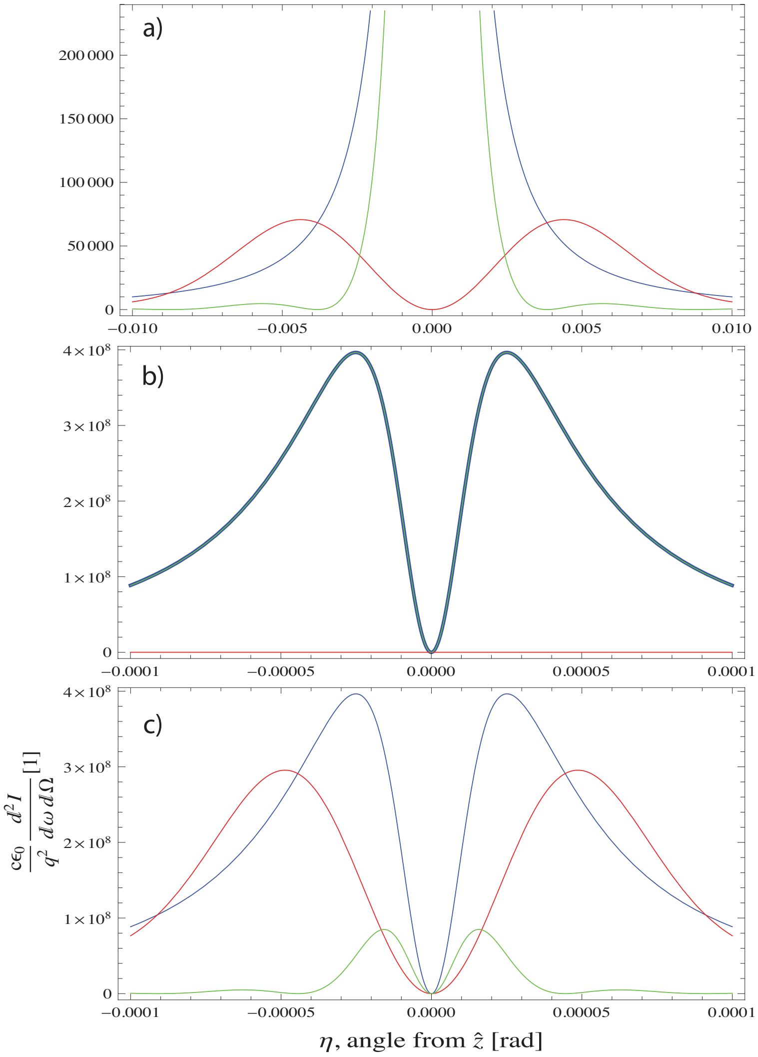

Figure 3.4: A selection of angular profiles of transition radiation from an infinite plane (blue), transition radiation from a finite source (red) and diffraction radiation from a hole (green). The finite source and hole are of the same radius a. a) Uses parameters similar to those of the experiments reported in this work, $\lambda = 30\ \mu m$, $\gamma = 40000$ and a = 3mm. b) is a smaller angular extent of a), to show the on axis null. c) $\lambda = 30\ \mu m$, $\gamma = 40000$ and a = 30cm.

and thus

$$\frac{\mathrm{d}^2 I}{\mathrm{d}\omega \mathrm{d}\Omega} = \frac{q^2}{16\pi^3 c\epsilon_0}(1+\frac{1}{k^2R^2})\frac{\beta^2 sin^2(\eta)}{\left(1-\beta^2 cos^2(\eta)\right)^2} * \\ \left\{ - a\alpha J_2(\delta a)K_1(\alpha a) + \frac{a\alpha^2}{\delta}J_1(\delta a)K_2(a\alpha)\right\}^2 . \tag{3.47}$$

Careful inspection shows that if the sum of the two limits, Equations 3.45 and 3.47, is taken then the factor in the curly brackets falls to unity and the expression for transition radiation from an infinite source is returned.

A comparison of the three sources of radiation is illustrated in Figure 3.4. We plot the angular distribution of energy from transition radiation from an infinite sheet, transition radiation from a disc of radius a and diffraction radiation from a hole of radius a in an infinite metal sheet. We see that as the surface/hole gets larger the transition radiation from a finite sized surface approaches that of an infinite surface and the diffraction radiation energy falls to zero. For this experiment there are a selection of apertures in the $a = 3$ mm to 10 mm range. For the relevant parameters in the experiment performed in this work an energy per unit frequency from 50% to 99% that of transition radiation from an infinite sheet is expected.

If the spectral energy density due to a finite bunch is integrated over all frequencies and all space (see section 3.4) the total CTR energy is expected to be on the order of 10 mJ for this experiment. With a total beam energy loss on the order of 150 mJ, multiple apertures producing 10 mJ of energy loss are a significant source of systematic error that are to be accounted for.

3.3 Čerenkov Radiation

We continue now with a description of Cherenkov Radiation, which is sometimes referred to as Čerenkov or Cherenkov-Vavilov radiation [49, 50, 51]. Generally, Cherenkov radiation is light which is emitted by the excitation of an asymmetric polarization in a medium with an index of refraction greater than one. Asymmetric polarization is brought about when a particle or field capable of imparting a polarization on a given macroscopic media moves faster than the media can respond.

As a first step we present simple conservation of energy and momentum arguments to arrive at the conditions for which Cherenkov radiation is produced. We start with the relativistically correct expression for the energy of a particle, $E^2 = p^2c^2 + (mc^2)^2$. Looking at the expression for small changes in energy and momentum we find that dE $= \frac{c^2\vec{p}}{E} \cdot \mathrm{d}\vec{p} = \vec{v} \cdot \vec{p}$, with $\vec{v}$ as the particle velocity. Taking the change in energy and momentum as $\hbar\omega$ and $n\hbar\omega\hat{n}/c$ respectively, where $\hat{n}$ is the direction of photon emission and n is the index of refraction, the result is

$$\cos\theta_c = \frac{1}{\beta n}. \tag{3.48}$$

This is the standard expression used to find the angle of radiation for light emitted through Cherenkov mechanisms.

In a quantitative treatment we begin as we began the last section, with Equations 3.6 modified to include a homogenous dielectric media described by dielectric constant ϵ_r,

$$\begin{aligned}\vec{\nabla}^2\phi - \frac{\epsilon_r}{c^2}\frac{\partial^2\phi}{\partial t^2} &= -\frac{\rho}{\epsilon_r\epsilon_0}\\ \vec{\nabla}^2\vec{A} - \frac{\epsilon_r}{c^2}\frac{\partial^2\vec{A}}{\partial t^2} &= -\mu_0\vec{J}\\ \vec{E} &= -\vec{\nabla}\phi - \frac{\partial\vec{A}}{\partial t}\\ \rho(\vec{x},t) &= q\delta(x-x_0)\delta(y-y_0)\delta(z-vt)\\ \vec{J}(\vec{x},t) &= qv\hat{z}\delta(x-x_0)\delta(y-y_0)\delta(z-vt).\end{aligned} \tag{3.49}$$

The analysis proceeds identically to that performed above but for clarity we write an intermediate equation

$$\vec{E}(\vec{x},\omega) = \frac{-iq}{v(2\pi)^{5/2}\epsilon_0\epsilon_r}e^{i\frac{\omega}{v}z}\int_{-\infty}^{\infty}\frac{k_x\hat{x}+k_y\hat{y}+\frac{\omega}{v}(1-\beta^2\epsilon_r)\hat{z}}{k_x^2+k_x^2+(1-\beta^2\epsilon_r)\frac{\omega^2}{v^2}}e^{-i\vec{k}_\perp\cdot\vec{x}_{\perp 0}}e^{i\vec{k}_\perp\cdot\vec{x}_\perp}\mathrm{d}^2\vec{k}_\perp, \tag{3.50}$$

with a result similar to that found in the previous section,

$$E_\rho(\vec{x},\omega) = \frac{q}{v(2\pi)^{3/2}\epsilon_0\epsilon_r}e^{i\frac{\omega}{v}z}\frac{\omega}{v}\sqrt{(1-\beta^2\epsilon_r)}K_1\big(\sqrt{(1-\beta^2\epsilon_r)}\frac{\omega}{v}(\rho-\rho_0)\big). \tag{3.51}$$

If we now look at the limiting form a $K_1(x)$ for $x \gg 1$ we find

$$E_\rho(\vec{x},\omega) = \frac{q}{v(2\pi)^{3/2}\epsilon_0\epsilon_r}\sqrt{\frac{\pi}{2(\rho-\rho_0)}}\sqrt{\frac{\omega}{v}\sqrt{(1-\beta^2\epsilon_r)}}e^{i\frac{\omega}{v}z}e^{-\frac{\omega}{v}\sqrt{(1-\beta^2\epsilon_r)}(\rho-\rho_0)}. \tag{3.52}$$

Thusly, if $\beta^2\epsilon_r < 1$, which is satisfied for a particle beam of any velocity in perfect vacuum, we see that the fields fall off exponentially in ρ so that there is no radiation. If on the other hand $\beta^2\epsilon_r > 1$ the exponent which contains $\sqrt{(1-\beta^2\epsilon_r)}$ produces an i and the fields are then seen to radiate away.

If we examine the exponent we find that the radiation is in phase when $z - \sqrt{(\beta^2\epsilon_r - 1)}\rho$ is a constant. The switching of $(\beta^2\epsilon_r - 1)$ is deliberate as it assumes $\beta^2\epsilon_r > 1$ and that the i has already been pulled out. Without loss of generality we can take this constant to be one. We can then show, through a bit of trigonometry

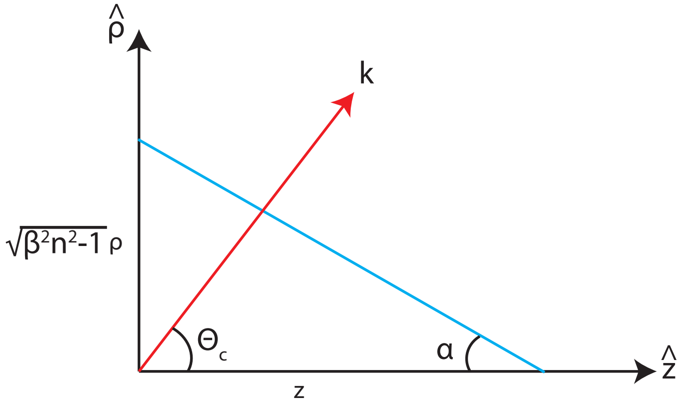

Figure 3.5: A diagram showing a line of constant phase front (shown in blue) as derived in Equation 3.52. The red arrow denotes the direction of propagation of the phase front.

as described by Figure 3.5,

$$\tan\alpha = \tan\frac{\pi}{2} - \theta_c = \cot\theta_c = \frac{1}{\sqrt{(\beta^2 n^2 - 1)}}, \tag{3.53}$$

which leads to

$$\cos\theta_c = \frac{1}{\beta n}. \tag{3.54}$$

Similar calculations can be performed to find the other field components, which when combined with the expression for the Poynting flux through a cylinder gives the radiation emitted per unit distance traveled [49],

$$\left(\frac{dE}{dx}\right)_{rad} \propto \int_{n>(1/\beta)} \omega \left(1 - \frac{1}{\beta^2 n^2}\right) \mathrm{d}\omega, \tag{3.55}$$

the formula derived by Tamm and Frank in 1937 [52].

The particles used in the experiment are accelerated to an energy of 20.35 GeV which means they have a velocity of 99.9999999685% the speed of light. To put it another way the velocity difference compared to the speed of light is in the 10th decimal. As air has an index of refraction of 1.000277, this beam will

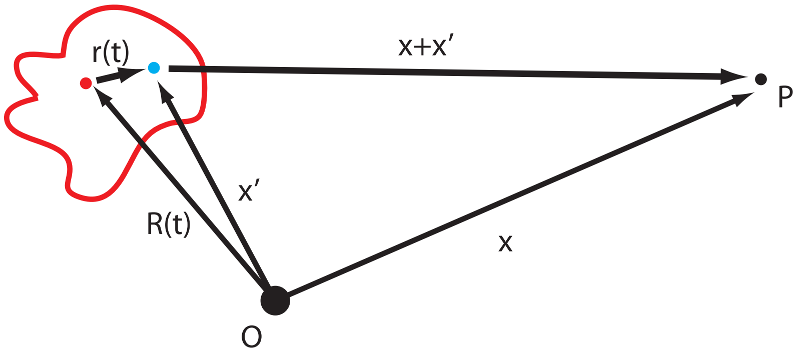

Figure 3.6: Diagram represention of the vectors used in the derivation of coherent radiation effects due to bunches of charged particles. In this diagram the red curved line represents a collection of charges which has a center of mass (red dot) that moves as $\vec{R}(t)$. The point O represents the origin of our chosen coordinate system and P the point of observation. A representative particle from the bunch is shown as a blue dot. The vectors $\vec{x}$, $\vec{x'}$ and $\vec{x}+\vec{x'}$ are an instance of the vectors defining the motion of the selected bunch particle. $\vec{r_{i,j}}(t)$ is the vector connecting the center of mass to the selected particle.

tend to radiate away energy when not in vacuum. If we assume a linear model for the scaling of index of refraction, 1+P/P$_0$ where P$_0$ is the pressure at STP, we find that such a beam stops radiating away energy as Cherenkov radiation at $7.6 * 10^{-4}$ torr. Cherenkov radiation in air is the origin of the light used in detector in the spectrometer in this experiment [53].

3.4 Coherent Radiation

We shall now derive an expression for bunches of particles radiating together. We shall see that if conditions are ideal the resulting radiation field increases as the square of the number of particles, N_p^2, as opposed to simply N_p.

To begin we start with the expression for energy radiated by a single charge, Eq. 3.1, and define everything outside of the exponential as $G(t)$:

$$\frac{d^2I}{d\omega d\Omega} = \Big|\sum_{i=1}^{N_p}\int_{-\infty}^{\infty} G(t)e^{i\omega(t-\hat{n}\cdot\frac{\vec{x}+\vec{x}'_i}{c})}dt\Big|^2, \tag{3.56}$$

where we have shown explicitly the vectorial relation between the particle of interest and the observation point, graphically represented in Fig. 3.6. Careful examination of Fig. 3.6 shows it is possible to write $\vec{x}+\vec{x'} = \vec{x}+\vec{R}(t)+\vec{r}(t)$, so for clarity we write:

$$\frac{d^2I}{d\omega d\Omega} = \Big|\sum_{i=1}^{N_p}\int_{-\infty}^{\infty} G(t)e^{i\omega(t-\hat{n}\cdot\frac{\vec{x}}{c}-\hat{n}\cdot\frac{\vec{R}(t)}{c}-\hat{n}\cdot\frac{\vec{r}_i(t)}{c})}dt\Big|^2. \tag{3.57}$$

The first two terms in the exponential are the same no matter which particle of the bunch is chosen, as long as the origin O remains the same, so we rewrite that term as $\phi(t)$. This leaves

$$\begin{aligned}\frac{d^2I}{d\omega d\Omega} &= \left(\sum_{i=1}^{N_p}\int_{-\infty}^{\infty} G(t)\phi(t)e^{-i\omega\hat{n}\cdot\frac{\vec{R}(t)}{c}}e^{-i\omega\hat{n}\cdot\frac{\vec{r}_i(t)}{c}}dt\right) * \\ &\quad \left(\sum_{j=1}^{N_p}\int_{-\infty}^{\infty} G^*(t)\phi^*(t)e^{i\omega\hat{n}\cdot\frac{\vec{R}(t)}{c}}e^{i\omega\hat{n}\cdot\frac{\vec{r}_j(t)}{c}}dt\right), \end{aligned}\tag{3.58}$$

where the superscript * represents the complex conjugate and the magnitude has been written explicitly.

If the individual particle positions, $\vec{r}_{i,j}(t)$, do not change with respect to the center of mass position $\vec{R}(t)$, the terms involving $\vec{r}(t)$ may be removed from the integral. What remains is the single particle energy radiated per unit solid angle per unit frequency. This function can be, for example, the expression given for transition radiation above in Eq. 3.5. Bundling up the expression for single particle radiation we arrive at the next step in the derivation:

$$\frac{d^2I}{d\omega d\Omega} = \sum_{i=1}^{N_p}\sum_{j=1}^{N_p} e^{-i\frac{\omega}{c}\hat{n}\cdot(\vec{r}_i-\vec{r}_j)}\frac{d^2I}{d\omega d\Omega}\bigg|_{s.p.}. \tag{3.59}$$

The rest of the derivation centers around examination of the double sum term. That is to say,

$$\sum_{i=1}^{N_p} \sum_{j=1}^{N_p} e^{-i\frac{\omega}{c}\hat{n}\cdot(\vec{r}_i - \vec{r}_j)} = ?. \tag{3.60}$$

As the sums are over the same physical distribution of particles, if $i = j$ then the exponential reduces to 1 and the sum to N_p. This leaves us to contend with the sum for all terms for which $i \neq j$. As the double sum is primarily concerned with the difference in the location of the two particles under examination $\vec{r}_i - \vec{r}_j$, we describe the two most obvious cases: 1) the particles are scattered in an arbitrarily large region compared to the wavelength of radiation of interest and 2) the particles are scattered in an arbitrarily small region compared to the wavelength of interest.

In the first case what results is the phase difference between each photon, $e^{-i\frac{\omega}{c}\cdot(\vec{r}_i - \vec{r}_j)}$, is such that the sum total of the double sum results in zero. An example of this is a uniform distribution of particles evenly distributed along a full wavelength of the radiation of interest. A particle that emits a photon with a phase $\phi = \pi$ (not to be confused with $\phi(t)$ defined earlier, which is the same for all particles by definition) constructively interferes with a particle which emits a photon with a phase of $\phi = 0$. Such radiation is called *incoherent*, and its magnitude is equal to the radiation due to a single particle times the number of particles radiating, N_p. Evidently, in order for the terms in the double sum for which $i \neq j$ to matter, the beam must be short compared to a wavelength.

The second case listed above, in which a bunch of particles is distributed over a region small compared to the wavelength of interest, results in an N_p^2 enhancement of the the radiation field. Such radiation is said to be *coherent*. Performing a *gedanken* similar to the one above, we imagine a bunch of particles infinitely short compared to the wavelength of interest. This results in the phase factors, $e^{-i\frac{\omega}{c}\cdot(\vec{r}_i-\vec{r}_j)}$, individually reducing to unity. But how many phase factors are there? As the sums are to be performed for $i \neq j$, for $i, j \in 1...N_p$, each particle i (of which there are N_p) has a phase factor pairing it with $N_p - 1$ other particles (from j). This means that there are $N_p(Np - 1)$ terms in the double sum for $i \neq j$. Add to this term the result from the $i = j$ case and the N_p^2 result is evident.

To be more explicit in the derivation of the energy radiated by a bunch of charged particles we now derive an expression for the energy radiated for a charge bunch which is not readily described by either of the above two cases. To do so we begin by defining:

$$\frac{d^2I}{d\omega d\Omega} = \left(N_p + [N_p(N_p-1)]f(\omega)\right)\frac{d^2I}{d\omega d\Omega}\bigg|_{s.p.} \tag{3.61}$$

$$f(\omega) \equiv \frac{1}{N_p(N_p-1)}\sum_{i=1}^{N_p}\sum_{j\neq i}^{N_p} e^{-i\frac{\omega}{c}\hat{n}\cdot(\vec{r}_i-\vec{r}_j)}. \tag{3.62}$$

This formulation of the problem of coherence allows us to state the "degree of coherence" by calculating $f(\omega)$, which returns the expected incoherent expression for $f(\omega) \rightarrow 0$ and coherent expression for $f(\omega) \rightarrow 1$. Explicit calculation of $f(\omega)$ would prove difficult for systems in which $N_p \rightarrow \infty$, so we resort to an ensemble averaging technique used commonly in plasma physics [54]. We define a distribution of point like particles as $N_i(\vec{r}) = \frac{1}{N_p}\sum_i \delta(\vec{r}-\vec{r}_i) = f_i(\vec{r}) + \delta N_i(\vec{r})$. In this unfortunate notation, $f_i(\vec{r})$ is not the same as $f(\omega)$ but they are related. Specifically $f_i(\vec{r})$ is the $distribution function$ of the particle bunch in real space. The distribution function represents the smooth part of N_i while $\delta N_i(\vec{r})$ represents the spiky nature of N_i which is due to the discrete nature of the particles.

In the limit that the number of particles becomes extremely large, the sums written above can be converted to integrals. Using the definition of $N_i(\vec{r})$ allows us to write:

$$\frac{1}{N_p}\left\langle \sum_{i=1}^{N_p} e^{-i\frac{\omega}{c}\hat{n}\cdot\vec{r}_i}\right\rangle = \left\langle \int_{\mathbf{R}^3} e^{-i\frac{\omega}{c}\hat{n}\cdot\vec{r}} N_i(\vec{r}) d^3\vec{r}\right\rangle = \int_{\mathbf{R}^3} e^{-i\frac{\omega}{c}\hat{n}\cdot\vec{r}} f_i(\vec{r}) d^3\vec{r}. \tag{3.63}$$

Where we have taken advantage of the fact that the ensemble average of the spiky function is zero, $\langle \delta N_i(\vec{r})\rangle = 0$. Writing the double sum from the expressions above using this same method yields:

$$\frac{1}{N_p^2}\left\langle \sum_{i=1}^{N_p} e^{-i\frac{\omega}{c}\hat{n}\cdot\vec{r}_i} \sum_{j=1}^{N_p} e^{i\frac{\omega}{c}\hat{n}\cdot\vec{r}_j}\right\rangle = \int_{\mathbf{R}^3} d^3r \int_{\mathbf{R}^3} d^3r' e^{-i\frac{\omega}{c}\hat{n}\cdot(\vec{r}-\vec{r}')} \Big\langle N_i(\vec{r}) N_j(\vec{r}')\Big\rangle. \tag{3.64}$$

Explicitly writing out the ensemble average on the right hand side of the previous equation gives:

$$\begin{aligned} \langle N_i(\vec{r}) N_j(\vec{r}')\rangle &= \Big\langle (f_i(\vec{r}) + \delta N_i(\vec{r}))(f_j(\vec{r}') + \delta N_j(\vec{r}'))\Big\rangle, & (3.65)\\ &= f_i(\vec{r}) * f_j(\vec{r}') + f_i(\vec{r}) * \Big\langle \delta N_j(\vec{r}'))\Big\rangle & (3.66)\\ &+ f_j(\vec{r}') * \Big\langle \delta N_i(\vec{r})\Big\rangle + \Big\langle \delta N_i(\vec{r}) * \delta N_j(\vec{r}'))\Big\rangle. \end{aligned}$$

The second and third elements of Eq. 3.66 are identically zero. The fourth term, the product of the two spiky functions, can be shown to vanish in the limit of large numbers of particles [33]. This leads to,

$$\frac{1}{N_p^2}\left\langle \sum_{i=1}^{N_p} e^{-i\frac{\omega}{c}\hat{n}\cdot\vec{r}_i} \sum_{j=1}^{N_p} e^{i\frac{\omega}{c}\hat{n}\cdot\vec{r}_j}\right\rangle = \int_{\mathbf{R}^3} d^3r \int_{\mathbf{R}^3} d^3r' e^{-i\frac{\omega}{c}\hat{n}\cdot(\vec{r}-\vec{r}')} f_i(\vec{r}) f_i(\vec{r}'), \tag{3.67}$$

and as $fi(\vec{r})$ is a probability density function and thus necessarily positive and real, $f_i^*(\vec{r}) = f_i(\vec{r})$, giving,

$$\frac{1}{N_p^2}\left\langle \sum_{i=1}^{N_p} e^{-i\frac{\omega}{c}\hat{n}\cdot\vec{r}_i} \sum_{j=1}^{N_p} e^{i\frac{\omega}{c}\hat{n}\cdot\vec{r}_j}\right\rangle = \left| \int_{\mathbf{R}^3} d^3r e^{-i\frac{\omega}{c}\hat{n}\cdot\vec{r}} f_i(\vec{r})\right|^2. \tag{3.68}$$

Returning now to Eqs. 3.61 and 3.62, we see that

$$\frac{1}{N_p^2}\left\langle \sum_{i=1}^{N_p} e^{-i\frac{\omega}{c}\hat{n}\cdot\vec{r}_i} \sum_{j=1}^{N_p} e^{i\frac{\omega}{c}\hat{n}\cdot\vec{r}_j}\right\rangle = \frac{1}{N_p} + \frac{N_p(N_p+1)}{N_p^2}\left\langle \sum_{i=1}^{N_p} \sum_{j\neq i}^{N_p} e^{-i\frac{\omega}{c}\hat{n}\cdot(\vec{r}_i-\vec{r}_j})\right\rangle. \tag{3.69}$$

Equating the last two equations, and taking $N_p >> 1$, leads to the final result,

$$f(\omega) = \left\langle \sum_{i=1}^{N_p} \sum_{j \neq i}^{N_p} e^{-i\frac{\omega}{c}\hat{n}\cdot(\vec{r}_i - \vec{r}_j)} \right\rangle = \left| \int_{\mathbf{R}^3} d^3 r e^{-i\frac{\omega}{c}\hat{n}\cdot\vec{r}} f_i(\vec{r}) \right|^2 . \tag{3.70}$$

What we see is that the degree of coherence of a bunch of particles is the square of the Fourier Transform of the distribution function of the beam. Examination of $f(\omega)$ in the limits that the bunch length goes either infinitely short or infinitely long shows that, as expected, as the bunch length becomes shorter the beam becomes more coherent,

$$f(\omega) \to \begin{cases} 1 & \text{as } \sigma_z \to 0 \\ 0 & \text{as } \sigma_z \to \infty. \end{cases} \tag{3.71}$$

Specifically $f(\omega)$ allows one to describe the degree of coherence of the radiation generated in a given process.

3.5 Kramers-Kronig and Pulse Reconstruction

Now that we have a description of the frequency content of radiation generated from various sources, we seek to find a way to use that spectral content to generate a profile of what the radiation source might look like. Phase retrieval problems such as these are studied in detail due to their applicability in optics [55] and have been of interest for at least 60 years [56]. The experiments presented in this work are specifically concerned with the one dimensional phase retrieval problem, which in general is considered hopeless [57, 58, 59]. It has, however, been shown that under certain circumstances [60, 61, 62, 63] some details of the source distribution are retrievable.

We begin with a description of the problem of phase retrieval and a derivation of the Kramers-Kronig relations. We then outline the limits of such phase retrieval attempts as applied to Coherent Transition Radiation (CTR) and show heuristically that some details of the radiation source are recoverable.

3.5.1 Phase Retrieval

Given the relatively slow response time of most detectors, on the order of a picosecond [64], in order to measure the temporal profile of a light pulse which is shorter than the response time of the detector other techniques, such as autocorrelation, are necessary [65]. Such techniques suffer from the fact that they do not give any phase information, only spectral intensity. We are thus interested in trying to recover the phase information from the spectral intensity or show that the phase wasn't necessary for the measurements we wish to make.

In its most general form the so called one dimension phase retrieval problem[1] can be initiated with a function which is complex in the time domain, such as $E(t) = E_0 e^{-i\omega t}$, so that the Fourier transform is written as,

$$f(\omega) = r(\omega)e^{i\phi(\omega)} = \int_{-\infty}^{\infty} \rho(t)e^{i\psi(t)}e^{i\omega t}\,\mathrm{d}t, \tag{3.72}$$

where the magnitude and phase of the functions in both domains have been explicitly written out. The question arises as to whether one can determine $f(t)$, or $f(\omega)$, given only $r(\omega)$. A proof of lack of uniqueness of a Fourier inverse determined using $r(\omega) = |f(\omega)|$ follows directly from comparison of two functions with the same spectral intensity $r(\omega)$ but different spectral phases $\phi(\omega)$,

$$\begin{aligned} h(t) &= \frac{1}{2\pi}\int_{-\infty}^{\infty} r(\omega)e^{-i\omega t}\,\mathrm{d}\omega \\ g(t) &= \frac{1}{2\pi}\int_{-\infty}^{\infty} r(\omega)e^{i\phi(\omega)}e^{-i\omega t}\,\mathrm{d}\omega. \end{aligned} \tag{3.73}$$

---

[1] There is no phase retrieval problem in two dimensions [66], but that is beyond the scope of this text.

From this it is easily seen that $r(\omega) = |\tilde{h}(\omega)| = |\tilde{g}(\omega)|$ but that $h(t) \neq g(t)$, so that $r(\omega) = |f(\omega)|$ is insufficient to completely determine $f(t)$. The result obtained from using $r(\omega)$ alone is ambiguous, and infinitely so. In retrospect this may have been entirely obvious given the relationship between the magnitude and phase of complex numbers. That is to say, a point on the complex plane is defined by a magnitude and phase, the use of magnitude alone produces a circle.

This type of analysis can be extended to the discrete Fourier transform,

$$F_k \equiv \sum_{n=0}^{N-1} f_n e^{i\frac{2\pi k}{N}n} = \sum_{n=0}^{N-1} f_n z^n, \tag{3.74}$$

where f_n are a series of data points. Use of the Fundamental Theorem of Algebra [67] states that a polynomial of one variable of degree n has n roots, so it may be written as a product of those roots, $F_k = \sum_{n=0}^{N-1} a_n(z - z_n)$. It is easily seen that an arbitrary phase added to the mth root, $(z - z_m) \rightarrow (z - z_m)e^{ip}$, does not effect the magnitude $|F_k|$, so that we are again left with an ambiguity when attempting to use $|F_k|$ to determine f_n [68].

3.5.2 A Kramers-Kronig Derivation

If the response of a system, $H(t)$, to a stimulus $f(t)$ is written in typical Green's function format as

$$H(t) = \int_{-\infty}^{\infty} G(t - t')f(t')\mathrm{d}t', \tag{3.75}$$

and the Fourier Transform [69] of the Green's function and the stimulus term are given as,

$$\begin{aligned} G(t - t') &= \frac{1}{\sqrt{2\pi}} \int_{-\infty}^{\infty} e^{i\omega(t-t')} G(\omega)\,\mathrm{d}\omega \\ f(t') &= \frac{1}{\sqrt{2\pi}} \int_{-\infty}^{\infty} e^{i\omega' t'} f(\omega')\,\mathrm{d}\omega', \end{aligned} \tag{3.76}$$

with their inverse transforms given by[2],

$$
\begin{aligned}
G(\omega) &= \frac{1}{\sqrt{2\pi}} \int_{-\infty}^{\infty} e^{-i\omega(t-t')} G(t-t')\,\mathrm{d}t \\
f(\omega) &= \frac{1}{\sqrt{2\pi}} \int_{-\infty}^{\infty} e^{-i\omega' t} f(t)\,\mathrm{d}t,
\end{aligned} \tag{3.77}
$$

it follows then that

$$H(\omega) = G(\omega) f(\omega). \tag{3.78}$$

It is thus seen that the response of a system in the Fourier domain is a mere product of the Green's function and the stimulating function. If $G(\omega)$ is analytic [70] in the upper half of the complex plane it follows from Cauchy's Integral Theorem [30] that,

$$\oint \frac{G(\omega')}{\omega' - \omega}\,\mathrm{d}\omega' = 0, \tag{3.79}$$

which through application of the residue theorem gives,

$$G(\omega) = \frac{1}{i\pi} \mathrm{P} \int_{-\infty}^{\infty} \frac{G(\omega')}{\omega' - \omega} \mathrm{d}\omega'. \tag{3.80}$$

If $G(\omega)$ is now split into real and imaginary components we then arrive at one version of the Kramers-Kronig relations:

$$
\begin{aligned}
\mathrm{Re}[G(\omega)] &= \frac{1}{\pi} \mathrm{P} \int_{-\infty}^{\infty} \frac{\mathrm{Im}[G(\omega')]}{\omega' - \omega} \mathrm{d}\omega' \\
\mathrm{Im}[G(\omega)] &= -\frac{1}{\pi} \mathrm{P} \int_{-\infty}^{\infty} \frac{\mathrm{Re}[G(\omega')]}{\omega' - \omega} \mathrm{d}\omega'.
\end{aligned} \tag{3.81}
$$

Through simple demands that $G(t-t')$ be a real function, which it should be if the response to a real stimulus $f(t')$ is to be real, it can be shown that $G(-\omega) = G^*(\omega)$. This means that $G_{real}(-\omega) = G_{real}(\omega)$ and $G_{Im}(-\omega) = -G_{Im}(\omega)$ and,

$$
\begin{aligned}
\mathrm{Re}[G(\omega)] &= \frac{2}{\pi} \mathrm{P} \int_{0}^{\infty} \frac{\omega' \mathrm{Im}[G(\omega')]}{\omega'^2 - \omega^2} \mathrm{d}\omega' \\
\mathrm{Im}[G(\omega)] &= -\frac{2\omega}{\pi} \mathrm{P} \int_{0}^{\infty} \frac{\mathrm{Re}[G(\omega')]}{\omega'^2 - \omega^2} \mathrm{d}\omega'.
\end{aligned} \tag{3.82}
$$

---

[2] When solving for the Principal Value in the above expression it is necessary to briefly return to definition of the $G(\omega)$, Equation 3.77. Care should be taken that causality is always obeyed, so that if $\omega = \omega_R + i\omega_I$ and $t - t' < 0$ that the contour is closed in the lower half of the complex plane.

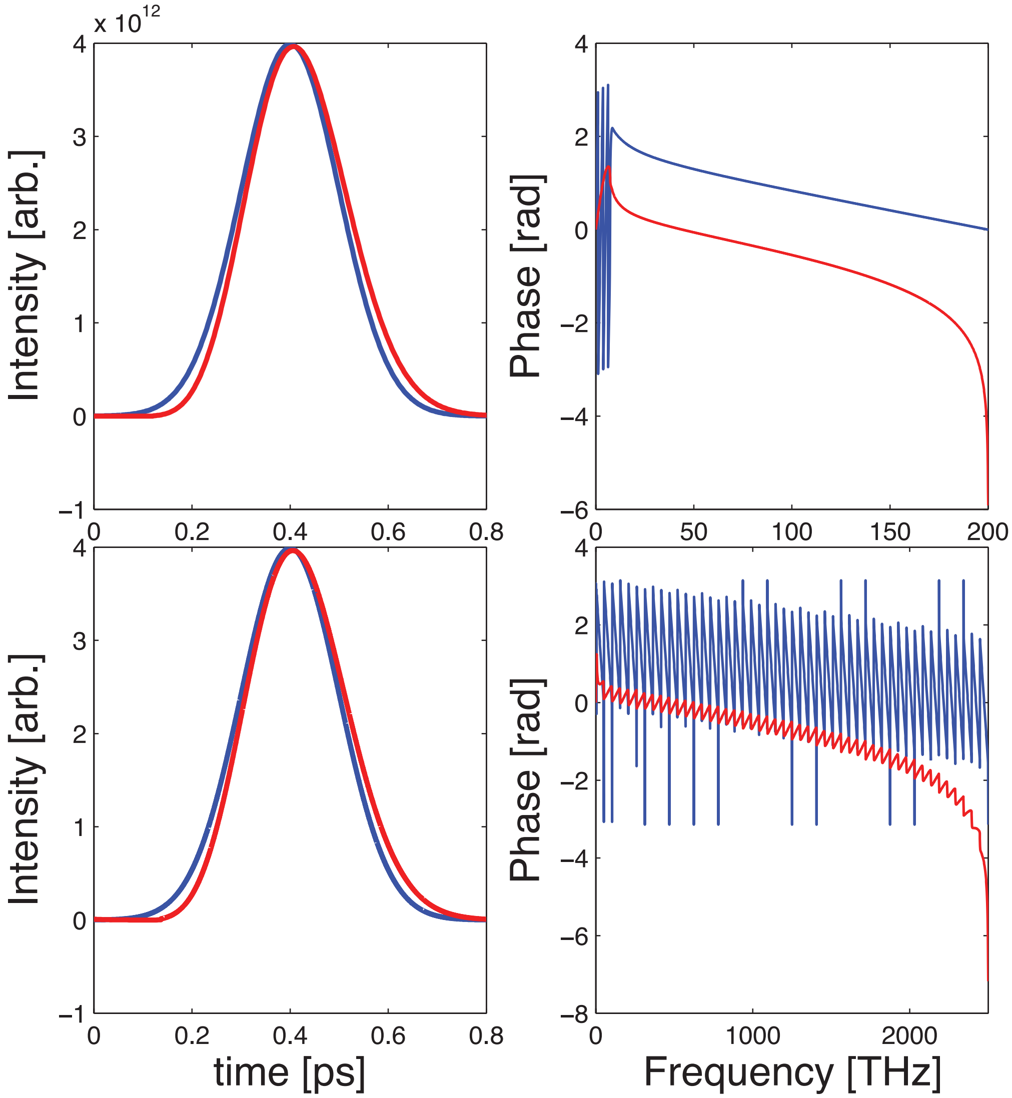

Figure 3.7: An example of a Kramers-Kronig reconstruction of a time-bandwidth limited Gaussian pulse of $\sigma_t = 100$ fs. The input pulse and phase are shown in blue and the minimum phase reconstruction is shown in red. For the top set a window 100 σ_t wide was divided up into 4000 points for this reconstruction. For the bottom the window was 8 σ_t wide and divided into 4000 points.

3.5.3 Transition Radiation, Bunch Shapes and Phase Retrieval

Despite a previous section outlining that phase retrieval in one dimension is understood to be impossible, we now show heuristically that some details of a radiation pulse can be determined from the spectral content of the radiation alone, under certain circumstances. Starting from Eq. 3.61 we note that in the one dimensional limit the bunch form factor $f(\omega)$ reduces to,

$$f(\omega) = \left| \int_{-\infty}^{\infty} f(z) e^{-i\frac{\omega}{c}z} \, \mathrm{d}z \right|^2 = \left| \hat{F}(\omega) \right|^2, \tag{3.83}$$

the magnitude squared of the Fourier Transform. The natural log of the Fourier components of the pulse distribution is taken giving

$$\ln(\hat{F}(\omega)) = \ln(r(\omega)) + i\phi(\omega), \tag{3.84}$$

where $\hat{F}(\omega) = r(\omega)e^{i\phi(\omega)}$ has been used. The Kramers-Kronig relations may be applied such that a minimum phase approximation can be determined using,

$$\phi_{min}(\omega) = -\frac{2\omega}{\pi} \mathrm{P} \int_0^{\infty} \frac{\ln(r(\omega))}{\omega'^2 - \omega^2}. \tag{3.85}$$

Using the above equation an approximation to the generating pulse can be derived by performing the inverse Fourier transform using $r(\omega)$ and $\phi_{min}(\omega)$.

Figure 3.7 provides an example of the process of minimum phase reconstruction for a time-bandwidth limited Gaussian pulse. For such a pulse the expected phase is constant and zero as the Fourier transform of a Gaussian pulse is purely real. The deviations visible in the figure are due to machine limits in calculating Fourier coefficients and the cut-offs due to the inability to numerically calculate out to infinity. The "actual" phase and the reconstructed phase appear to agree well for most frequencies up to a constant phase offset. This is confirmed by the similarity in the reconstructed pulse when compared to the input pulse.

The above analysis indicates that despite the limitations of a theoretically irretrievable phase and the limitations that exist in making an actual measurement, a fair reproduction of a Gaussian beam is possible. This close agreement can be explained by arguments involving the locations of the zeros of the Fourier transform in the complex plane [60, 71]. We expand on a single Gaussian attempt with a reconstruction of a pair of Gaussian pulses of identical width, but uneven in amplitude and offset, Figure 3.8. We see that while the details of the pulses are qualitatively correct the order in which the pulses are recovered is not. A minimum phase approximation gets the qualitative bunch shapes correct but will always place the large bunch first. Thus, absent other information, it is not possible to determine the order of arrival of the bunches.

Next we show that when attempting to reconstruct a single Gaussian that the phase is almost irrelevant, Figure 3.9. The agreement in Figure 3.9.c is unsurprising in that a Gaussian offset from zero has linear phase, in the Eq. 3.84 representation. For the last case, Figure 3.9.d, it can be seen that if the radiation were to have an interesting phase function $\phi(\omega)$, but Gaussian spectral intensity, the minimum phase reconstruction would still return a Gaussian.

If one tries to reconstruct a series of Gaussians of equal amplitude and duration but of non-periodic spacing, the minimum phase approximation fails, Figure 3.10. This is to be expected as it violates the previously stated criterion that a minimum phase reconstruction works as long as the weak bunches follow strong ones [60]. It is noted, but not shown, that the minimum phase reconstruction of identical and periodically spaced Gaussian pulses does appear to work.

Finally, we attempt a minimum phase reconstruction of a selection of non-symmetric and non-Gaussian bunches to illustrate the limits of the process, Figure 3.11. From these demonstrations it is obvious that in general the minimum

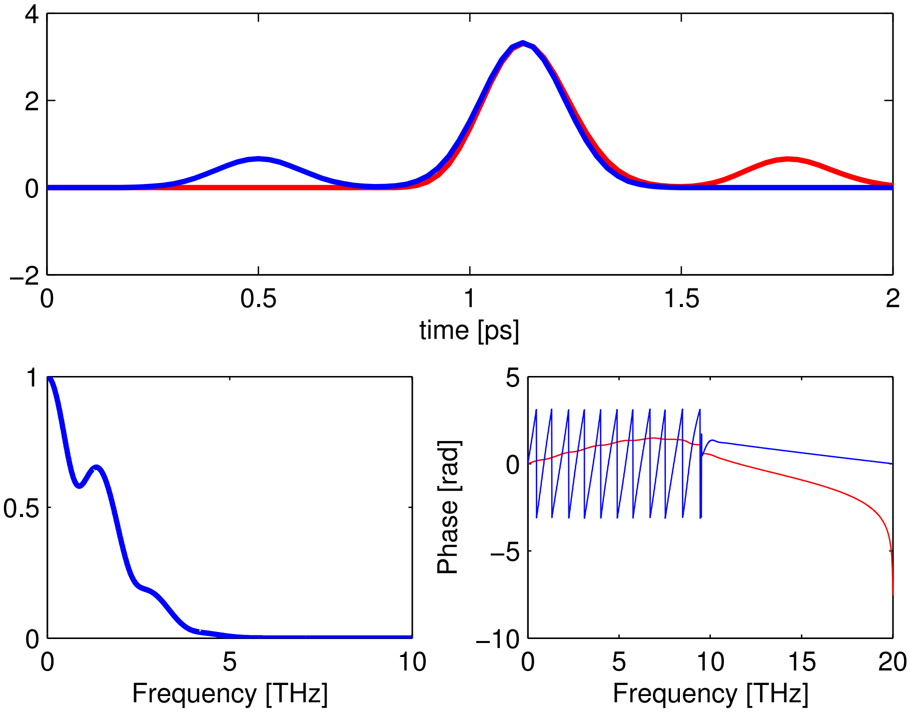

Figure 3.8: A reconstruction of a pair of Gaussians of equal width σ_t=100 fs but offset by some 600 fs, and the initial pulse is one fifth the amplitude of the trailing pulse. Shown in the top frame is the original pulse in blue and the reconstruction in red. The bottom left shows the spectrum and the bottom right the phases of the two pulses.

phase reconstruction cannot provide any information about the head-tail order, even for fairly asymmetric bunches. It does seem to return an appropriate measure of the beam lenth. Furthermore, for certain symmetric shapes like square pulses the method does not recover the proper pulse length.

When attempting to reconstruct a bunch profile from Coherent Transition Radiation care must be taken as the methods used to measure the radiation's temporal profile, such as autocorrelation, naturally broaden the pulse as measured.

Furthermore, autocorrelation techniques always return a symmetric profile even when the input profile is not symmetric. These broadening and symmetrizing effects must be kept in mind when attempting to use a phase retrieval technique on data to obtain information about the initial pulse. A deeper discussion of these and other challenges can be found in the references, specifically References [60, 61, 64].

A final note on the subject of using transition radiation as a bunch length diagnostic that should be mentioned is that the spectrum of the emitted light has a necessary cut off at the plasma frequency of the metal used to generate the radiation. Furthermore, the form factor $f(\omega)$ as derived is a function purely of the physical extent of the beam so we do not expect effects like frequency-position correlations, or chirps, which might add additional ambiguity to the minimum phase reconstruction.

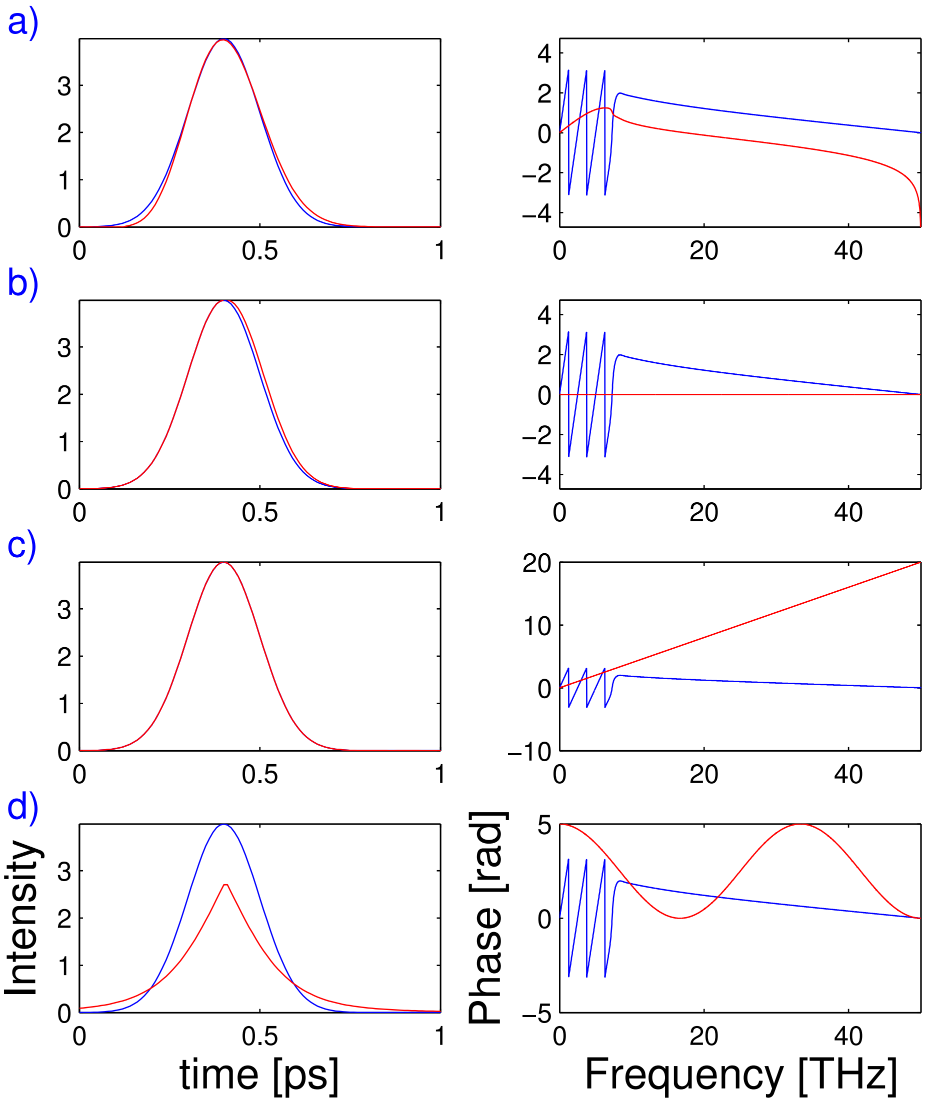

Figure 3.9: A comparison of the reconstructed pulses using user defined phases, but the spectrum from a single seed Gaussian of σ_t=100 fs with an offset of $\tau = 4\sigma_t$. a) The minimum phase approximation as described by Lai and Sievers [60, 61]. b) Zero phase is assumed. c) A linear phase is used. d) A cosine plus an offset is in phase is input. For all plots the blue curves represent the original function and the red the minimum phase reconstruction.

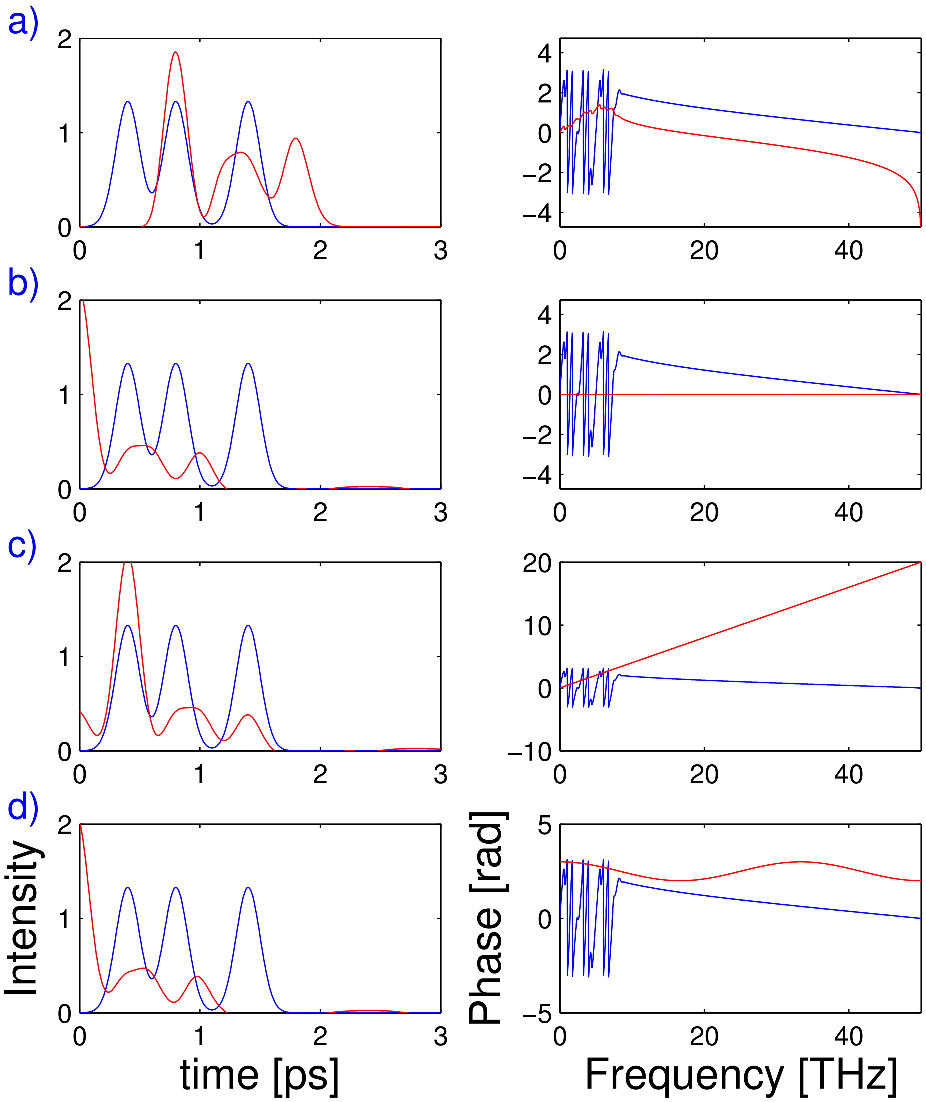

Figure 3.10: A comparison of the reconstructed pulses using user defined phases, but the spectrum from three Gausisan of identical $\sigma_t = 100$ fs, but offsets from zero of $\tau_1 = 400$ fs,$\tau_2 = 800$ fs,$\tau_3 = 1400$ fs. a) The minimum phase approximation as described by Lai and Sievers [60, 61]. b) Zero phase is assumed. c) A linear phase is used. d) A cosine plus an offset is input. For all plots the blue curves represent the original function and the red the minimum phase reconstruction.

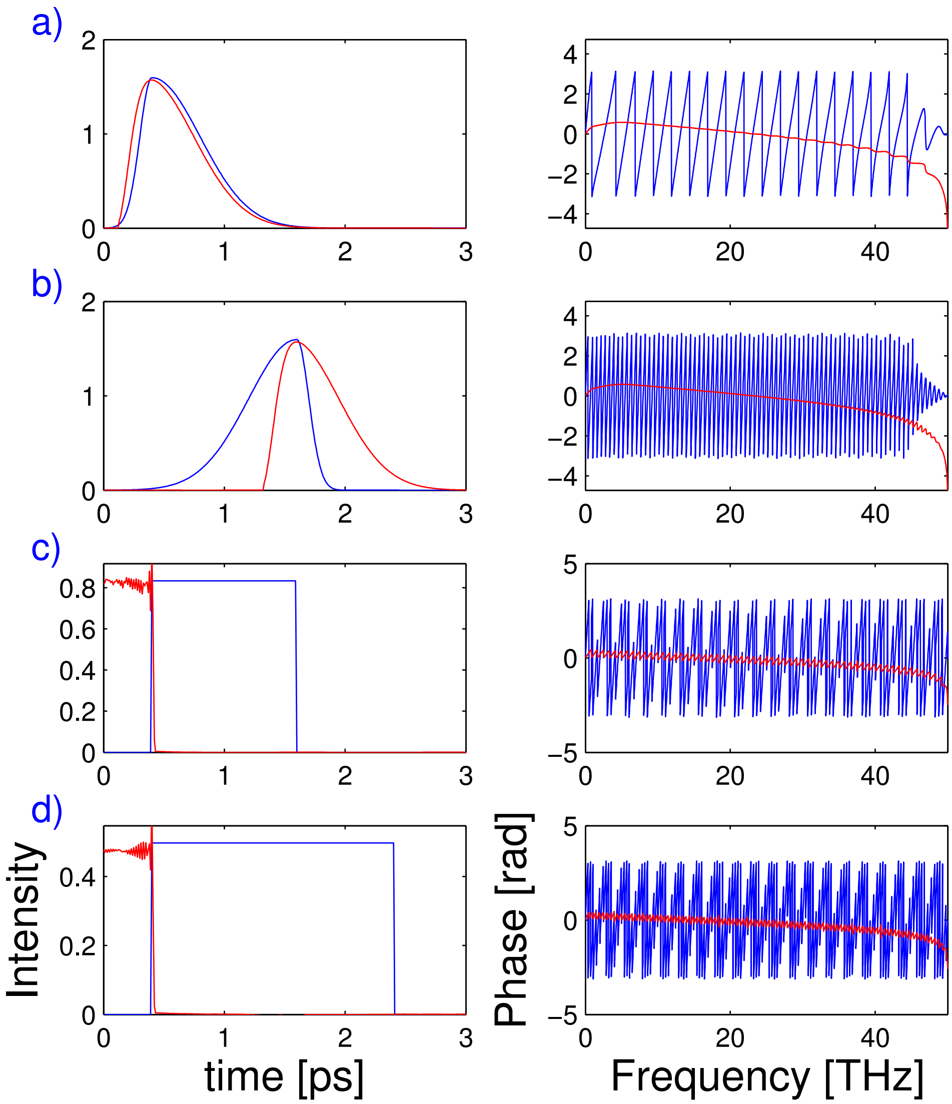

Figure 3.11: A comparison of the reconstructed pulses using asymmetric or non-Gaussian shapes. a) Is an asymmetric gaussian where the first half is a Gaussian of width $\sigma_t = 100$ fs and the second half is of width $\sigma_t = 400$ fs. b) the same as a) but reversed in time. c) A square pulse with a width of 300 fs. d) A square pulse with a width of 500 fs. As before, blue represents the original pulse and red the minimum phase reconstruction.

CHAPTER 4

Wakefields and Accelerators

Accelerator physicists are looking for technologies to increase the average gradient in new systems past the present limit of $\sim$20 MVm^{-1} [72] in traditional room temperature copper structures. The end goal of such research is not only reduction in size of present accelerating complexes, from kilometers to a kilometer or less, but for the creation of high energy, compact beam sources that pave the way for the next generation of radiation sources which operate in bands heretofore difficult to access, such as terahertz [25] and x-rays [18].

In this section we explore the use of novel devices called wakefield accelerators that utilize a drive-witness configuration to transfer energy from the drive beam to the witness beam. Such structures are capable of sustaining fields in the region of >1 GVm^{-1} in the case of dielectrics and >10 GVm^{-1} [26] in the case of plasmas [1, 2]. In this section we derive some of the more common relations used when describing wakefield accelerators.

Any structure that can effectively add energy to a passing particle beam by definition also effectively removes energy from the beam; good accelerators are good decelerators. Such a simple statement, otherwise known as beam loading, gave rise to the study of wakefields in accelerating structures. The first of these important relations presented here is the relationship between the voltage excited in a structure by a passing beam and the voltage "seen" by the passing beam. This relation is known as *fundamental theorem of beam loading* or *fundamental theorem*

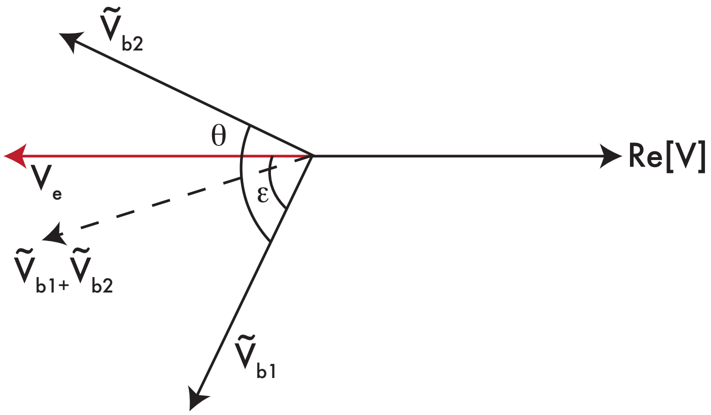

Figure 4.1: A phasor diagram representing the wakefield system under study in this section. The quantity $\tilde{V}_{b1}$ represents the beam induced voltage after the first pass through the system, whereas $\tilde{V}_{b2}$ is that same voltage after n oscillations, less a small quantity of phase Θ.

of wakefields. We follow this with a derivation of the *Panofsky-Wenzel theorem* which will set constraints on what our wakefields must look like in order to best accelerate beams of finite size. Next, we provide a few remarks about the nature of superposition and wakefields generated by bunches of particles and finally we discuss transformer ratios and their importance in wakefield accelerators.

4.1 The Fundamental Theorem of Wakefields

We seek to show that the field seen by a particle is one half the beam-induced voltage in the structure. In doing so we follow the method as demonstrated by Wilson using energy conservation [73].

We start by asserting the energy stored in the structure as:

$$W = \alpha V^2, \tag{4.1}$$

where V is the cavity voltage. We allow that the field seen by the particle is some fraction of the beam induced cavity voltage V_b, $V_e = fV_b$. We further allow that the phase of the field seen by the particle differs from the phase of the beam-induced voltage by some quantity ε. We next assume that after an initial pass through the structure the beam then passes through the structure again; the mechanism for steering the particle back through the structure is assumed to be lossless but otherwise arbitrary. The time it takes the particle to again enter the structure is assumed to be some integer number of oscillations of the mode in question plus another component $\Theta < 2\pi$, and that the structure is lossless such that the magnitude of the beam-induced voltage created on the first pass is preserved.

Beginning with Eq. 4.1 we find the stored energy after the second pass through the structure is:

$$\begin{aligned} W &= \alpha(\tilde{V}_{b2} + \tilde{V}_{b1})^2, \\ &= 2V_b^2\alpha(1 + \cos\theta) \end{aligned} \tag{4.2}$$

where a tilde is used to denote a complex quantity and V_b is the magnitude of the beam-induced voltage.

Next we derive and expression for the energy lost by the particle:

$$\begin{aligned} \Delta u &= qV_e + qV_e + qV_b\cos(\Theta - \varepsilon), \\ &= qV_b(2f + \cos(\Theta - \varepsilon)) \end{aligned} \tag{4.3}$$

where the first term on the right hand side is the energy lost during the particle's first trip through the structure and the remaining two terms are the energy lost during its second trip. We see here explicitly the beam-induced voltage remaining in the structure after the first pass through the structure. Energy conservation demands that Eqs. 4.2 and 4.3 be equal given no other source of energy or energy loss in the system as described. We then collect terms with the same functional dependence on Θ; Θ is the only quantity which may be varied by the user and thus its behavior is not determined by the wakefield structure in question,

$$(2\alpha V_b - 2qf) + (2\alpha V_b - q\cos\varepsilon)\cos\Theta - q\sin\varepsilon\sin\Theta = 0. \tag{4.4}$$

To satisfy the above equation all non-theta terms must simultaneously vanish giving:

$$\begin{aligned} V_b &= \frac{qf}{\alpha}, \\ V_b &= \frac{q\cos\varepsilon}{2\alpha}, \\ 0 &= qsin\varepsilon. \end{aligned} \tag{4.5}$$

The last of Eq. 4.5 requires that $\varepsilon = 2\pi n$, for $n \in \mathbb{Z}$, requiring the beam-induced voltage and the field seen by the particle to be in phase. The $2n + 1$ terms are omitted as they would involve the particle take energy from a structure which initially is stated to contain none. Combining the first two equations of Eqs. 4.5 and making use of $cos(2\pi n) = 1$ yields $f = \frac{1}{2}$. Thus the field seen by the particle is half the beam-induced voltage V_b.

4.2 Panofsky-Wenzel Theorem

Next we seek to show that for accelerating systems that have a clear boundary where the interaction with the particle beam is terminated there is no longitudinal variation in the transverse momentum kick if there is no transverse variation in the longitudinal kick. This relation is most often referred to as the Panofsky-Wenzel theorem [74]. While its definition can be rather verbose it serves a key roll in accelerator physics in that when building an accelerating structure one typically does not want to induce longitudinally varying transverse momentum kicks in the beam while accelerating it.

To begin we start with the Lorentz force acting on a particle moving along the $\hat{z}$-axis at constant velocity, a very good assumption for relativistic beams ($v \simeq c$),

$$\frac{\mathrm{d}\vec{p}}{\mathrm{d}t} = e\bigg(-\vec{\nabla}\phi - \frac{1}{c}\frac{\partial \vec{A}}{\partial t} + \frac{\vec{v}}{c} \times (\vec{\nabla} \times \vec{A})\bigg) \tag{4.6}$$

where we have immediately written the Lorentz force in terms of potentials. Rewriting the last term on the right hand side of Eq. 4.6 yields the convective derivative which can be converted to the total time derivative,

$$\begin{aligned} \frac{\mathrm{d}\vec{p}}{\mathrm{d}t} =& e\bigg(-\vec{\nabla}\phi - \frac{1}{c}\frac{\partial \vec{A}}{\partial t} + (\frac{\tilde{\vec{v}}}{c} \cdot \vec{\nabla}\tilde{\vec{A}}) - (\frac{\vec{v}}{c} \cdot \vec{\nabla})\vec{A}\bigg) \\ \frac{\mathrm{d}\vec{p}}{\mathrm{d}t} =& e\bigg(-\vec{\nabla}\phi - \frac{1}{c}\frac{\mathrm{d}\vec{A}}{\mathrm{d}t} + (\frac{\tilde{\vec{v}}}{c} \cdot \vec{\nabla}\tilde{\vec{A}})\bigg) \\ \frac{\mathrm{d}}{\mathrm{d}t}\bigg(\vec{p} + \frac{e}{c}\vec{A}\bigg) =& e\vec{\nabla}\bigg(\frac{v}{c}A_z - \phi\bigg), \end{aligned} \tag{4.7}$$

where the $\sim$ is used in place of the Hestenes overdot, which can be confused for the time derivative. Using Eq. 4.7 we now separate the momentum kicks into transverse and longitudinal parts.

$$\begin{aligned} \frac{\mathrm{d}}{\mathrm{d}t}\bigg(\vec{p} + \frac{e}{c}\vec{A}\bigg)_{\perp} &= e\vec{\nabla}_{\perp}\bigg(\frac{v}{c}A_z - \phi\bigg) \\ \frac{\mathrm{d}}{\mathrm{d}t}\bigg(\vec{p} + \frac{e}{c}\vec{A}\bigg)_{z} &= e\frac{\partial}{\partial z}\bigg(\frac{v}{c}A_z - \phi\bigg). \end{aligned} \tag{4.8}$$

If we integrate from the beginning of the interaction to the end, and remember that the interaction is terminated at both ends such that the fields (and their potentials) vanish at those points we are left with:

$$\begin{aligned} \Delta p_{\perp} &= e\vec{\nabla}_{\perp}\int_{0}^{t'} \mathrm{d}t\bigg(\frac{v}{c}A_z - \phi\bigg) \\ \Delta p_{z} &= e\frac{\partial}{\partial z}\int_{0}^{t'} \mathrm{d}t\bigg(\frac{v}{c}A_z - \phi\bigg). \end{aligned} \tag{4.9}$$

If the longitudinal derivative of the transverse kick is taken and the transverse derivative of the longitudinal kick we arrive at the final form of the Panofsky-Wenzel theorem,

$$\frac{\partial}{\partial z}\Delta p_{\perp} = \nabla_{\perp}\Delta p_{z}. \tag{4.10}$$

4.3 Superposition of Wakes

We are now interested in the wakefield generated not just by a single driving charge but by a collection of charges. Traditional derivations of superposition center around the longitudinal wakefield function W_z, defined as:

$$W_z(s) = \frac{1}{LQ}\int_{0}^{L} \mathrm{d}z\ E_z(z, \frac{z+s}{c}), \tag{4.11}$$

where s represents the distance of the test particle behind the driving charge Q. We will take a slightly different approach in that we are interested in the longitudinal electric field itself, E_z. The difference between the two is that the wakefield function W_z gives the integrated voltage gain per unit charge and unit length of the entire structure of length L, whereas the electric field E_z gives the instantaneous voltage per unit length.

We begin by noting that for the systems of interest, time and position are related as one would expect, $v_b \mathrm{d}t = \mathrm{d}z$, which is to say that the transverse velocity of the particles is negligible. This relation allows us to switch at liberty quantities that vary in time or position. With this in mind we write the electric field due to a driving charge Q at a distance s behind the driving charge as:

$$E_z(z, s_0, t_0) = \frac{1}{Q}\int_{-\infty}^{z} \mathrm{d}s'\ E_z(z - s' - s_0, \frac{z}{v_b} - t_0)Q\delta(s' - z), \tag{4.12}$$

where t_0 and s_0 are arbitrary phase factors which allow us to pick an origin of our choosing. For example, selecting as our origin a Galilean frame which moves with the driving particle Q, E_z can be written as a function of s only. The E_z under the integral is the single particle longitudinal electric field response of the device, for example the field in a radio frequency cavity or due to a plasma wave.

The above relation for the electric field behind a driving particle of charge Q can be expanded to N number of charges Q as:

$$E_z(z, s_i) = \frac{1}{Q} \int_{-\infty}^{z} \mathrm{d}s' \; E_z(z - s' - s_0, \frac{z}{v_b} - t_0) Q \sum_{i=1}^{N} \delta(s' - s_i). \tag{4.13}$$

At this point it behooves us to rewrite this sum over all N discrete charges Q to obtain an integral relation for the electric field due to a *distribution* of particles. This is done so as to avoid subjecting ourselves to the tedium of keeping track of N equations. To do this we write the sum of delta functions as [54]:

$$N(s) = \sum_{i=1}^{N} \delta(s - s_i) \equiv f(s) + \delta N(s) \tag{4.14}$$

where $f(s)$ is a smooth function defined as the ensemble average of $N(s)$ and $\delta N(s)$ represents the spiky nature of our true discrete distribution,

$$\langle N(s) = f(s) + \delta N(s) \rangle \rightarrow \langle N(s) \rangle \equiv f(s), \tag{4.15}$$

with $\langle\rangle$ representing the ensemble average. For such a system it is natural to assume that the resulting electric field will also be composed of a smooth part and a discrete noisy component, $E_z = E_z(z) + \delta E_z(z)$.

With these definitions in hand it is now possible to write the electric field of a sum of discrete particles as:

$$E_z(z) + \delta E_z(z) = \int_{-\infty}^{z} \mathrm{d}s' \; \{E_z(z - s', 0) + \delta E_z(z - s', 0)\}\{f(s') + \delta N(s')\}, \tag{4.16}$$

where we have chosen our origin to follow the particle at the center of our discrete set such that z now represents an absolute position relative to this center particle and the integral takes care of the phase differences of other driving particles. Using Eq. 4.15, it can be seen that the linear cross terms involving either δE_z or δN will vanish when an ensemble average is taken, leaving only the term quadratic in the noisy terms and the smooth functions:

$$E_z(z) = \int_{-\infty}^{z} \mathrm{d}s' \left(E_z(z - s', 0) f(s') + \langle \delta E(z - s') \delta N(s') \rangle \right). \tag{4.17}$$

Since the relative fluctuations of the mean in the noisy function δN are proportional to $N^{-1/2}$ and the fluctuations of the electric field δE are proportional, through Poisson's equation, to $N^{-1/2}$, the second term on the right hand side of Eq. 4.17 vanishes as $N \to \infty$. As such, for large systems of particles the term quadratic in fluctuations can be ignored. In the end we are left with the field of a bunch of particles being equal to the convolution of the single particle field with the distribution of the bunch,

$$E_z(z) = \int_{-\infty}^{z} \mathrm{d}s' \; E_z(z - s') \; f(s'). \tag{4.18}$$

4.4 Transformer Ratio

The peak transformer ratio, R, is defined as the absolute value of the ratio of the max gradient seen by a witness beam to the max gradient seen by a drive beam,

$$R = \frac{E_{w,gain}}{E_{d,loss}} = \frac{E_+}{E_-}. \tag{4.19}$$

For the purposes of this text we will also be interested in the average transformer ratio, that is to say the average gradient of the witness compared to the average gradient of the drive beam. The average transformer ratio takes into account any possible effects due to beam shape and is much more easily measured than the peak transformer ratio. Further distinctions are made between the unloaded

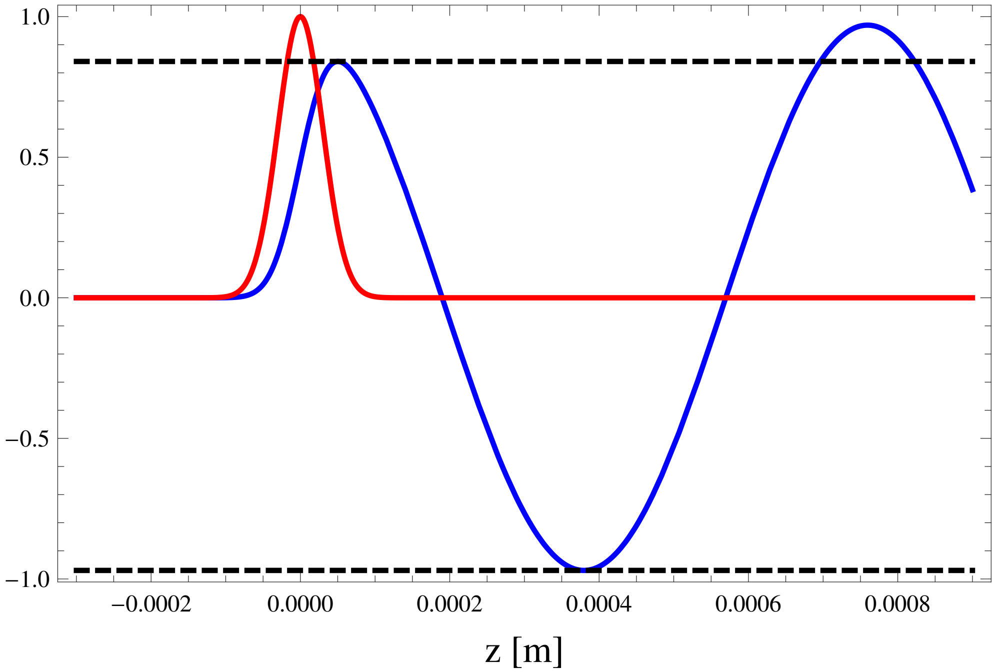

Figure 4.2: An example of an unloaded peak transformer ratio calculation. Red is the normalized beam profile, blue the normalized single mode structure response. For this example we have used a Gaussian beam of r.m.s beam size σ_z = 30 μm and a k_z of 8300 m^{-1}, the same as the parameters of the experiments performed in this work. The peak decelerating field is found to be $E_+ = 0.97$ and $E_- = 0.85$, resulting in R = 1.155.

transformer ratio and the loaded transformer ratio, the later of which contains effects due to the witness beam, the former does not. We are interested in systems with high transformer ratios [75], and how to ensure such high transformer ratios. We strive to be clear about which one we refer to as much as possible.

As an initial example we start with Equation 4.18 where $f(s')$ is a Gaussian distribution and $E_z(z-s')$ is equal to $E_0 cos\big(k_z(z-s')\big)$ for a single mode structure.

$$E_{z,wake} = \int_{-\infty}^{z} E_0 cos\big(k_z(z-s')\big)\frac{e^{-\frac{s'^2}{2\sigma_z^2}}}{\sqrt{2\pi}\sigma_z}\mathrm{d}s', \tag{4.20}$$

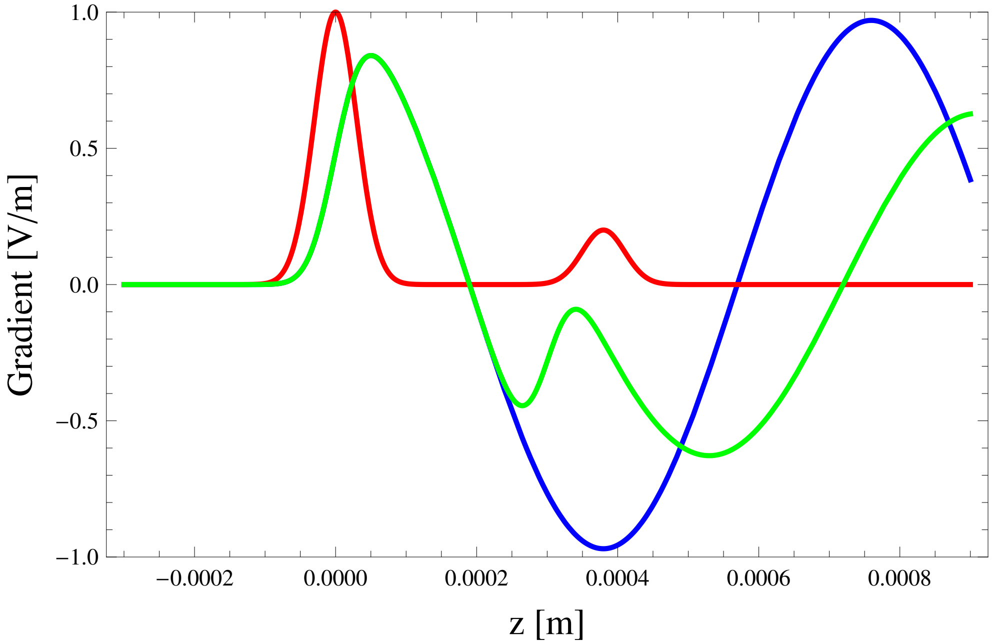

Figure 4.3: An example of a loaded peak transformer ratio calculation. Red is the normalized beam profile, blue the normalized single mode structure response of the drive beam only and green the structure response to both beams. For this example we have used a Gaussian beams of r.m.s beam size $\sigma_z = 30\ \mu m$ and a k_z of 8300 m^{-1}, the same as the parameters of the experiments performed in this work. For this example the average transformer ratio is $R_{avg} = 0.1$.

which when integrated gives:

$$E_{z,wake} = \frac{E_0}{4} e^{-\frac{1}{2}\mathrm{kz}\left(2iz+\mathrm{kz}\sigma_z^2\right)} \left\{ 1 + \mathrm{Erf}\left[\frac{z - i\mathrm{kz}\sigma_z^2}{\sqrt{2}\sigma_z}\right] + e^{2i\mathrm{kz}z}\left(1 + \mathrm{Erf}\left[\frac{z + i\mathrm{kz}\sigma_z^2}{\sqrt{2}\sigma_z}\right]\right) \right\}. \tag{4.21}$$

If the above equation is extremized the peak transformer ratio is found to be, R = 1.155, well in line with the requirement that for symmetric bunches the transformer ratio can be shown to be no greater than R = 2 [76, 77]. When Eq.

4.21 is evaluated in the limit that $\sigma_z \to 0$ and $z = 0$ then

$$E_{z,wake} \to \frac{E_0}{2}. \tag{4.22}$$

This is exactly what one would expect for a single particle (delta function) [31] and results in an unloaded, peak transformer ratio of R=2. Evidently the symmetric function which maximizes the transformer ratio is a delta function.

If we now include the witness beam as well as the drive beam, the result is shown in Figure 4.3, where we have used

$$E_{z,wake} = \int_{-\infty}^{z} E_0 cos\big(k_z(z - s')\big)\Bigg\{\frac{e^{-\frac{s'^2}{2\sigma_z^2}}}{\sqrt{2\pi}\sigma_z} + \frac{1}{5}\frac{e^{-\frac{(s'-s_0)^2}{2\sigma_z^2}}}{\sqrt{2\pi}\sigma_z}\Bigg\}. \tag{4.23}$$

The expression for the resulting field is a bit too cumbersome to write out, or interpret as written, so we will be satisfied with numerical calculation of the average transformer ratio resulting in R =0.1.

Such abysmal transformer ratios can be improved upon if we consider distributions which are not symmetric. We can further improve the situation if we consider witness beams with peak currents that are much lower than the drive beams. We consider next the case of a non-symmetric beam, a triangular or "ramped" beam profile,

$$f(s) = \frac{2}{N^2\lambda^2} s\Theta(s)\Theta(N\lambda - s), \tag{4.24}$$

where $N\lambda$ is the length of the ramp in wavelengths and $\Theta(s)$ the Heaviside Step function. Performing the necessary integrals leads to a peak unloaded transformer ratio

$$R = \frac{2\pi N sin(k_z z)}{1 - cos(k_z z)} = \pi N, \tag{4.25}$$

that is proportional to the length of the beam. An example of a drive-witness set up using a ramped beam can be found in Figure 4.4.

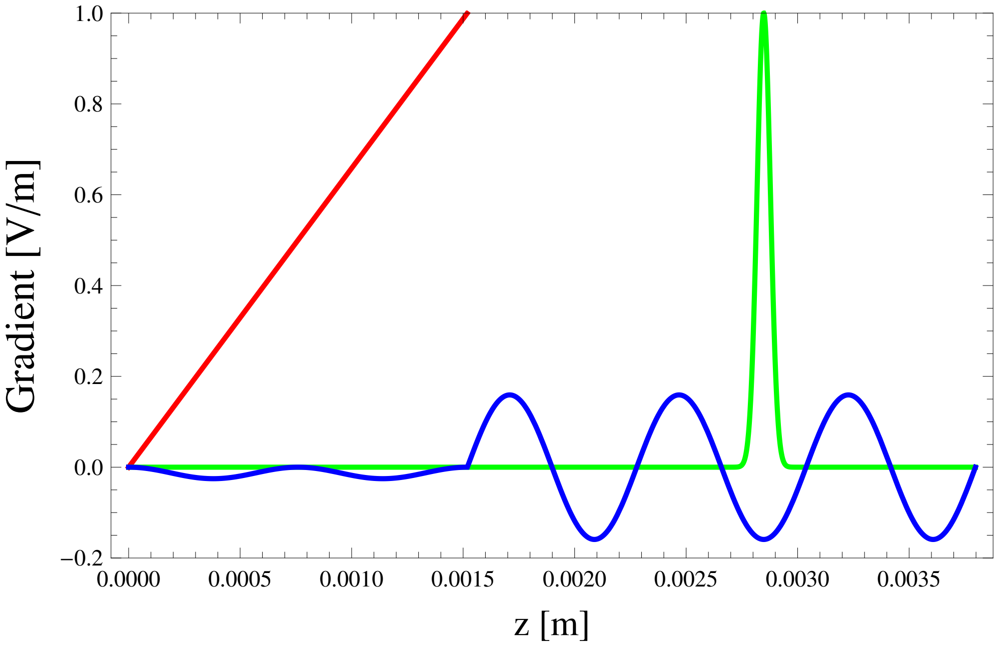

Figure 4.4: An example of using a ramped beam to drive a wake in a single mode structure with a drive bunch length of L = 2λ. The drive beam is shown in red, the witness in green and the resulting wake in blue. In this case the ramped beam is two periods long resulting in an unloaded peak transformer ratio of R = 2π. The witness beam is a gaussian beam of r.m.s. length $\sigma_z = 30\mu m$ and a total charge which is 1% that of the drive beam. For this configuration the average transformer ratio is $R_{avg} = 4.76$

When comparing Figure 4.3 and 4.4 bear in mind that while the drive bunches have the same total charge the witness beams do not. This was the point of the exercise, in order to improve the effective transformer ratio of a drive-witness setup you need a shaped drive bunch and a relatively low charge (or low current) witness bunch. Furthermore, it is worth noting that the ratio of the peak currents of the drive bunches is ten-to-one times greater in the Gaussian shaped beam example, due to the same charge contained in a much shorter beam. This density difference results in a ratio for the peak unloaded accelerating gradients of $E_{ramp}/E_{Gauss} = 0.16$. If your accelerating system is charge constrained you can improve the transformer ratio of your wakefield accelerator, and thus the efficiency, but at the cost of needing a longer drive-witness interaction to get the same final energy exchange.

A further complication of the above systems is the nonuniform gradient throughout the bunches. This means a sustained interaction will effect the bunch energy spread and the bunch shape via dispersive elements [6, 78]. As such we are interested in a bunch profile which results in uniform decelerating field in the drive bunch, thus changing the bunch average energy but not the inter-particle energy.

To find a suitable beam distribution function we can rewrite Equation 4.18, making use of the convolution theorem for the Laplace transform, as,

$$\hat{f}(s) = \frac{\mathcal{L}\{E_w(z)\}}{\mathcal{L}\{E_z(z)\}}, \tag{4.26}$$

where $\mathcal{L}\{\}$ represents the Laplace transform and $E_w = E_{z,wake}$. If we had our druthers we would first insist that the gradient in a drive bunch of length L be constant,

$$E_w(z) = E_0\big(\Theta(z) - \Theta(z-L)\big), \tag{4.27}$$

$$\hat{E}_w(s) = \frac{E_0}{s}(1 - e^{-sL}), \tag{4.28}$$

$$\hat{E}_z(s) = \frac{sE_0}{s^2 + k^2} \tag{4.29}$$

so that the required beam distribution function is,

$$f(z) = \frac{1}{2\pi i}\int_{\gamma - i\infty}^{\gamma + i\infty} \frac{(1 - e^{-sL})}{s^2}(s^2 + k^2)e^{sz}\mathrm{d}s = k^2 L. \tag{4.30}$$

This is just a ramped beam (inside the beam $L \to z$) so that we arrive at $R = \pi N$ again, where N is L/λ. In some sense it is remarkable this guess even produced a distribution which makes any sense. By requiring the decelerating wake be

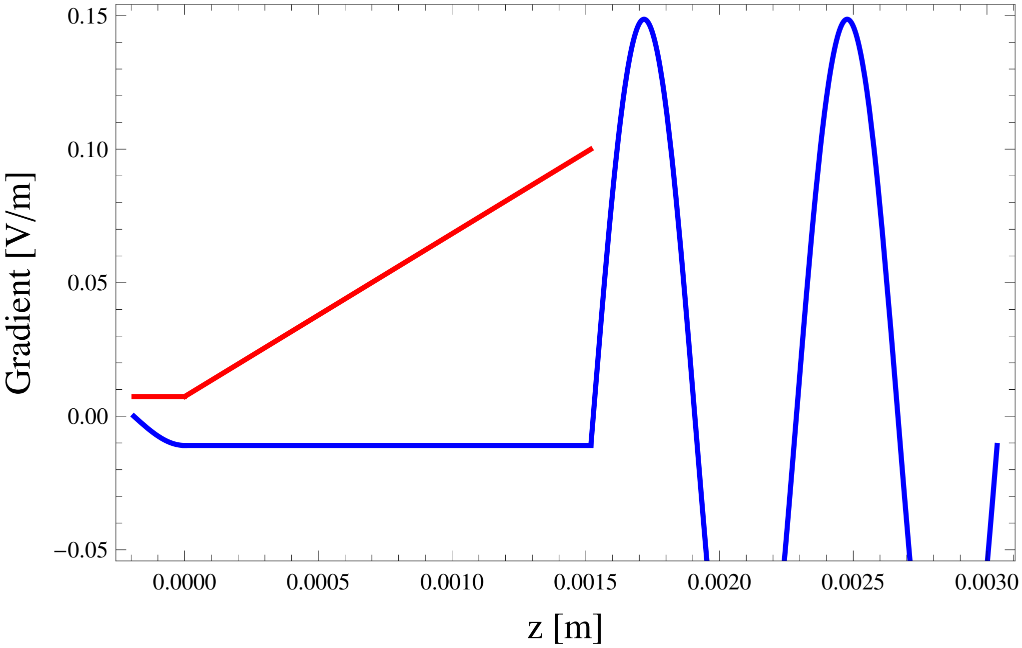

Figure 4.5: The response of a single mode system to a doorstop beam distribution. The red represents the beam distribution and blue the system response.

constant we are demanding that $E_w(z=0)=E_0$ when by definition it should be zero.

If we instead insist [79] that $E_w(z)=E_0(1-e^{-\alpha z})$,

$$\hat{E}_w(s)=\frac{\alpha}{s^2+s\alpha}, \tag{4.31}$$

$$f(z)=\frac{-k^2+k^2 z\alpha}{\alpha}+\frac{e^{-z\alpha}\left(k^2+\alpha^2\right)}{\alpha} \tag{4.32}$$

the transformer ratio is seen to be $R=2\pi N$ when $\alpha\to\infty$, a twofold increase over the simple ramped beam case. This distribution turns out to resemble a ramped beam with a delta function on its nose and is awfully difficult to produce in practice. For practical purposes the beam most often used is the "doorstop"

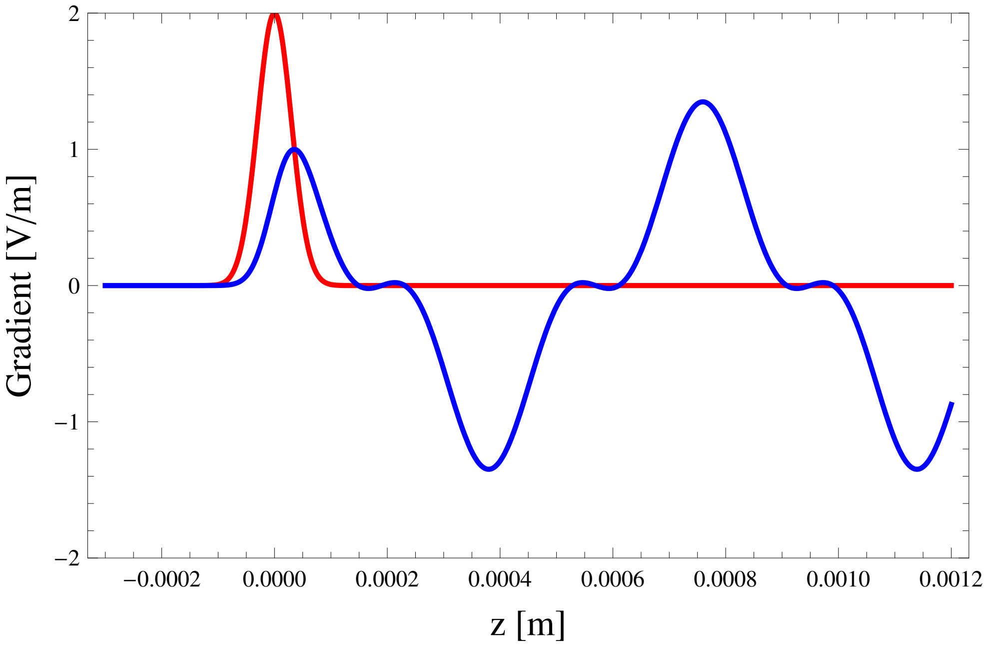

Figure 4.6: The wake excited by a Gaussian beam in a two mode structure. The exciting beam shown in red is the same as that used in previous figure with r.m.s. size $\sigma = 30\ \mu m$, the wake is again shown in blue. For this example the ratio of the fundamental to the secondary mode is A/B = 2 and the secondary wavenumber $k_2 = 3 * k1$. The unloaded peak transformer ratio for this system is R = 1.35.

distribution,

$$f(z) = \frac{2}{L(2+kL)}\left\{\Theta(z)\Theta(L+\frac{\pi}{2k}-z)+k(z-\frac{\pi}{2k})\Theta(z-\frac{\pi}{2k})\Theta(L+\frac{\pi}{2k}-z)\right\}, \tag{4.33}$$

a uniform distribution for a quarter period followed by a ramp, see Figure 4.5. Such a distribution has an unloaded transformer ratio which approaches $R \sim 2\pi N$, the theoretical value for the ideal distribution, and is relatively straightforward to produce *in situ*.

Finally we examine the case for a Gaussian beam in a multimode system for which,

$$E_{z,wake}(z) = E_0 \int_{-\infty}^{z} f(s)\Big(A\cos\big(k_1(z-s)\big) + B\cos\big(k_1(z-s)\big)\Big)\mathrm{d}s. \qquad (4.34)$$

A and B are the ratio constants for the excitation of the different modes, with wave numbers k_1 and k_2. An analytic solution for the transformer ratio of this system is too long to write down, so we are content in showing that the multimode nature of the system can improve the transformer ratio through example, Figure 4.6. For this example the unloaded transformer ratio improves from R = 1.155 to R = 1.35. Such improvements will be important later when we discuss the results of the experiments outlined later in this work.

CHAPTER 5

Dielectric Structures as Accelerators

In preparation for the experiment described in future sections, we wish to construct a theoretical model which describes the problem at hand. Specifically, we wish to solve Maxwell's Equations for an annularly symmetric dielectric lined waveguide that has modes which can couple to a relativistic particle beam. We begin by solving Maxwell's equations for a waveguide containing a linear dielectric material, an example of which is shown in Figure 5.1. We then move on to a derivation of the various parameters observed in experiment, such as the beam-structure coupling parameters.

Due to the scope of the problem at hand it is necessary to focus on solutions less general than possible. As such, we desire only solutions to Maxwell's Equations for which the phase velocity of the waves in the vacuum channel of the waveguide are equal to the velocity of the particles exciting the wave, $v_\phi = \beta c$. Since the beam-stucture coupling is mediated by the longitudinal electric field, E_z, the Transverse Electric modes (TE_{mn}) are ignored, leaving the Transverse Magnetic (TM_{mn}) and Hybrid Electromegnetic (HEM_{mn}) modes. Furthermore, due to the boundary conditions at work in the problem, as outlined below, it is seen that the TM modes are only allowed when $m = 0$ [80, 81, 82, 83].

When the solutions for a particular waveguide are known we can then derive expressions, usually integral relations, which describe the beam-structure interaction. We intend to calculate the relevant measurable parameters examined in

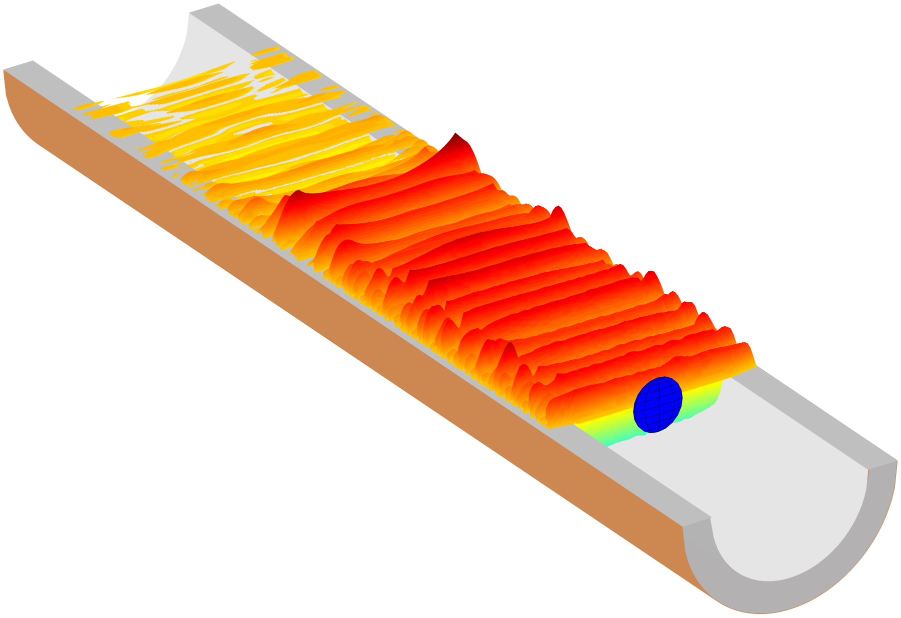

Figure 5.1: A cartoon representation of the experiment performed in this thesis. The top part of the dielectric, shown in grey, has been cut away. The dielectric is coated with a copper cladding to define and contain the mode, shown in orange. The beam is represented as an ellipsoid in blue. As the particle beam traverses the structure is couples to the longitudinal electric field of the modes supported in the structure and gives up energy to those modes, shown here is the wakefield E_z as calculated using VORPAL for an on axis beam.

the experiment described in later sections of this work. As the expressions for the parameters can be complicated relations of non-elementary functions and the resulting functions, if they exist and can be written down, are often not elucidating, we confine ourselves to numerical calculation where necessary.

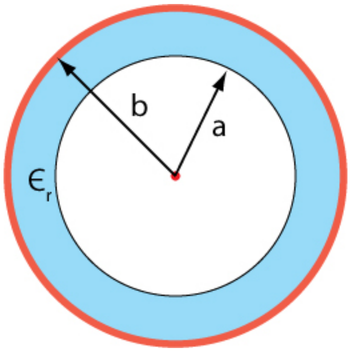

Figure 5.2: A drawing of the boundaries used to solve Maxwell's Equations for a dielectric lined waveguide. The dielectric capillary has an inner radius of a and an outer radius of b, the annulus of which is filled with a dielectric of relative permittivity ϵ_r. The outer shell, at $\rho = b$, is coated with a metal (mostly copper) and is assumed to be a perfect conductor for the purposes of this work.

5.1 An outline of the problem

The solution to the problem at hand necessitates solving Maxwell's Equations for the system presented in Figure 5.2. As the symmetry of the problem suggests, cylindrical coordinates are to be used. As such we begin be writing down the sourceless Maxwell's equations,

$$\vec{\nabla} \times \vec{E} = i\omega\vec{B} \qquad \nabla \cdot \vec{E} = 0 \tag{5.1}$$

$$\vec{\nabla} \times \vec{B} = -i\mu\epsilon\omega\vec{E} \quad \nabla \cdot \vec{B} = 0 \tag{5.2}$$

where a harmonic $e^{-i\omega t}$ time dependence has been assumed. Combining the above equations using the usual relations for solving for the wave equation one arrives at:

$$\begin{aligned} \left(\nabla^2 + \mu\epsilon\omega^2\right)\vec{E} = 0 \\ \left(\nabla^2 + \mu\epsilon\omega^2\right)\vec{B} = 0. \end{aligned} \tag{5.3}$$

As we are interested in solution which propagate with the particle beam down the waveguide we write the solution in the $\hat{z}$ direction as $e^{ik_z z}$, leaving

$$\begin{aligned} \big(\nabla_\perp^2 + \mu\epsilon\omega^2 - k_z^2\big)\vec{E} = 0 \\ \big(\nabla_\perp^2 + \mu\epsilon\omega^2 - k_z^2\big)\vec{B} = 0, \end{aligned} \tag{5.4}$$

where $\nabla_\perp^2$ represents the Laplacian operator in the transverse directions. This Laplacian can be written for cylindrical coordinates as

$$\nabla_\perp^2 \Phi = \frac{1}{\rho}\frac{\partial}{\partial\rho}\left(\rho\frac{\partial\Phi}{\partial\rho}\right) + \frac{1}{\rho^2}\frac{\partial^2\Phi}{\partial\theta^2}. \tag{5.5}$$

If a separation of variables is performed, assuming the coordinates are unrelated and taking into account the assumptions previously made we arrive at,

$$\begin{aligned} \frac{\partial^2 Q(\theta)}{\partial\theta^2} + m^2 Q(\theta) = 0 \\ \frac{\partial^2 R(\rho)}{\partial\rho^2} + \frac{1}{\rho}\frac{\partial R(\rho)}{\partial\rho} + (k_\perp^2 - \frac{m^2}{\rho^2})R(\rho) = 0, \end{aligned} \tag{5.6}$$

where $k_\perp^2 \equiv \mu\epsilon\omega^2 - k_z^2$. It is important to note that $k_\perp^2$ depends on the permittivity and permeability of the material under examination. That is to say that as we have two different materials, vacuum and dielectric, we need two different $k_\perp^2$.

In the vacuum region we demand that the phase velocity of the wave be equal to the phase velocity of the beam, $k_z = \frac{\omega}{v_\phi} = \frac{\omega}{\beta c}$, and thus the transverse wavenumber is imaginary and is written as $k_\perp \to ik$. The tranverse wavenumber in the the dielectric, $k_\perp \to \kappa$, is left as a free parameter:

$$\begin{aligned} -k^2 &= \frac{\omega^2}{c^2} - k_z^2 \qquad \text{in vacuum channel} \\ \kappa^2 &= \mu\epsilon\omega^2 - k_z^2 \quad \text{in dielectric} \end{aligned} \tag{5.7}$$

With this change of $k_\perp$ from real to imaginary the solutions in the vacuum channel transform into modified Bessel functions I_m and K_m. The two equations can be combined, along with the definition of $k_z = \frac{\omega}{\beta c}$, to arrive at

$$\begin{aligned} k &= \frac{\kappa}{\gamma\sqrt{\epsilon_r\beta^2 - 1}} \\ \omega &= \frac{\beta c\kappa}{\sqrt{\epsilon_r\beta^2 - 1}}, \end{aligned} \tag{5.8}$$

where ϵ_r is the dielectric coefficient of the material used to line the waveguide wall.

The solution to the first equation in 5.6 is $Q(\theta) = e^{-im\theta}$, where m must be in integer if the field is to be single valued when the entire azimuth is used.

Finally what remains is to solve for $R(\rho)$ using the geometry of the problem at hand. We start with the usual ansatz:

$$R_m(\rho) = \begin{cases} AI_m(k\rho) + BK_m(k\rho) & \text{if } \rho \leq a \\ CJ_m(\kappa\rho) + DN_m(\kappa\rho) & \text{if } a \leq \rho \leq b, \end{cases} \tag{5.9}$$

where immediately we write $B = 0$ as K_m is not physical as $\rho \to 0$, and follow the usual process of manually satisfying the boundary conditions.

Before proceeding with the satisfaction of the boundary conditions we note that it is possible to write four of the six field components in terms of the remaining two [14]. In this case we elect (as is customary) to solve for $\vec{E_z}$ and $\vec{B_z}$, noting that the other components of the field can then be found using the relations:

$$\begin{aligned} \vec{E_t} &= \frac{i}{k_\perp^2}\left[k_z\vec{\nabla}_\perp E_z - \omega\hat{z}\times\vec{\nabla}_\perp B_z\right] \\ \vec{B_t} &= \frac{i}{k_\perp^2}\left[k_z\vec{\nabla}_\perp B_z + \mu\epsilon\omega\hat{z}\times\vec{\nabla}_\perp E_z\right]. \end{aligned} \tag{5.10}$$

This splits the solutions to the waves in the dielectric lined waveguide into three distinct groups: Transverse Electric modes TE_{mn} for which $E_z = 0$, Transverse Magnetic modes TM_{mn} for which $B_z = 0$ and Hybrid Electromagnetic modes HEM_{mn} which allow E_z & $B_z \neq 0$ simultaneously.

As a final remark prior to beginning specific solutions, we point out that it can be shown [14, 17] that,

$$\left.\frac{\partial B_z}{\partial n}\right|_S = \left.E_z\right|_S = 0, \tag{5.11}$$

are both necessary and sufficient conditions for satisfaction of all the boundary conditions at a dielectric-perfect conductor interface, where S represents evaluation at the interface.

5.2 The Transverse Magnetic TM_{0n} modes

For the case in which $m = 0$ Eqs. 5.10 can be seen to separate into two different categories. These are the aforementioned Transverse Magnetic and Transverse Electric modes. As we are interested only in modes which the beam can couple to via the longitudinal electric field, E_z, we concern ourselves with the TM_{0n} modes, for which $B_z = 0$.

Examining Eqs. 5.10 for the case in which $B_z = m = 0$ we see that the only two transverse field components which exist are E_r and B_θ which are given by the relations:

$$\begin{aligned} E_\rho &= \frac{ik_z}{k_\perp^2}\frac{\partial E_z}{\partial \rho} \\ B_\theta &= \frac{i\mu\epsilon\omega}{k_\perp^2}\frac{\partial E_z}{\partial \rho} \\ \frac{E_\rho}{B_\theta} &= \frac{c}{\epsilon_r \beta_{beam}}. \end{aligned} \tag{5.12}$$

The relation between the two has been explicitly included to indicate that there remains only one boundary condition to solve for in addition to those required of E_z. While a more general solution can written which provides the TM_{0n} solutions under the right circumstances the author finds it illuminating to start with a simpler system. The more general case can be found in the section on HEM_{mn} modes. We continue by writing out E_z and E_ρ for the case in which $B_z = m = 0$, using Eq. 5.9,

$$\begin{aligned} E_z &= R_0(\rho)e^{-i(k_z z+\omega t)} \\ E_\rho &= \frac{ik_z}{k_\perp^2}\frac{\partial R_0(\rho)}{\partial\rho}e^{-i(k_z z+\omega t)}, \end{aligned} \tag{5.13}$$

and then writing the the system of equations which comprise the relevant boundary conditions,

$$\Delta E_z\bigg|_{\rho=a} = 0 \ , \ \Delta E_z\bigg|_{\rho=b} = 0 \ , \ \Delta D_\rho\bigg|_{\rho=a} = 0. \tag{5.14}$$

The preceding boundary conditions form a set of coupled equations which are then used to solve for the dispersion relation of the system via the determinant. Specifically, as the system of equations can be written as a homogenous set of equations the determinant of the system must be zero if there is to be a non-trivial solution [84],

$$\begin{pmatrix} I_0(ka) & -J_0(\kappa a) & -N_0(\kappa a) \\ 0 & J_0(\kappa b) & N_0(\kappa b) \\ \frac{1}{k}I_0'(ka) & \frac{1}{\kappa}J_0'(\kappa a) & \frac{1}{\kappa}N_0'(\kappa a) \end{pmatrix} \begin{pmatrix} A \\ C \\ D \end{pmatrix} = 0, \tag{5.15}$$

$$\begin{vmatrix} I_0(ka) & -J_0(\kappa a) & -N_0(\kappa a) \\ 0 & J_0(\kappa b) & N_0(\kappa b) \\ \frac{1}{k}I_0'(ka) & \frac{1}{\kappa}J_0'(\kappa a) & \frac{1}{\kappa}N_0'(\kappa a) \end{vmatrix} \equiv 0. \tag{5.16}$$

For the purposes of this section the $()'$ is a derivative with respect to the total argument of the function under examination.

The determinant for the TM_{0n} modes can then be written as

$$\frac{I_1(ka)}{kI_0(ka)} = \frac{\epsilon_r}{\kappa}\frac{N_1(\kappa a)J_0(\kappa b) - J_1(\kappa a)N_0(\kappa b)}{N_0(\kappa a)J_0(\kappa b) - J_0(\kappa a)N_0(\kappa b)}, \tag{5.17}$$

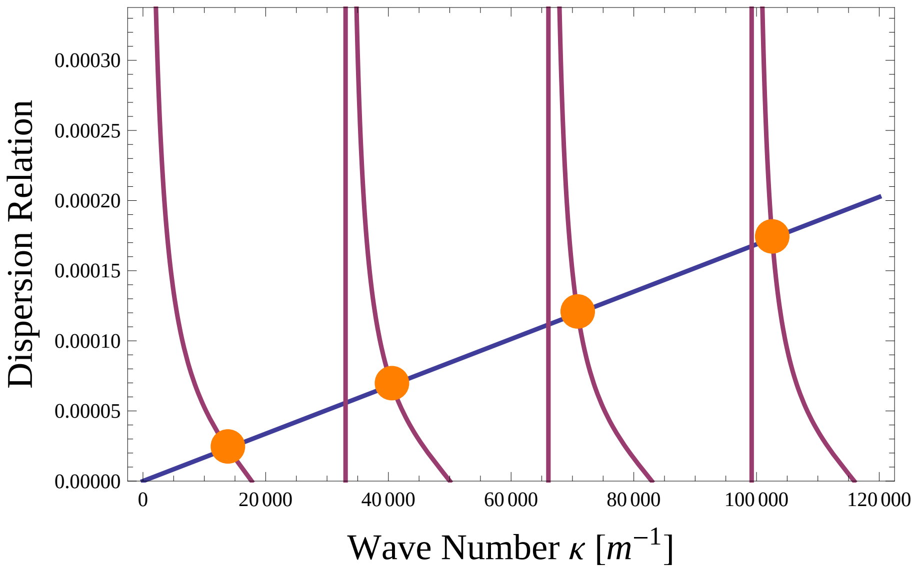

Figure 5.3: A graphical solution to the transcendental equation given in Eq. 5.17. The left-hand side of the equation is shown in blue while the right-hand side is shown in red and the orange dots represent the intercepts between the two and thus the solutions to the dispersion relation. For this plot the inner radius of the structure is $a = 225\ \mu m$ and the outer radius is $b = 320\ \mu m$ while the dielectric constant $\epsilon_r = 3.8$, corresponding to one of the structures used in an experiment described later.

a transcendental equation which is solved to find the discrete solutions κ_{0n} allowed by the system. Solutions to the transcendental equation can be found graphically by plotting the two sides of the above equation, as shown in Figure 5.3, where each orange dot is a solution κ_{0n}.

Before we continue a choice must be made as to which direction the beam travels. As the author likes to integrate from $-\infty$ to ∞, the beam will be assumed to move from right to left. The means that we can now write the explicit functions

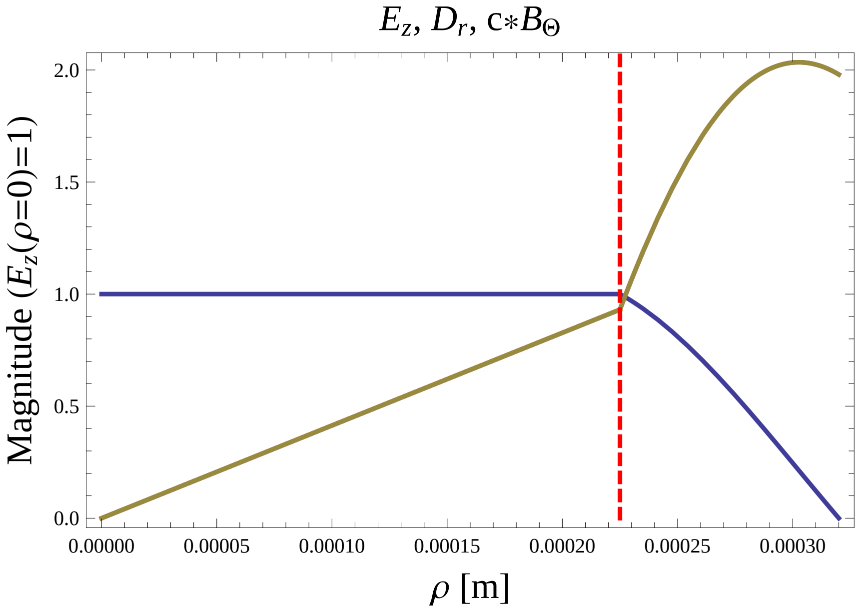

Figure 5.4: The fields present in the structure due to the excitation of the TM_{01} mode, normalized to E_z. Of note is the relative flatness of E_z in the vacuum channel. The parameters used as the sam as with Fig. 5.3, the boundary between the vacuum and the dielectric at $a = 225\mu m$ is marked with a dashed red line. While D_r is shown with a solid red line, cB_θ (in yellow) covers it completely.

which describe E_z as:

$$E_z(\rho) = E_0 e^{-i(k_z z + \omega t)} \begin{cases} I_0(k\rho) & \text{if } \rho \leq a \\ I_0(ka)\frac{N_0(\kappa\rho)J_0(\kappa b) - J_0(\kappa\rho)N_0(\kappa b)}{N_0(\kappa a)J_0(\kappa b) - J_0(\kappa a)N_0(\kappa b)} & \text{if } a \leq \rho \leq b, \end{cases} \tag{5.18}$$

where C and D have been eliminated in favor of A and A has been relabeled E_0, a term which describes the absolute magnitude of the fields in the structure. The subscripts for κ_{0n} and k_{0n} have been suppressed in the above equation. With the values of κ_{0n} which satisfy the dispersion relation for the TM_{0n} modes in hand, we are now free to plot the field distributions as a function of ρ. The reader is reminded that the modes have an m number of 0, so they look the same for any given angle θ around the axis of symmetry $\hat{z}$. Of particular interest to the experiment described later is that the longitudinal electric field for the TM_{0n} modes are only mathematically a function of ρ in the vacuum channel. For the parameters used in this experiment E_z differs by one part in a million from $\rho = 0$ to $\rho = a$. Envoking the Panofsky-Wenzel theorem this means that $\frac{\partial p_z}{\partial \rho} \approx 0$, so any transverse forces which do arise must be free of the longitudinal coordinate z. The fields for the TM_{01} mode are shown in Fig. 5.4.

5.2.1 Beam-Mode Coupling

With the fields in a given TM_{0n} mode described by Eqs. 5.18 and 5.10 it is now possible to solve for the coupling of a specific particle beam distribution to a particular mode, E_0. To do so it is necessary to write a conservation law for energy in the beam-mode system [14],

$$-\int_V \vec{J} \cdot \vec{E}\, \mathrm{d}^3x = \int_V \left[\frac{\partial u}{\partial t} + \vec{\nabla} \cdot \vec{S}\right] \mathrm{d}^3x, \tag{5.19}$$

where J is the beam current, $u = \frac{1}{2}(\vec{E} \cdot \vec{D} + \vec{B} \cdot \vec{H})$ is the energy stored in the field and $\vec{S} = \vec{E} \times \vec{H}$ is the Poynting vector.

We begin by solving for the single particle coupling to the mode and make use of the expressions derived in Section 4.3 to expand to a bunch of particles. As such, the current for a single particle can be written as:

$$\vec{J} = -ev_z\delta(\rho - \rho_0)\frac{\delta(\theta - \theta_0)}{\rho}\delta(z - v_z t)\hat{z}, \tag{5.20}$$

where we are specifically allowing for a particle which is off axis with initial coordinates (ρ_0, θ_0) and the particle is assumed to have a vanishingly small transverse velocity. As the waves excited in the structure travel at the speed of light down the waveguide, by definition, we perform a Galilean change of frame into the beam's frame, $\zeta = z + v_z t$, of Eq. 5.19 and 5.20,

$$\begin{aligned} -\int_V \vec{J} \cdot \vec{E}\, \mathrm{d}^3x &= \int_V \left[(\frac{\partial}{\partial t} + v_z \frac{\partial}{\partial \zeta}) u - \vec{\nabla} \cdot \vec{S} \right] \mathrm{d}^3x \\ \vec{J} &= -e v_z \delta(\rho - \rho_0) \frac{\delta(\theta - \theta_0)}{\rho} \delta(\zeta) \hat{z}. \end{aligned} \tag{5.21}$$

Noting that in the beam frame $u \neq f(t)$, the $\frac{\partial}{\partial t}$ term on the right-hand side of the first of the above equations can be dropped. Making use of the Divergence theorem for the transverse portion of the term involving the Poynting Vector yields:

$$-\int_V \vec{J} \cdot \vec{E}\, \mathrm{d}^3x = \int_V \left[-\frac{\partial S_z}{\partial \zeta} + v_z \frac{\partial u}{\partial \zeta} \right] \mathrm{d}^3x - \int_C \vec{S_\perp} \cdot \hat{n}\, \mathrm{d}^2x_\perp, \tag{5.22}$$

where C represents a contour in the plane of the problem shown in Figure 5.2. If the integral over the contour C is evaluated at a point inside the perfect conductor surrounding the structure the last term in the above equation vanishes. Finally the partial derivative with respect to ζ can be integrated out and we are left with,

$$-\int_V \vec{J} \cdot \vec{E}\, \mathrm{d}^3x = \int_A \left[-S_z + v_z u \right] \mathrm{d}^2x_\perp, \tag{5.23}$$

where A is the surface in the plane perpendicular to the particle motion, at the particle location, $\zeta = 0$.

The integral comprising $\vec{J}$ and $\vec{E}$ is now performed, for which the particle is assumed to be in the vacuum channel,

$$e v_z E_0 I_0(k\rho_0) = -E_0^2 \int_A \left[\frac{S_z - v_z u}{E_0^2} \right] \mathrm{d}^2x_\perp, \tag{5.24}$$

where the constant common E_0 has been removed from all field terms in the Poynting vector S_z and field energy density u. Now solving for E_0 gives the single particle coupling to the TM_{0n} modes as,

$$E_0 = -e v_z I_0(k\rho_0) \frac{1}{\int_A \left[\frac{S_z - v_z u}{E_0^2} \right] \mathrm{d}^2x_\perp}. \tag{5.25}$$

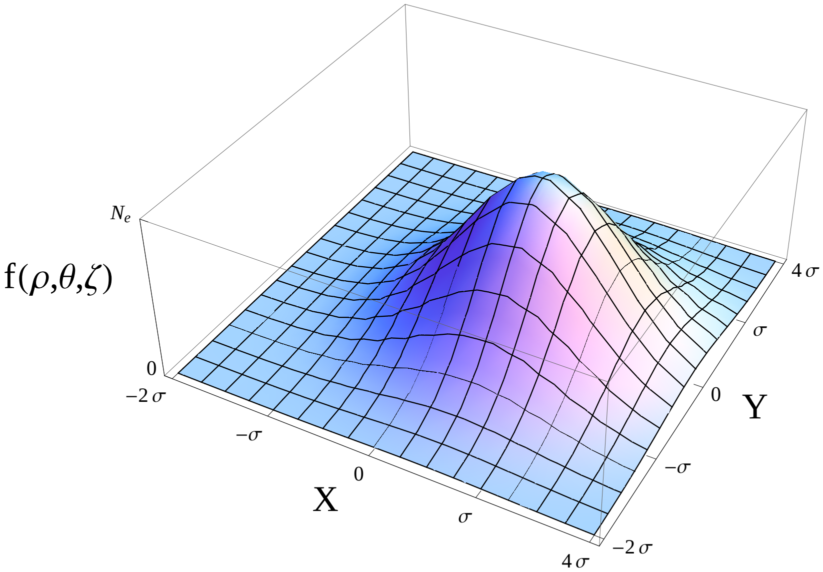

Figure 5.5: An example of a beam distribution where the beam is offset along the $\hat{x}$-axis by $\frac{\sigma}{2}$.

It is noted that this expression conforms to that derived in Reference [85] where objections were made concerning the definition of a group velocity for the modes in the structures used in this work. Contrary to said objections if we assume arguendo that such a definition for the group velocity exists and is defined as is usually so for waveguides [14, 17, 84, 86], the resulting expression for E_0 returns the same coupling parameter as in Equation 5.25.

To calculate the wakefield due to an electron beam it is necessary to use the beam's distribution function such as

$$f(\rho,\theta,\zeta) = \frac{N_e}{\sqrt{2\pi}\sigma_z} e^{-\frac{\zeta^2}{2\sigma_z^2}} * \frac{1}{2\pi\sigma_\rho^2} e^{\frac{-\rho^2+2\rho\rho_{off}Cos(\theta)-\rho_{off}^2}{2\sigma_\rho^2}}, \tag{5.26}$$

where an offset along the x-axis of magnitude ρ_{off} has been assumed, see Figure 5.5. Next we use Equation 5.25 to calculate the single particle-mode coupling parameter and perform the superposition integral of all N_e particles in the distribution which gives (as in Section 4.3),

$$E_z = E_0 N_e \int_{-\infty}^{z} \mathrm{d}s e^{-ik_z(z-s)} \frac{1}{\sqrt{2\pi}\sigma_z} e^{-\frac{s^2}{2\sigma_z^2}} \int_0^a \int_0^{2\pi} \rho \mathrm{d}\rho \mathrm{d}\theta \frac{I_0(k\rho)}{2\pi\sigma_\rho^2} e^{\frac{-\rho^2+2\rho\rho_{off}Cos(\theta)-\rho_{off}^2}{2\sigma_\rho^2}}. \tag{5.27}$$

Performing the integral over θ gives,

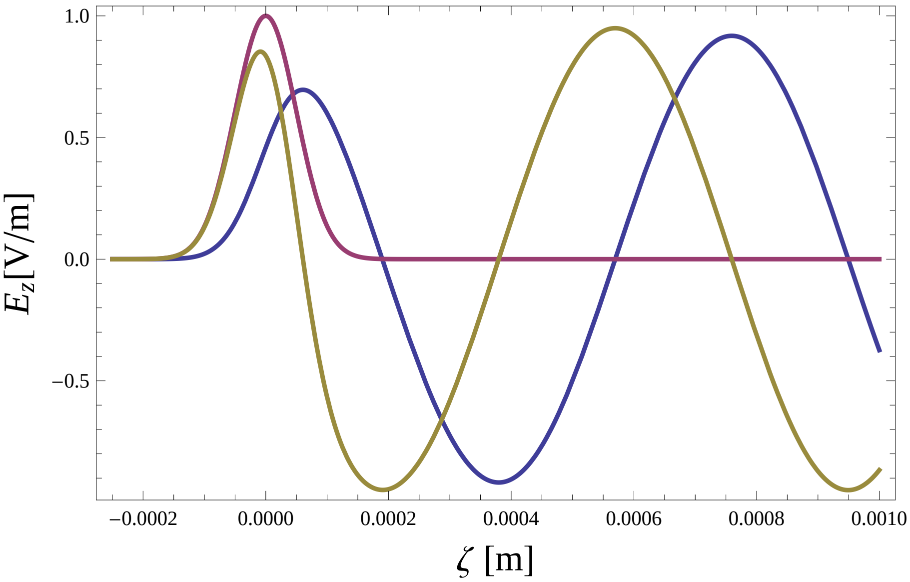

Figure 5.6: The response of a single mode structure to a gaussian bunch (in red) of finite length. The total structure response E_z is shown in blue, while the first derivative is shown in yellow. For this plot the r.m.s bunch length of the beam was 50 μm and the dimensions for the structure were $a = 225$ μm and $b = 320$ μm. The magnitude of the beam current and the derivative of the longitudinal electric field E_z have been scaled and are representative of their structure only.

$$E_z = E_0 N_e \int_{-\infty}^{z} \mathrm{d}s e^{-ik_z(z-s)} \frac{1}{\sqrt{2\pi}\sigma_z} e^{-\frac{s^2}{2\sigma_z^2}} \int_0^a \rho \mathrm{d}\rho \frac{I_0(k\rho)}{\sigma_\rho^2} e^{\frac{-\rho^2-\rho_{off}^2}{2*\sigma_\rho^2}} I_0(\frac{\rho_{off}\rho}{\sigma_\rho^2}). \tag{5.28}$$

If the beam size is assumed to be much smaller than the radius of the structure, $\sigma_\rho \ll a$, then the ρ integral can be integrated analytically (from 0 to ∞) [45] to give

$$E_z = E_0 N_e \int_{-\infty}^{z} \mathrm{d}s e^{-ik_z(z-s)} \frac{1}{\sqrt{2\pi}\sigma_z} e^{-\frac{s^2}{2\sigma_z^2}} \underline{e^{\frac{k^2\sigma_\rho^2}{2}} I_0(k\rho_{off})}, \tag{5.29}$$

If it is further assumed that the offset ρ_{off} is on the order of an r.m.s. beam size σ_ρ the underlined component in the above equation reduces to unity, leaving us with,

$$E_z = E_0 N_e \int_{-\infty}^{z} \mathrm{d}s e^{-ik_z(z-s)} \frac{1}{\sqrt{2\pi}\sigma_z} e^{-\frac{s^2}{2\sigma_z^2}}. \tag{5.30}$$

This result is unsurprising as we may have expected it given the longitudinal electric field E_z is constant across the vacuum gap, q.v. Figure 5.4. For the TM_{0n} modes a particle which is on axis couples equally as well as a particle which is off axis, but still in the vacuum channel. Continuing on with the evaluation of the coupling of a beam to the TM_{on} modes, Eq. 5.27, we evaluate the most recent integral and find,

$$E_z(z) = \frac{E_0 N_e}{2} e^{-ik_z z} e^{-\frac{k_z^2\sigma_z^2}{2}} \left[1 + \mathrm{Erf}\left(\frac{z}{\sqrt{2}\sigma_z} - \frac{ik_z\sigma_z}{\sqrt{2}}\right)\right]. \tag{5.31}$$

The above integral evaluated in the case that $z \gg \sigma_z$ returns $E_z \simeq E_0 N_e$, that is to say that the maximum field behind the bunch is simply the single particle field times the number of particles.

5.3 The Hybrid Electromagnetic HEM_{mn} modes

We now concern ourselves with the modes present in the structure when $m \neq 0$, the so-called Hybrid HEM_{mn} modes. To avoid the confusion possible when using an admixture of complex solutions to solve a separable equation we resort to using real functions except for the wake-like solution describing propagation along the waveguide. This will require and anstaz with 9 unknowns, 8 for the boundary conditions and one for the definition of κ. As in the last section we will leave one coefficient as a free parameter which defines the coupling from particle to mode.

The defining fields E_z and B_z can be written as,

$$E_z(r,\theta,z,t) = e^{-i(k_z z+\omega t)} \begin{cases} I_m(kr)\Big(A\cos(m\theta)+F\sin(m\theta)\Big) & \text{if } r \le a \\ \Big\{CJ_m(\kappa r) - DN_m(\kappa r)\Big\}\cos(m\theta+\phi) & \text{if } a \le r \le b, \end{cases} \tag{5.32}$$

$$B_z(r,\theta,z,t) = e^{-i(k_z z+\omega t)} \begin{cases} I_m(kr)\Big(B\cos(m\theta)+H\sin(m\theta)\Big) & \text{if } r \le a \\ \Big\{QJ_m(\kappa r) - PN_m(\kappa r)\Big\}\cos(m\theta+\psi) & \text{if } a \le r \le b. \end{cases} \tag{5.33}$$

We once again apply the boundary conditions at $\rho = b$,

$$\Delta E_z\Big|_{\rho=b} = 0 \ , \ \Delta\frac{\partial B_z}{\partial\rho}\Big|_{\rho=b} = 0, \tag{5.34}$$

and $\rho = a$

$$\Delta E_z\Big|_{\rho=a} = \Delta\epsilon E_r\Big|_{\rho=a} = \Delta E_\theta\Big|_{\rho=a} = 0 \ , \ \Delta B_z\Big|_{\rho=a} = \Delta B_r\Big|_{\rho=a} = \Delta B_\theta\Big|_{\rho=a} = 0 \tag{5.35}$$

and arrive at the following matrix which defines the dispersion relation

$$\begin{aligned}&\left|\begin{matrix} 0 & -\frac{k_z}{k}T\cos{(m\theta+\phi)}\left(\frac{I'_m(ka)}{I_m(ka)}+\frac{\epsilon_r k}{\kappa}\frac{V}{T}\right) \\ 0 & -\frac{\omega}{kc^2}T\cos{(m\theta+\phi)}\left(\frac{I'_m(ka)}{I_m(ka)}+\frac{\epsilon_r k}{\kappa}\frac{V}{T}\right) \\ -\frac{m\omega}{k^2c^2a}\frac{I_m(ka)}{\sin m\theta} & \frac{m\omega}{k^2c^2a}T\left(\frac{\cos{(m\theta+\phi)}\cos{(m\theta)}}{\sin{(m\theta)}}-\frac{\epsilon_r k^2}{\kappa^2}\sin{(m\theta+\phi)}\right) \\ \frac{mk_z}{k^2a}\frac{I_m(ka)}{\sin m\theta} & -\frac{mk_z}{k^2a}T\left(\frac{\cos{(m\theta+\phi)}\cos{(m\theta)}}{\sin{(m\theta)}}-\frac{k^2}{\kappa^2}\sin{(m\theta+\phi)}\right)\end{matrix}\right. \\ &\left.\begin{matrix}\frac{m\omega}{k^2a}\frac{I_m(ka)}{\sin m\theta} & -\frac{m\omega}{k^2a}W\left(\frac{\cos{(m\theta+\psi)}\cos{(m\theta)}}{\sin{(m\theta)}}-\frac{\epsilon_r k^2}{\kappa^2}\sin{(m\theta+\psi)}\right) \\ \frac{mk_z}{k^2a}\frac{I_m(ka)}{\sin m\theta} & -\frac{mk_z}{k^2a}W\left(\frac{\cos{(m\theta+\psi)}\cos{(m\theta)}}{\sin{(m\theta)}}-\frac{k^2}{\kappa^2}\sin{(m\theta+\psi)}\right) \\ 0 & -\frac{k_z}{k}W\cos{(m\theta+\psi)}\left(\frac{I'_m(ka)}{I_m(ka)}+\frac{k}{\kappa}\frac{U}{W}\right) \\ 0 & \frac{\omega}{k}W\cos{(m\theta+\psi)}\left(\frac{I'_m(ka)}{I_m(ka)}+\frac{k}{\kappa}\frac{U}{W}\right)\end{matrix}\right| = 0.\end{aligned} \tag{5.36}$$

Where

$$\begin{aligned} T(\kappa,m) &= N_m(\kappa a)-\frac{N_m(\kappa b)}{J_m(\kappa b)}J_m(\kappa a) \\ W(\kappa,m) &= N_m(\kappa a)-\frac{N'_m(\kappa b)}{J'_m(\kappa b)}J_m(\kappa a) \\ V(\kappa,m) &= N'_m(\kappa a)-\frac{N_m(\kappa b)}{J_m(\kappa b)}J'_m(\kappa a) \\ U(\kappa,m) &= N'_m(\kappa a)-\frac{N_m(\kappa b)}{J_m(\kappa b)}J'_m(\kappa a).\end{aligned} \tag{5.37}$$

After a prodigious amount of algebra two relations are found. First, in order for the mode numbers κ to not be a function of θ we must have $\phi = \psi \pm \frac{\pi}{2}$. For the remainder of this work we shall take $\phi = \psi + \frac{\pi}{2}$. Second, the dispersion relation is found to reduce to

$$\frac{m^2\gamma^4\beta^2(\epsilon_2-1)^2}{\kappa^4a^2} = \left(\frac{I'_m(ka)}{kI_m(ka)}+\frac{\epsilon_r}{\kappa}\frac{V}{T}\right)\left(\frac{I'_m(ka)}{kI_m(ka)}+\frac{1}{\kappa}\frac{U}{W}\right), \tag{5.38}$$

which agrees with the relation derived through other methods [82, 85]. It is noted that if $m = 0$ the term with $\Gamma_m = \frac{V}{T}$ yields the TM_{0n} modes and the term with

$\Pi_m = \frac{U}{W}$ the TE_{0n} modes. An example plot showing the solutions to the above dispersion relation is shown in Figure 5.7 and the fields are plotted in Figure 5.8.

Finally the equations for the longitudinal fields can be written

$$E_z(\rho,\theta,z,t) = E_0 \cos{(m\theta+\phi)} e^{-i(k_z z+\omega t)} * \\ \begin{cases} I_m(k\rho) & \text{if } \rho \le a \\ \alpha_m \Big\{ J_m(\kappa\rho)N_m(\kappa b) - N_m(\kappa\rho)J_m(\kappa b) \Big\} & \text{if } a \le \rho \le b, \end{cases} \tag{5.39}$$

$$B_z(\rho,\theta,z,t) = -B_0 \sin{(m\theta+\phi)} e^{-i(k_z z+\omega t)} * \\ \begin{cases} I_m(k\rho) & \text{if } \rho \le a \\ \eta_m \Big\{ J_m(\kappa\rho)N'_m(\kappa b) - N_m(\kappa\rho)J'_m(\kappa b) \Big\} & \text{if } a \le \rho \le b, \end{cases} \tag{5.40}$$

with

$$\alpha_m \equiv \frac{I_m(ka)}{J_m(\kappa a)N_m(\kappa b) - J_m(\kappa b)N_m(\kappa a)}, \tag{5.41}$$

$$\eta_m \equiv \frac{I_m(ka)}{J_m(\kappa a)N'_m(\kappa b) - J'_m(\kappa b)N_m(\kappa a)}. \tag{5.42}$$

Once again $()'$, the prime, indicates differentiation with respect to the entire argument. The relationship between E_0 and B_0 can be found by examining the boundary condition for E_θ at $\rho = a$. The E_θ boundary condition at $\rho = a$ gives,

$$\begin{aligned} &\frac{-1}{k^2}\left[\frac{-mk_z}{a}E_0 I_m(ka) + \omega k B_0 I'_m(ka)\right] = \\ &\quad \frac{1}{\kappa^2}\Big\{\frac{-mk_z}{a}E_0\alpha_m[J_m(\kappa a)N_m(\kappa b) - N_m(\kappa a)J_m(\kappa b)] \\ &\quad + \omega\kappa B_0\eta_m[J'_m(\kappa a)N'_m(\kappa b) - N'_m(\kappa a)J'_m(\kappa b)]\Big\}, \end{aligned} \tag{5.43}$$

Which cleans up to

$$\frac{mk_z}{a\omega}\frac{E_0}{B_0}\left(\frac{1}{k^2} + \frac{1}{\kappa^2}\right) = \left\{\frac{I'_m(ka)}{kI_m(ka)} + \frac{\Pi_m}{\kappa}\right\} \tag{5.44}$$

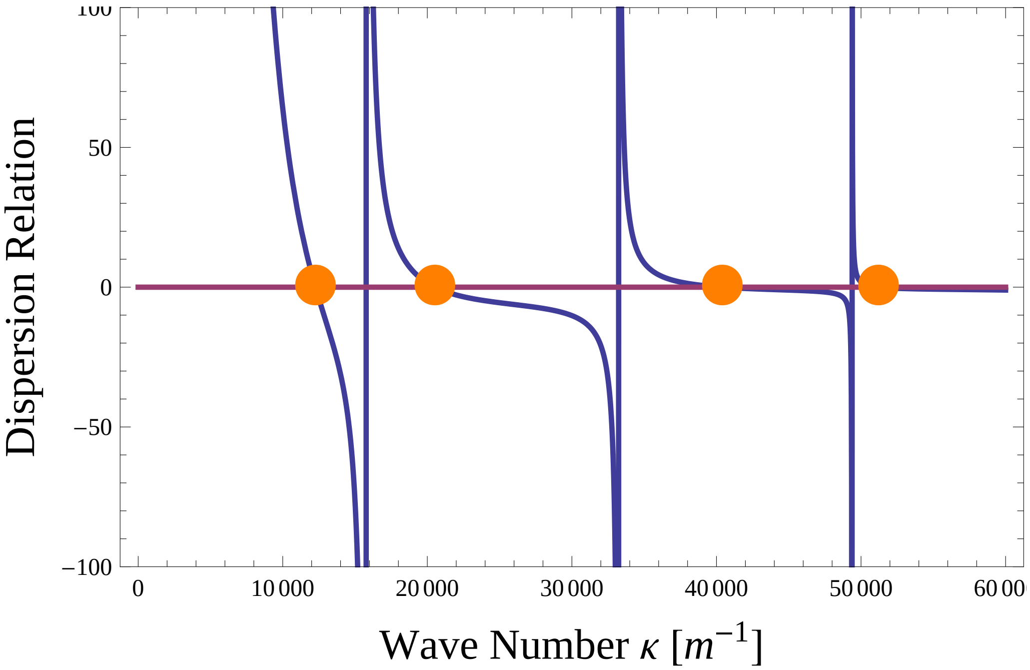

Figure 5.7: A plot of Equation 5.38 and its solutions. The blue line represents the left hand side of the dispersion relation and the red line marks zero. The orange dots are the first four values of κ_{mn} which satisfy the dispersion relation. For this plot a=225 μm, b = 320 μm and ϵ_r=3.8.

with

$$\Gamma_m = \frac{J'_m(\kappa a)N_m(\kappa b) - N'_m(\kappa a)J_m(\kappa b)}{J_m(\kappa a)N_m(\kappa b) - N_m(\kappa a)J_m(\kappa b)} = \frac{V}{T} \tag{5.45}$$

$$\Pi_m = \frac{J'_m(\kappa a)N'_m(\kappa b) - N'_m(\kappa a)J'_m(\kappa b)}{J_m(\kappa a)N'_m(\kappa b) - N_m(\kappa a)J'_m(\kappa b)} = \frac{U}{W}. \tag{5.46}$$

The traverse fields can be derived using the waveguide field relations previous derived in Eq. 5.10.

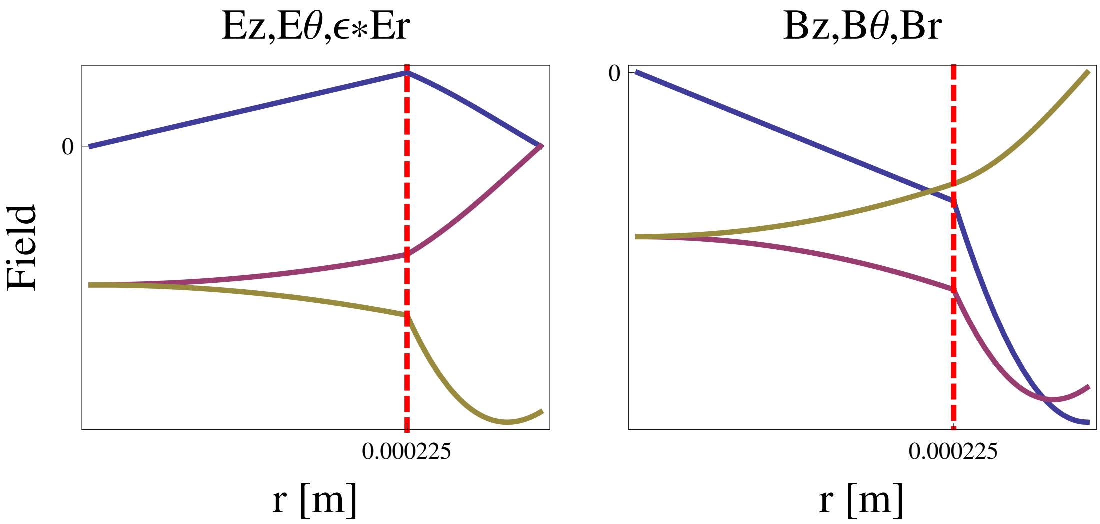

Figure 5.8: Plot of the fields generated in the HEM_{11} mode. The colors correspond to the labels in the order blue, red, yellow. The vertical dashed red line indicates the change from vacuum to dielectric a $\rho = a$, where $\epsilon_r = 3.8$. These are the fields at their maximum, they are not all necessarily in phase.

5.3.1 Beam-HEM_{mn} mode coupling

With the values of κ_{mn} known all that is left is to determine the beam-mode coupling, which can be done using Equation 5.25,

$$E_0(\rho, \theta) = -e v_z \frac{1}{\int_A \left[\frac{S_z - v_z u}{E_0^2} \right] \mathrm{d}^2 x} I_m(k\rho) \cos(m\theta + \phi) = E_c I_m(k\rho) \cos(m\theta + \phi), \tag{5.47}$$

where ρ and θ are the location of the particle coupling to the wake and E_c is the single particle to field coupling coefficient. To obtain the total expected coupling we need to sum over all the particles, including their coupling parameter, resulting in an integral over the distribution function. For example, the longitudinal electric field for the beam distribution used in Equation 5.26 is given by,

$$\begin{aligned} E_z(\rho,\theta,z) =& \cos{(m\theta+\phi)} I_m(k\rho) \int_{-\infty}^{z} \mathrm{d}s e^{-ik_z(z-s)} \frac{e^{-\frac{s^2}{2\sigma_z^2}}}{\sqrt{2\pi}\sigma_z} * \\ & \int_0^a \rho' \mathrm{d}\rho' \int_0^{2\pi} \mathrm{d}\theta' E_0 I_m(k\rho') \cos{(m\theta'+\phi)} \frac{e^{-\frac{\rho_0^2}{2\sigma^2}}}{2\pi\sigma^2} e^{-\frac{\rho'^2}{2\sigma^2}} e^{\frac{\rho'\rho_0 \cos\theta'}{\sigma^2}}, \end{aligned} \tag{5.48}$$

where σ is the r.m.s beam size in the transverse dimension, σ_z the beam size in the longitudinal direction, k the vacuum channel transverse wave number, k_z the longitudinal wave number and ρ_0 is the offset of the beam along the $\hat{x}$-axis. For this derivation we will take $\phi = 0$ so as to align the modes with the $\hat{x}$ axis. The θ' integral can be completed by converting the $\cos{(m\theta')}$ term into exponentials and using the Jacobi-Anger expression, but it is more clear to use the identity [45],

$$\int_0^{2\pi} \cos{(m\theta')} e^{\frac{rr_0}{\sigma^2}\cos\theta'} \mathrm{d}\theta' = 2\pi I_m(\frac{rr_0}{\sigma^2}). \tag{5.49}$$

Next, if the beam radius σ is small compared to the structure radius a, then the radial integral can be performed as

$$\int_0^{\infty} \rho e^{-\frac{r^2}{2\sigma^2}} I_m(k\rho) I_m(\frac{\rho\rho_0}{\sigma^2}) = \sigma^2 e^{\frac{\sigma^2}{2}(k^2+\frac{\rho_0^2}{\sigma^4})} I_m(k\rho_0). \tag{5.50}$$

Using these two identities gives the longitudinal electric field as

$$E_z(\rho,\theta,z) = E_c \cos{(m\theta)} I_m(k\rho) e^{\frac{\sigma^2 k^2}{2}} I_m(k\rho_0) \int_{-\infty}^{z} \mathrm{d}s\, e^{-ik_z(z-s)} \frac{e^{-\frac{s^2}{2\sigma_z^2}}}{\sqrt{2\pi}\sigma_z}. \tag{5.51}$$

The integral over s can be shown to be

$$\int_{-\infty}^{z} \mathrm{d}s e^{-ik_z(z-s)} \frac{e^{-\frac{s^2}{2\sigma_z^2}}}{\sqrt{2\pi}\sigma_z} = \frac{1}{2} e^{-ik_z z} e^{-\frac{k_z^2\sigma_z^2}{2}} \left[1 + \mathrm{Erf}(\frac{z}{\sqrt{2}\sigma_z} - \frac{ik_z\sigma_z}{\sqrt{2}})\right]. \tag{5.52}$$

Finally the expression for the longitudinal electric field can be written as

$$\begin{aligned} E_z(\rho,\theta,z) = & \frac{E_c}{2} \cos{(m\theta)} I_m(k\rho) I_m(k\rho_0) e^{\frac{\sigma^2 k^2}{2} - \frac{k_z^2\sigma_z^2}{2}} e^{-ik_z z} * \\ & \left[1 + \mathrm{Erf}(\frac{z}{\sqrt{2}\sigma_z} - \frac{ik_z\sigma_z}{\sqrt{2}})\right]. \end{aligned} \tag{5.53}$$

For later use this equation is written as

$$E_z(\rho,\theta,z) = \tilde{E}_z(z,\rho_0)\cos{(m\theta)}I_m(k\rho). \tag{5.54}$$

5.3.2 Transverse Forces

We now take a look at the forces on a symmetric beam with a simple offset from the center of the dielectric lined waveguide. Such an example is by no means exhaustive but a treatment of all sources of beam instabilities is beyond the scope of this work [87]. The forces on particles in the fields in dielectric lined waveguides can be derived from the Lorentz Force equation, assuming a beam velocity $\vec{v} = v\hat{z}$,

$$\begin{aligned} \frac{\vec{F}}{q} &= \vec{E} + v_0\hat{z}\times\vec{B}, \\ \frac{F_\rho}{q} &= E_r - v_0B_\theta, \\ \frac{F_\theta}{q} &= E_\theta + v_0B_r. \end{aligned} \tag{5.55}$$

To calculate the forces then we must return then to the equations for the fields as a function of E_z and B_z, Equation 5.10. Using these relations and the relation which sets the phase match between the waves in the guide and the beam, $k_z = \frac{\omega}{v_0}$, the forces are found to be

$$\begin{aligned} F_\rho &= \frac{-iq}{k^2}\left[\left(k_z - \frac{\omega v_0}{c^2}\right)\frac{\partial E_z}{\partial\rho} + \frac{1}{\rho}\left(\omega - k_z v_0\right)\frac{\partial B_z}{\partial\theta}\right] = -\frac{iq}{k_z}\frac{\partial E_z}{\partial\rho}, \\ F_\theta &= \frac{-iq}{k^2}\left[\frac{1}{\rho}\left(k_z - \frac{\omega v_0}{c^2}\right)\frac{\partial E_z}{\partial\theta} + \left(\omega - k_z v_0\right)\frac{\partial B_z}{\partial\rho}\right] = -\frac{iq}{k_z\rho}\frac{\partial E_z}{\partial\theta}. \end{aligned} \tag{5.56}$$

This can be shown the agree with the forces as derived by use of the Panofsky-Wenzel theorem, Equation 4.10. The relation $\omega - k_z v_0$ is identically zero in the vacuum channel, we are looking for modes for which $k_z = \omega/v_0$.

If the forces are converted to their cartesian coordinate equivalents, where it is noted that $\hat{x}$ is the vector between the center of the dielectric lined waveguide and the center of the bunch distribution, then the forces can be written as

$$F_x = \frac{-iq}{k_z}\tilde{E}_z(z,\rho_0)\Bigg(kI'_m(k\rho)\cos^2(m\theta) + \frac{m}{\rho}I_m(k\rho)\sin^2(m\theta)\Bigg)$$
$$F_y = \frac{-iq}{k_z}\tilde{E}_z(z,\rho_0)\Bigg(kI'_m(k\rho)\cos(m\theta)\sin(m\theta) - \frac{m}{\rho}I_m(k\rho)\cos(m\theta)\sin(m\theta)\Bigg). \tag{5.57}$$

5.3.2.1 Monopole Forces

We examine now the forces due to the first TM mode for which m = 0. Furthuremore, for the structures used in this experiment $k\rho \ll 1$ so that an expansion of the Bessel functions can be performed giving

$$\begin{aligned} F_x &= -\frac{iqk_z}{2\gamma^2}\rho\tilde{E}_z(\rho_0,z), \\ F_y &= 0. \end{aligned} \tag{5.58}$$

5.3.2.2 Dipole Forces

Next we look at m = 1 while holding on to the approximation that $k\rho \ll 1$ and find the dipole forces to be

$$\begin{aligned} F_x &= -\frac{iqk}{2k_z}\tilde{E}_z(\rho_0,z), \\ F_y &= 0. \end{aligned} \tag{5.59}$$

The m = 1 modes are shown to act as a dipole force in the direction of offset from the structure axis and are not a function of position.

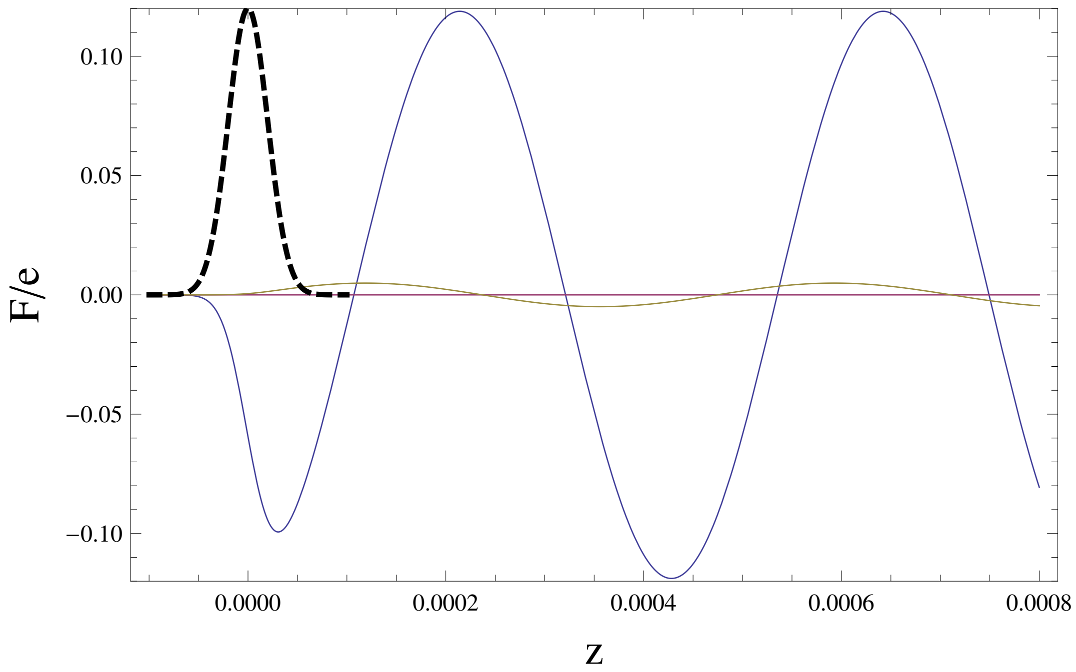

Figure 5.9: The forces in a quartz structure with a=150 μm and b = 200 μm. The black dashed line represents the beam distribution used to excite the wakes. The distribution is modeled to have parameters similar to those which are used in this experiment, $\sigma_\rho = \sigma_z = 30\mu m$ and an offset of 30 μm. The longitudinal force of the TM_{01} mode is shown in blue, the longitudinal force for the HEM_{11} mode is shown in red and the transverse force associated with the the HEM_{11} mode is shown in yellow. As we have elected to offset the bunch in the $\hat{x}$ direction the transverse forces are entirely in the $\hat{x}$ direction.

5.3.2.3 Quadrupole Forces

Examining now the m = 2 mode with the same condition that $k\rho \ll 1$ we see that

$$\begin{aligned} F_x &= -\frac{iqk_z}{4\gamma^2}\rho\tilde{E}_z(\rho_0, z), \\ F_y &= 0. \end{aligned} \tag{5.60}$$

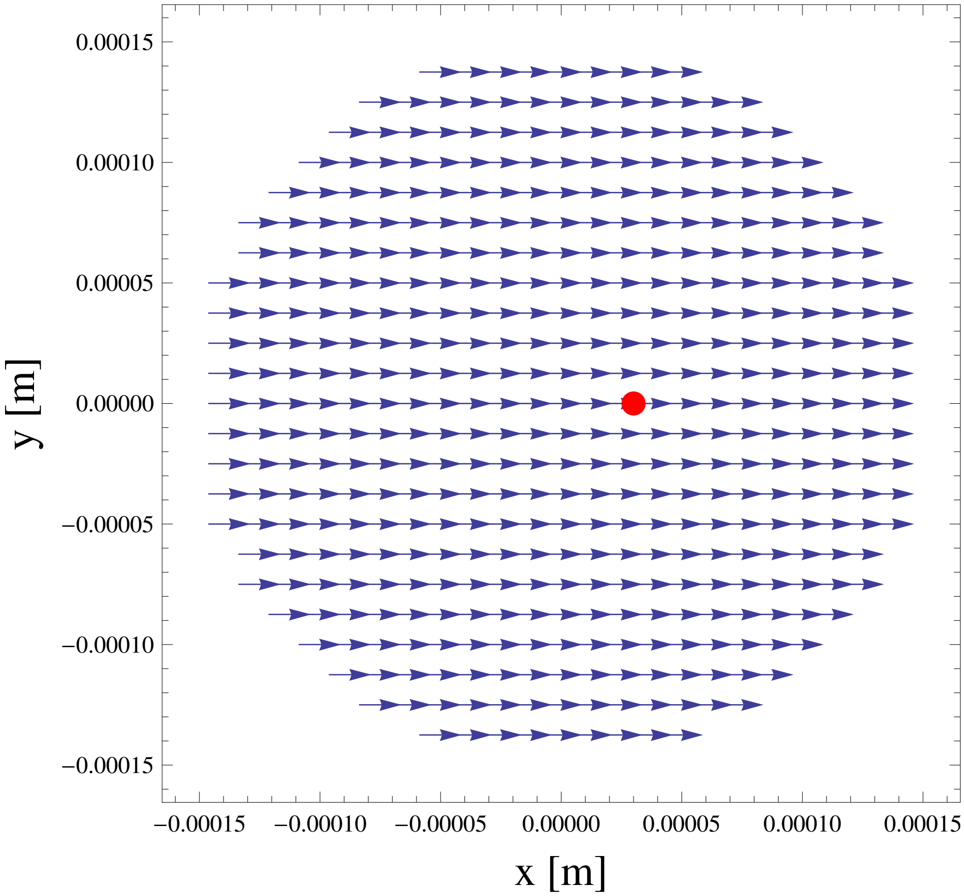

Figure 5.10: The transverse wakefields at the center of the bunch, z=0 m. The pure dipole nature is evident. Also note that the field acts in the direction of the beam offset; it tends to increase offsets, not reduce them.

It is evident that an offset in the structure produces a quadrupole force in only one direction and of a magnitude which is half that of the monopole forces. This analysis can be continued and it will show that to all orders there are only ever forces in the direction of offset.

An example of the forces in a dielectric structure, keeping only the TM_{01} and HEM_{01} fields, is shown in 5.9. As the position of the drive bunch determines the orientation of the fields, the forces in the drive bunch are seen to be defocusing and will be so no matter how the the drive bunch moves. The regions behind the drive bunch which would seem to indicate defocusing are only defocusing while the bunch sits on the same side of the origin as the drive bunch. This indicates there are regions in the wakefield that are accelerating and focusing for both positively and negatively charged witness bunches. The transverse fields, shown Figure 5.10, as mentioned above are not a function of position and are a pure dipole so if the witness bunch passes through the origin the forces will switch sign and continue to push the witness beam toward the structure wall. This effect is related to a set of instabilities called the "Beam Break-Up" instability, or BBU [87] which we shall discuss next.

5.4 Beam Break-Up Instability

Beam Break-Up occurs when an off-axis bunch drives a wakefield which has a dipole component. The dipole component, due to the nature of the fields, affects the back of the beam while leaving the head of the beam undisturbed. To be more explicit, the real part of $\tilde{E}_z$ is Eq. 5.59 is zero at the front of the bunch: particles do not feel self deflecting forces. This leads not only to a difference in head-tail dynamics but in certain circumstances to an unstable growth in the motion of the back of the bunch. We start with a general treatment of beam break-up instabilities and then move on to specific instances relevant to the cylindrical structures used in the experiments contained in this work. We shall see that if left unchecked these dipole modes introduce very strong constraints on the alignment of the beam to the structure.

As an illustration of a beam break-up instability we start with a simple two particle problem where the source of the transverse wakefield, $F_\perp = W_\perp \langle x \rangle$, is a function of the average offset of the particles but is otherwise left arbitrary. As a general rule, any axially symmetric structure will produce a dipole mode if the beam is allowed to move off axis. If the beam is in a continuous focusing channel it will execute betatron oscillations such that the transverse position of the first particle $x_1(s)$ is given by $x_1(s) = x_0 \cos k_\beta s$, where s is the position along the accelerator as defined in Chapter 2. We then define the equation of motion of the second, trailing, particle as

$$x_2'' + k_\beta^2 x_2 = \frac{W_\perp}{\gamma m c^2} x_1(s) = \frac{W_\perp}{\gamma m c^2} x_0 \cos k_\beta s. \tag{5.61}$$

The solutions so this equation is

$$x_2(s) = x_0 \cos(k_\beta s) + \frac{W_\perp}{\gamma m c^2} \frac{x_0}{2k_\beta} s \sin(k_\beta s). \tag{5.62}$$

The position of $x_2(s)$ is seen to grow along the accelerator such that is is possible to define a growth parameter

$$\Gamma = \frac{W_\perp}{\gamma m c^2} \frac{1}{2k_\beta}, \tag{5.63}$$

which naturally depends on the source of the wakefield.

5.4.1 Beam Centroid Motion Along the Structure

To get a gauge as to why beam break-up is important we now derive an expression for the motion of the centroid of the beam in the structure. For this section we shall assume all offsets are in the $\hat{x}$ direction only so that $\rho \to x$. We begin by rewriting Eqs. 5.71 and 5.59 as

$$F_x = \frac{ik}{2k_z} |eE_c| e^{\frac{k_z^2 \sigma_\rho^2}{2\gamma^2}} I_1(kx_0) \int_{-\infty}^{z} \mathrm{d}p\, e^{-ik_z(z-p)} f(p), \tag{5.64}$$

where we have changed the variable of integration from s to p so as not to confuse it with the position along the accelerator. We have also left the longitudinal distribution function undefined. In order to be clear about the direction of the forces we have left no doubt about the presence of implicit minus signs in terms such as qE_c.

It is noted here that the beam is to give up energy to the structure through the Lorentz force, $F_z = qE_z$, where E_z is given by Eq. 5.72. Furthermore, if the real part of E_z is positive over the region of the beam, which is generally the case for bunches shorter than the wavelength of interest, then $F_z \propto -|eE_c|$.

The case for which the longitudinal beam distribution is a Gaussian is shown in Figure 5.9. As a more concrete example we elect to use a square pulse for the beam distribution. Such a distribution is described by the function

$$f(z) = \frac{1}{L}\Theta(\frac{L}{2} - z)\Theta(z + \frac{L}{2}), \tag{5.65}$$

where z is the coordinate in the beam frame, L is the length of the beam and $\Theta(z)$ is the Heaviside step function. This means that F_x is now given by

$$F_x = \frac{ik}{2k_z}|eE_c|e^{\frac{k_z^2\sigma_\rho^2}{2\gamma^2}} I_1(kx_0)\frac{1}{ik_zL}\left[1 - e^{ik_z(z+\frac{L}{2})}\right]. \tag{5.66}$$

The real part of the transverse force is now

$$F_x = \frac{k}{2k_z^2L}|eE_c|e^{\frac{k_z^2\sigma_\rho^2}{2\gamma^2}} I_1(kx_0)\left[1 - \cos\left(k_z(z + \frac{L}{2})\right)\right], \tag{5.67}$$

which shows a force which is defocusing over the length of the bunch. If we make the approximation that $kx_0 \ll 1$, an extremely safe approximation for the structures used in this thesis, it can be shown that the average force on the bunch is

$$\begin{aligned}\langle F_x\rangle &= \int_{-\infty}^{\infty} f(z)\mathrm{d}z\, \frac{k^2}{2k_z^2L}|eE_c|e^{\frac{k_z^2\sigma_\rho^2}{2\gamma^2}} x_0\left[1 - \cos\left(k_z(z + \frac{L}{2})\right)\right],\\ \langle F_x\rangle &= \frac{1}{2\gamma^2L}|eE_c|e^{\frac{k_z^2\sigma_\rho^2}{2\gamma^2}} x_0\left[1 - \mathrm{sinc}(k_zL)\right].\end{aligned} \tag{5.68}$$

Where, from the definition of k, $k^2/k_z^2 = 1/\gamma^2$ has been used. There are two immediate consequences of the above expression. The first is that higher energy beams do not deflect as fast as lower energy beams. The second is that by reducing $k_z L \ll 1$ the average force is reduced as well. For the parameters used in this experiment $k_z \approx 13251\ m^{-1}$ and L $\approx 70\ \mu m$, so that $k_z L \approx 0.92$ and $1 - Sinc(0.92) \approx 0.13$. A length of 70 μm has been used as it is the value for which the average transverse force on the bunch is the same as that of a Gaussian beam constructed using the parameters used in this experiment.

Continuing in this line of thinking, if we assume that the bunch doesn't change energy we can make an estimate for the distance along the accelerator it takes for the beam to move a beam width. To do so we rewrite the force as

$$\begin{aligned} \langle F_x \rangle = \gamma m c^2 \frac{d^2 x}{ds^2} &= \frac{1}{2\gamma^2 L} |eE_c| e^{\frac{k_z^2 \sigma_\rho^2}{2\gamma^2}} x_0 \Bigg[1 - \mathrm{sinc}(k_z L) \Bigg], \\ x_0''(s) - k_S^2 x_0 &= 0, \\ k_S^2 \equiv \frac{|eE_c|}{2\gamma^3 m c^2 L} &e^{\frac{k_z^2 \sigma_\rho^2}{2\gamma^2}} \Bigg[1 - \mathrm{sinc}(k_z L) \Bigg]. \end{aligned} \tag{5.69}$$

The beam parameters for the experiments performed in this work are $e \rightarrow N_e e$ with $N_e = 1.87 * 10^{10}$, $\gamma = 40000$, $|E_c| = 8 * 10^7$, L $= 70\ \mu m$, $k_z = 13251\ m^{-1}$, $\sigma_\rho = 30 \mu m$, which leads to k_S of $7.37\, m^{-1}$. This means that if a bunch starts out at $x(0) = x_0 = \sigma_\rho = 30 \mu m$ and moves to $x(s) = 2 * \sigma_\rho$, it does so at s = 20cm.

As a reminder, the radius of the structures used in this experiment are 150-225 μm. A shift of 30 μm represents a large fraction of the clear aperture we are trying to contain the beam within. This says nothing of the fact that a beam-structure axis alignment of better than 30 μm is a difficult, however not impossible, undertaking in practice. There is also the issue of our prior calculations examining the centroid of the beam; the effects at the back of the beam will be worse on average! We therefore need a method to make alignment to the structure and transport along the structure much more forgiving.

5.4.2 Improving Transport Using External Focusing

The force we are looking to counter is a dipole force related to the lowest transverse mode (HEM_{11}) excited when a beam is injected off-axis in a cylindrically symmetric dielectric structure. Keeping in mind that the condition of off-axis injection occurs in error, the use of a dipole corrector magnet will not work. Since the magnitude of the transverse wakefield is proportional to the offset in the structure we would like a corrector which applies a stronger correction as the beam moves farther off axis. A quadrupole magnet, discussed in Chapter 2, does exactly this.

If we assume a quadrupole magnet system which is perfectly smooth in its focusing strength and axially aligned with the dielectric structure in question we can write down the equations of motion for the tail particle, following Eq. 5.62 as,

$$\begin{aligned} x_2(s) &= x_0 \cos(k_\beta s) + \frac{k_S^2(z_2)x_0}{2k_\beta} s \sin(k_\beta s), \\ \Gamma &= \frac{k_S^2(z_2)x_0}{2k_\beta}, \end{aligned} \tag{5.70}$$

in which we have included explicitly the fact that k_S is to be taken at the x_2 particle position z_2. Equation 5.67 can be used to find k_S. What we see immediately is that with the beam parameters decided, all that remains is to select a quadrupole strength for which $k_\beta^2 = B'/(B\rho)$ [1]. In order to reduce the growth rate of the instability the gradient in the magnetic field must be increased. What we also notice is that as the beam decelerates the gradient will have to be decreased if we wish the growth factor Γ to stay constant.

If we again use beam parameters pertinent to the experiments discussed later in this work and assume a magnetic field gradient on the order of 500 T/m [88]

---

[1] $B\rho$ is called the magnetic rigidity and can be calculated using the formula $B\rho = 333P_0$ T-m where P_0 is entered in GeV/c.

we calculate a growth parameter of $\Gamma = 0.027$. This means that after a meter, for locations where $s = k_\beta(n\pi + \pi/2)$, we can expect the excursions of the tail of the beam to be on the order of 2.7 cm, after starting at 30 μm. For the structures used in this experiment this growth is clearly unacceptable. An exact solution to the problem of beam break-up is the subject of much debate. Next, we provide a brief look at this debate through examining how to select structure parameters.

5.4.3 Optimizing Structure Parameters

In addition to controlling the rate of beam motion off axis by providing external focusing it is possible to tailor the structure parameters to provide preferential excitation of the TM_{01} mode over the HEM_{11} mode. We shall see this requires the careful selection of structure parameters keeping the bunch length of the beam in mind. To begin we analyze the effect of bunch length on the excitation of the different modes in the structure and use the results to make decisions concerning which structure parameters to change and how.

We start our analysis by restating the longitudinal electric field for a given mode as

$$E_z(\rho, \theta, \zeta) = \tilde{E}_z(\zeta, \rho_0) \cos(m\theta) I_m(k\rho). \tag{5.71}$$

where $\tilde{E}_z$ can be defined as

$$\tilde{E}_z(\zeta, \rho_0) = \frac{E_c}{2} I_m(k\rho_0) e^{\frac{\sigma_r^2 k^2}{2} - \frac{k_z^2 \sigma_z^2}{2}} e^{-ik_z\zeta} \left[1 + \mathrm{Erf}\left(\frac{\zeta}{\sqrt{2}\sigma_z} - \frac{ik_z\sigma_z}{\sqrt{2}}\right) \right], \tag{5.72}$$

where we keep in mind that all the parameters which are not coordinates or beam parameters are a functions of the mode in question. This means that things like $k_z \to k_{z01}$ for the TM_{01} and $k_z \to k_{z11}$ for the HEM_{11} mode, and so on.

Using the requirement that $k_z = \frac{\omega}{\beta c}$ in the vacuum channel of the waveguide and the dispersion relation in the vacuum channel $-k^2 = \frac{\omega^2}{c^2} - k_z^2 = -\frac{k_z^2}{\gamma^2}$ the forces can be rewritten as,

$$\begin{aligned} F_z &= -eE_z(\rho,\theta,\zeta), \\ F_x &= \frac{ie}{2\gamma}\tilde{E}_z(\rho_0,\zeta). \end{aligned} \tag{5.73}$$

As we will show later, it is possible to design a system where only the two lowest modes dominate, so we have kept only the two dominant modes. If we expand the Bessel functions in the small parameters $I_0 \to 1$ and $I_1(k\rho) \to k\rho/2$ and also look only along the $\hat{x}$ axis, so $\theta \to 0$. This leaves us with

$$\begin{aligned} F_z(\zeta) &= -\frac{eE_c}{2}e^{\frac{\sigma_r^2k_z^2}{2\gamma^2}-\frac{k_z^2\sigma_z^2}{2}}e^{-ik_z\zeta}\left[1+\mathrm{Erf}(\frac{\zeta}{\sqrt{2}\sigma_z}-\frac{ik_z\sigma_z}{\sqrt{2}})\right], \\ F_x(\rho_0,\zeta) &= \frac{ieE_ck_z}{8\gamma^2}\rho_0 e^{\frac{\sigma_r^2k_z^2}{2\gamma^2}-\frac{k_z^2\sigma_z^2}{2}}e^{-ik_z\zeta}\left[1+\mathrm{Erf}(\frac{\zeta}{\sqrt{2}\sigma_z}-\frac{ik_z\sigma_z}{\sqrt{2}})\right]. \end{aligned} \tag{5.74}$$

We note here that the coupling parameter E_{c01} for F_z is not proportional to γ while E_{c11} for F_x is proportional to γ^2 so that the forces as written here are not a function of γ.

To get an idea of how the forces change as a function of σ_z for a given structure we now restrict ourselves to the case in which the beam distribution function does not evolve as the beam traverses the structure. For longer structures this is not a very good assumption, but for a first approximation it will suffice. To implement this assumption we integrate the forces over the bunch and arrive at,

$$\begin{aligned} \langle F_z\rangle &= -\frac{eE_c}{2}e^{\frac{\sigma_r^2k_z^2}{2\gamma^2}}PR(k_z,\sigma_z), \\ \langle F_x\rangle &= \frac{eE_ck_z}{8\gamma^2}\rho_0 e^{\frac{\sigma_r^2k_z^2}{2\gamma^2}}PI(k_z,\sigma_z), \end{aligned} \tag{5.75}$$

where PR and PI are defined as,

$$\begin{aligned} PR(k_z,\sigma_z) &= e^{-\frac{k_z^2\sigma_z^2}{2}}\int_{-\infty}^{\infty}\mathrm{d}\zeta\, Re\left[e^{-ik_z\zeta}\left[1+\mathrm{Erf}(\frac{\zeta}{\sqrt{2}\sigma_z}-\frac{ik_z\sigma_z}{\sqrt{2}})\right]\right]\frac{1}{\sqrt{2\pi\sigma_z^2}}e^{-\frac{\zeta^2}{2\sigma_z^2}}, \\ PI(k_z,\sigma_z) &= -e^{-\frac{k_z^2\sigma_z^2}{2}}\int_{-\infty}^{\infty}\mathrm{d}\zeta\, Im\left[e^{-ik_z\zeta}\left[1+\mathrm{Erf}(\frac{\zeta}{\sqrt{2}\sigma_z}-\frac{ik_z\sigma_z}{\sqrt{2}})\right]\right]\frac{1}{\sqrt{2\pi\sigma_z^2}}e^{-\frac{\zeta^2}{2\sigma_z^2}}. \end{aligned} \tag{5.76}$$

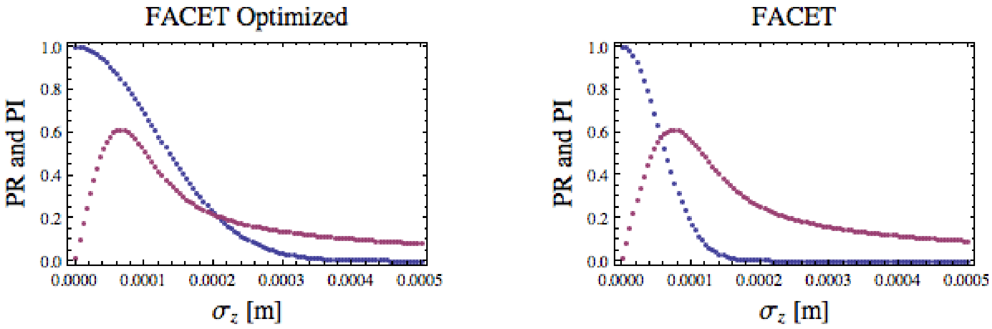

Figure 5.11: $PR(k_z, \sigma_z)$ (blue) and $PI(k_z, \sigma_z)$ (red) for the beam and structure parameters used in the experiments performed in this work are shown on the right. On the left is shown a set of more optimized parameters for the FACET beam. σ_z is allowed to vary to show the relative change in the beam-mode coupling.

For the above equations Re[] and Im[] represent the real and imaginary parts of the functions they contain. This ensures that the average forces described by Equation 5.75 are always real. Examples of PR and PI are shown in Figure 5.11. Here we show that by varying the bunch length it is possible to increase performance. By designing the system this way the optimum does not require pushing to shorter and shorter beams, thus introducing the difficulties of multi-mode excitation.

Aside from attempting to optimize cylindrical structures it should be mentioned that other geometries have favorable qualities which recommend them to use over cylindrical structures. As shown in Figure 5.12 there is no direct advantage to moving to thinner walls in a structure, the frequencies move together with the HEM_{11} mode, always of lower frequency and thus longer wavelength. This means that bunch length tuning cannot be used to preferentially excite the TM_{01} mode over the $HEM11$ mode. The advantage of cylindrical structures is that they are more easily excited, thus produce larger gradients with which to transfer energy. This also means that they more readily produce undesirable transverse

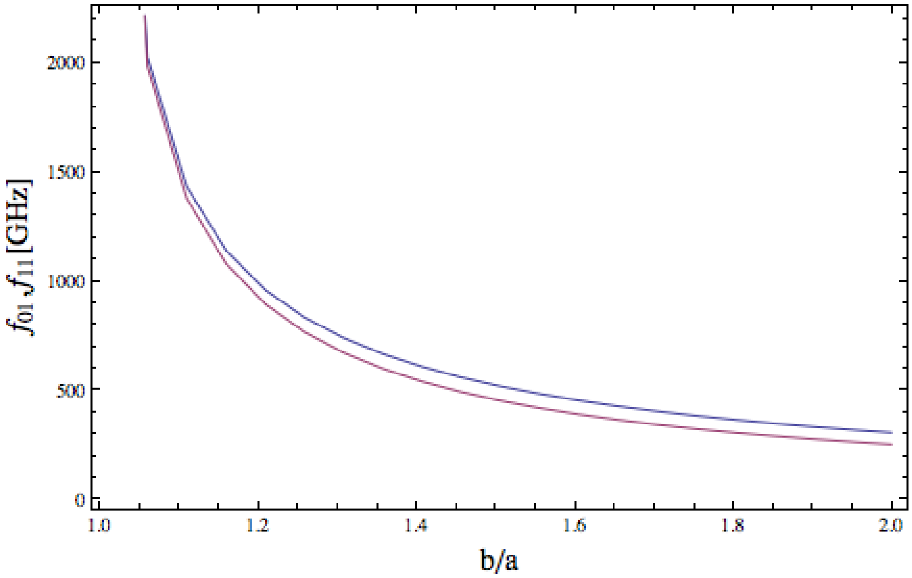

Figure 5.12: The variation of the TM_{01} frequency f_{01} and the HEM_{11} frequency f_{11} with a change in b/a. As shown here there is no advantage to be gained by moving to thinner walls. The frequencies of the two modes move together with the HEM_{11} mode always of lower frequency and thus longer wavelength. Selective excitation of the HEM_{11} mode is thus not possible.

forces.

An alternative to cylindrical structures can be found in slab symmetric structures [89, 4, 6]. If we consider the transverse wave number as a sum of squares of the two transverse coordinates, while maintaining our demand that mode travels down the dielectric structure with a phase velocity equal to that of the beam, we may write the dispersion relation (Eq. 5.7) as

$$k_x^2 + k_y^2 = \frac{k_z^2}{\gamma^2}. \tag{5.77}$$

It is then seen that if we allow the energy of the particle to become very great we must have $k_x^2 \approx -k_y^2$. If slab (or cartesian) symmetry is used and the $\hat{x}$ direction is taken to be extremely large then $k_x \to 0$. In this situation then k_y must also be zero and via the Panofsky-Wenzel theorem there are no traverse wakes. Taken to a slightly more realistic extreme it can be shown that systems where the beam has a very pronounced aspect ratio $\sigma_y \gg \sigma_x$ will have marked reduced transverse forces when compared with the cylindrical case [89].

There are additionally, other structure worth exploring such as Photonic Band Gap structures [90], dielectric woodpile structures [91] as well as slab symmetric structures which use a Bragg layer as a boundary, instead of metal [92].

5.5 Computational Methods and 3D PIC simulations

To complement the measurements to be made it was both necessary and desirable to calculate the spectrum excited in a given structure as well as the energy lost, due to a particular beam shape. As the exact beam parameters do not admit a tractable set of equations to calculate such absolute quantities simulations were used to fill in the information gaps. To that end a Mathematica [93] and Matlab [94] program were written to solve for the modes of a given structure and the beam's coupling to those modes in 1D. This required essentially solving the previously mentioned transcendental equation in search of the κ_{mn} wave numbers of the structure and applying the superposition of wakes to a measured longitudinal bunch profile, Eq. 4.18. In addition a 3D PIC code VORPAL [95] was used to completely capture all possible 3D effects.

An example of such 3D simulations is shown in Figure 5.13. The plot shows a VORPAL simulation compared to a Mathematica simulation, and the two are seen to agree quite well. After extensive testing it was determined that VORPAL simulations were computational expensive and time intensive for results that were

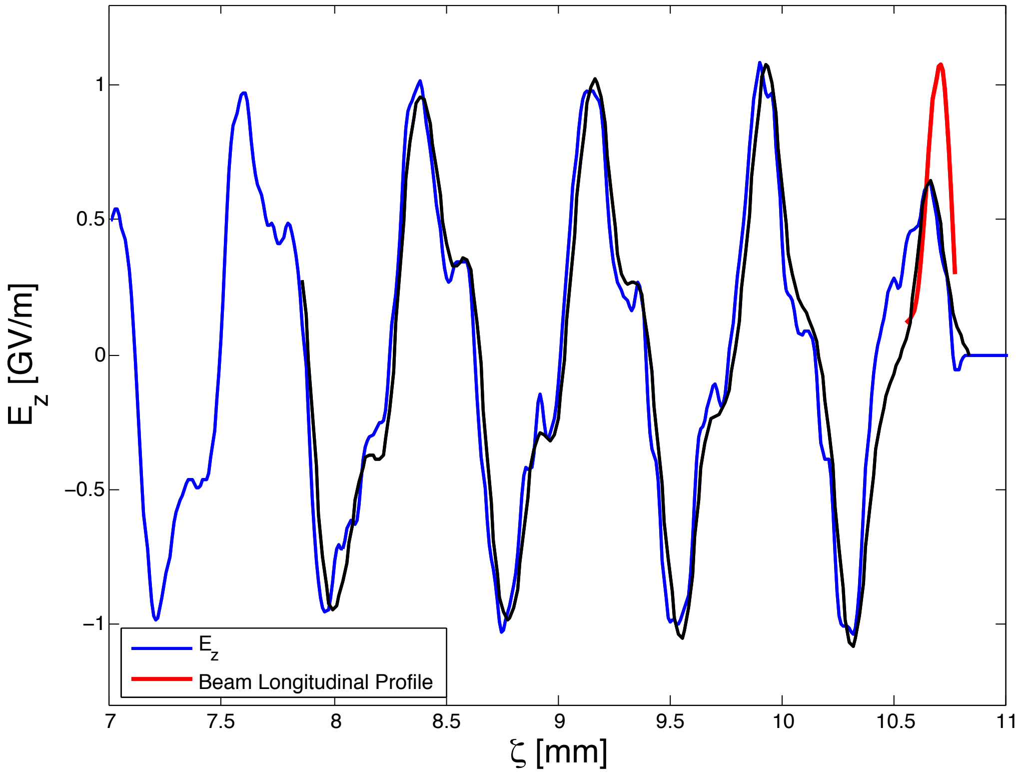

Figure 5.13: A VORPAL simulation showing the expected wakefield (blue) from a beam using parameters measured during experiment. The beam profile (red) is a reconstruction using Kramer-Kroenig techniques of Coherent Transition Radiation generated at a titanium foil at the interaction point and passed through a Michelson interferometer. (black) Theoretical wakefield calculated in Mathematica using the beam re-construction distribution mentioned above.

more easily obtained through other methods. To that end, VORPAL is only used when testing new physical scenarios and to assist in developing them in much faster custom codes.

This specific example shown in Figure 5.13 are the simulations run for the a = 225 μm, b =320 μm case. Here we see that the Cherenkov radiation excited is comprised of two modes. The large amplitude oscillation is the TM_{01} mode while the "kinks" that give the electric field its dogtooth appearance is the TM_{02} mode. For this simulation the beam was assumed to be on axis and thus should not excite the HEM modes. This should be compared with the relative strength of the modes as measured in Figure 6.5.

CHAPTER 6

Experiment

The goal of the experiment was to test the limits of dielectric lined waveguides as accelerators. Specifically we were looking to expand on previous work [26] by showing that these structures are capable of handling sustained fields very close to the breakdown limit, or failing that, the structures support fields well in excess of what is considered nominal for conventional accelerating structures. As an accelerating system a structure which only briefly holds large gradients before needing to be replaced is not very useful. What we show here is that these structures are capable of handling gradients in excess of 1.35 GVm^{-1}, a greater than factor of 50 improvement over the standard S-Band copper RF structures. These fields were sustained for many hours at a repetition rate of 10 Hz, or many tens of thousands of pulses.

We start with an overview of the Facility for Advanced aCcelerator Experimental Tests (FACET) at SLAC National Laboratory. We follow this with a description of the experiments themselves and the methods for structure fabrication. Finally we describe the data analysis and results in detail.

6.1 FACET

The FACET facility at SLAC was developed for the testing of Plasma Wakefield Acceleration (PWFA) using the high-energy, high-current beams produced by

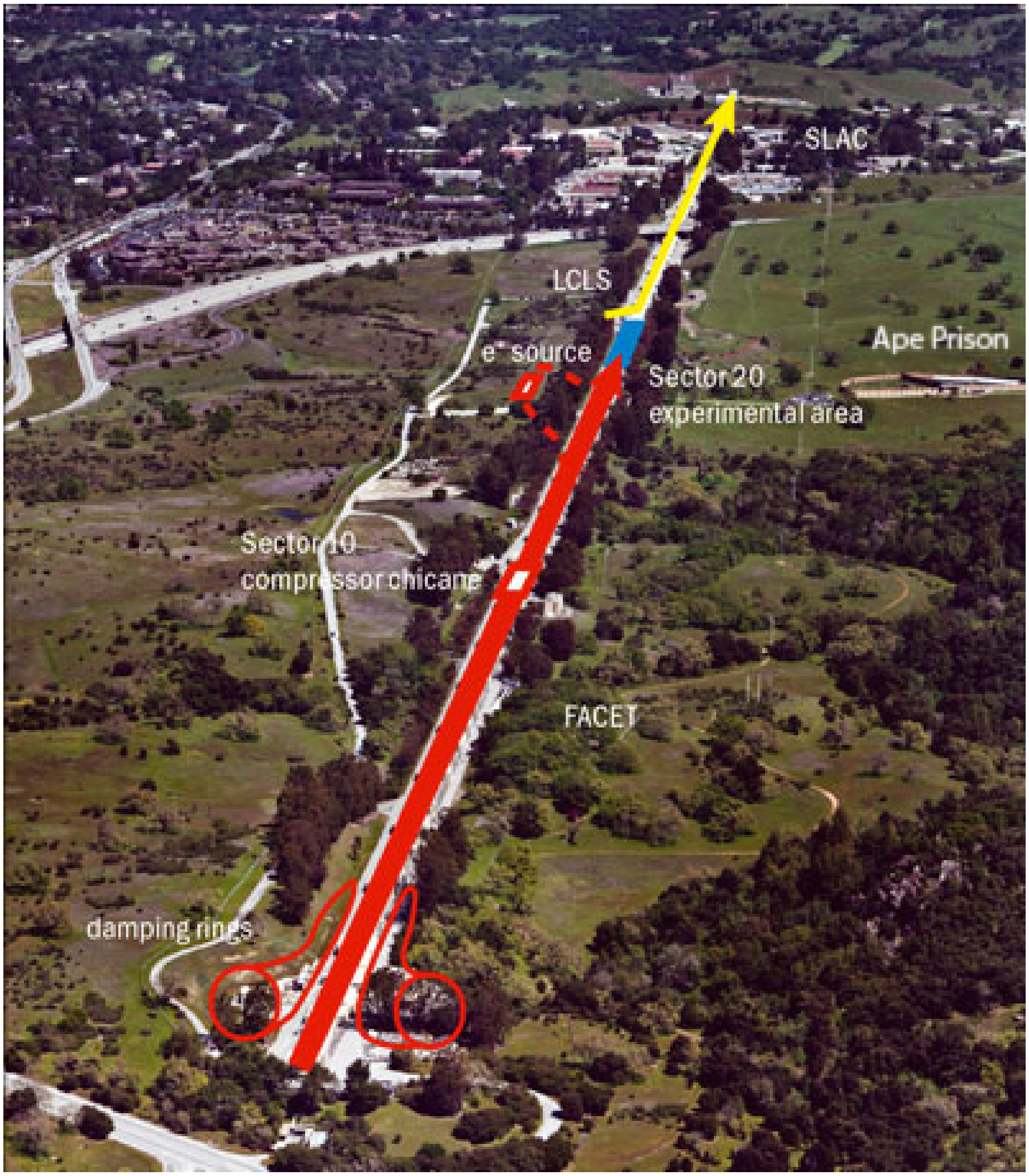

Figure 6.1: An aerial photograph of the FACET facility at SLAC.

the SLAC linac. The facility makes use of the first 2 kilometers of the SLAC linac which were left vacant after elementary particle experiments were ceased at SLAC in favor of x-ray production by the Linac Coherent Light Source (LCLS) [18]. An aerial photograph of the facility extent is show in Figure 6.1.

Table 6.1: A table of common beam parameters found at FACET. These numbers are for both electrons and positrons.

Parameter	Value	Unit
Beam Energy	20.35	GeV
Charge	3	nC
Beam Size @ IP	30x30	μm
β-function	0.15x2.0	m
Bunch Length	20+	μm

FACET is capable of producing both electrons and positrons in bunches as small as $\sigma_x \times \sigma_y \times \sigma_z = 30 \times 30 \times 20 \mu m$ containing upwards of 19 billion particles. This represents peak currents in excess of 45 kA, by far the largest in the world. As the devices tested in this experiment produce fields proportional to the current (Equation 5.31), FACET represents a unique opportunity to examine the physics of beams and structures under incredibly intense fields. A list of common beam parameters found at FACET is shown in Table 6.1

6.2 Structure Parameters

The selection of structure parameters was performed in two stages. To begin with generous allowances were made for clear aperture passage of the beam through the structure. The standard gauge is to ensure the structure diameter is 10 times the beam r.m.s width. For a beam with an r.m.s width of σ_r =30 μm this means using structure of at least 300 μm inner diameter. We started the experiments with 450 μm as they offer 15 σ_r clearance and so were very forgiving in terms of testing alignment procedures and model verification. For model verification it was critical to ensure that structure impact was eliminated as a source of error during model verification.

Once the model used to describe the experiments was confirmed we then moved to longer and smaller structures. As was outlined above, the longitudinal forces experienced by the beam are proportional to a^{-2}, so in order to reach incredibly high fields it is necessary to go as small as possible. To that end structures as small as 100 and 200 μm inner diameter were also tested. However these structures were extremely difficult to align and thusly suffered catastrophic loss of metallic coating and dielectric damage. As will be evident when discussing the alignment procedure, these structures were always unlikely to provide useful gradient details. They were introduced to beam anyway in order to set a standard for how beam impact or extremely high field damage manifested in the present group of structures.

Before we move on to the experimental description we remark that these structures are usually spoken of in terms of inner diameter, outer diameter and length. This means that we refer to the first structure listed in Table 6.2 as 450/640, 1 cm long. A list of all the structures used to present quantitative data in this work is given in Table 6.2.

6.3 Experimental Description

The essential goal and procedures for the experiment are very straight forward. Align a very small dielectric lined waveguide to the particle beam and measure the beam energy after the interaction point, both with and without the structure in the beam path. An additional measurement is performed which measures the

Table 6.2: The structure parameters used in the experiments presented here.

Inner Diameter a [μm]	Outer Diameter b [μm]	Length [cm]	Material
450	640	1	SiO_2
450	640	10	SiO_2
400	600	15	Quartz
300	400	15	Quartz

modes excited in the structure by measuring the frequency content of the coherent Cherenkov radiation (CCR) produced in the structure. Thusly the experiment is said to progress in two parts. First, measuring the change in beam energy is said to account for the beam side of the beam-structure interaction. Second, measuring the mode content of the radiation generated is said to quantify the structure side of the beam-structure interaction. In this way it is possible to eliminate sources of systematic error by checking the results against one another. A graphical representation of the experiment is shown in Figure 6.2.

Due to limitations in the apparatus used in this experiment, the experiment is further divided into two different structure regimes: short and long structures. Specifically, the detectors used to characterize the radiation left behind the beam as a wakefield have a maximum measurable energy of 5-6 millijoules. The shorter structures are expected to produce around 10 mJ of CCR in addition to ∼10 mJ of diffraction radiation from all apertures in the system. The longer structures used in this experiment are capable of producing upwards of 500 mJ of radiation. This magnitude of radiation is easily enough to saturate the detectors. In contrast the beam energy is on the order of 60 J (at 20.35 GeV), so that in order to measure a 10 mJ shift in the beam energy we would require the ability to differentiate

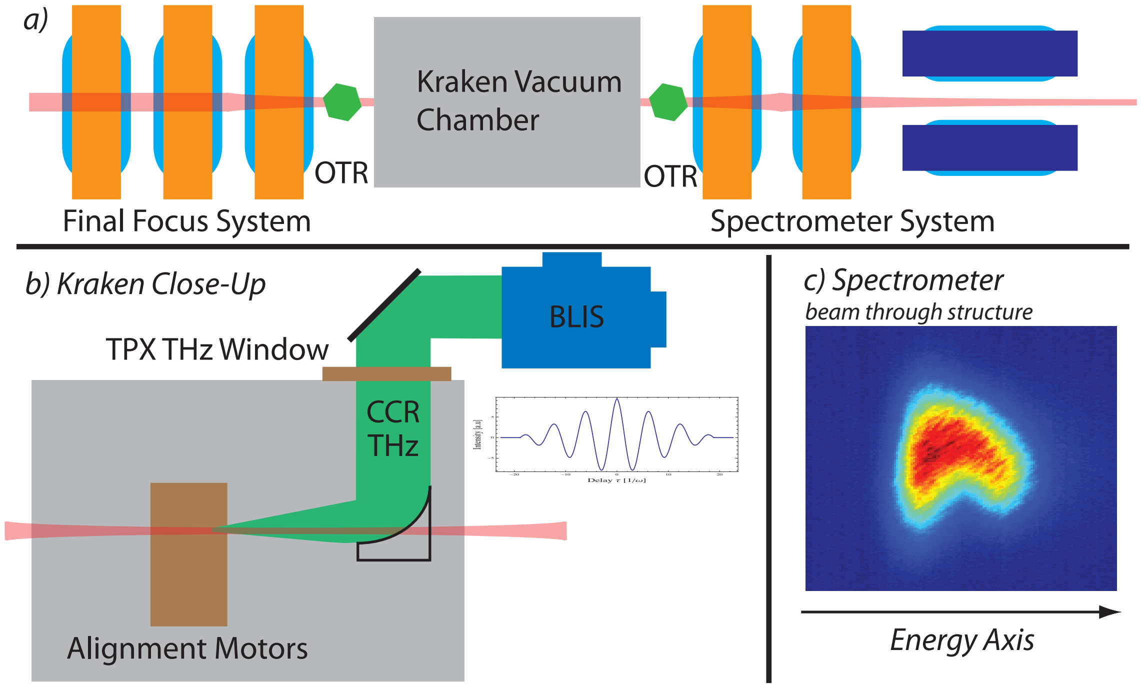

Figure 6.2: A graphical representation of the experiment. a) The beam arrives from the bunch compression system and is focused down by the final focus system and transported through the experimental chamber known as the "Kraken". The beam is then recaptured by the quadrupoles of the spectrometer system and passed through a dipole magnet which separates the particles by energy. A sample of what an image on the beam looks like after the spectrometer is shown in c). A close up of the in vacuum system inside the Kraken is shown in b).

a mean energy difference of ∼3 MeV between the nominal and beam-through-structure cases. In contrast, for the longer structures an energy shift of 500 mJ leads to a mean energy difference of 167 MeV, which is much easier to measure.

The stages of the experiment are conducted as follows. First, the spectral content of the radiated wakefield generated in a one centimeter long structure is measured. This verifies the model of the beam-structure interaction through inspection of the modes excited by the passing electron beam. Second, the spectral content of the radiation generated using a ten-centimeter structure is measured and the average energy loss of the electron beam after passing through the structure is measured. This measurement bridges the gap between the two regimes in that both the radiation and the beam energy are measurable. Finally, after the model has been verified using the shorter structures, the beam is sent through a fifteen-centimeter long structure and the average change of beam energy is measured.

It is worthwhile to note at this point that the experiment is chiefly concerned with the energy given up by an electron beam to a dielectric lined waveguide. There was no witness beam available for the experiments performed in this work. The system however can still be fully characterized and the accelerating gradient behind the bunch can be inferred via the *Fundamental Theorem of Beam Loading*. As it is customary to speak in terms of accelerating gradient, we will endeavor to avoid confusion by mentioning when we speak of decelerating as opposed to accelerating gradient.

6.3.1 Beam Energy Change

To perform the experiment an electron beam generated in the SLAC injector and damping system and is accelerated to an energy of 20.35 GeV. It is then compressed longitudinally in a W-chicane [96] and passed to the final focus system for FACET. This focusing system sets the beam size and focal parameters of the electron beam through the interaction point. After passing through the interaction point the beam passes through a hole in the collecting off-axis paraboloid and is captured by a series of quadrupole magnets, ostensibly set to an imaging condition. Then the beam is passed through a dipole spectrometer magnet which disperses the particles based on their energy. The beam then passes through a Cherenkov air gap in which the Cherenkov radiation generated by the beam is imaged. The Cherenkov radiation imaging system is calibrated using the base line energy of the linac, measured magnetic field parameters and against other energy measurements made in dispersive sections upstream of the interaction point. The Cherenkov radiation generated here is not to be confused with the radiation generated in the structure. This system is many meters away from the structure which is at the interaction point and the source is the extremely small difference of the index of refraction between air and vacuum. For this system the bend direction is the y direction, thusly we will chiefly be interested in the R_{33} and R_{34} elements of the transfer matrix when discussing sources of error in the measurement.

The calibration of the spectrometer system is measured to be 15 MeV/pixel, with a physical pixel width of 25 μm. As the r.m.s energy spread of the beam is measured to be around σ_E=300 MeV the beam is seen to span approximately 120 pixels at 6 σ_E width. Since we are interested in a measurement of the average, or centroid, energy of the beam we are left in essence with performing the Middle Riemann Sum approximation to the first moment of the distribution function. The error to such an approximation is given by

$$Error \leq \frac{M_2(b-a)^3}{24n^2}, \tag{6.1}$$

where b-a is the span of the integral approximated by the sum, n is the number of sub intervals in the approximation and M_2 is the maximum of the absolute value of the second derivative of the function being integrated. For these calculations it suffices to assume the energy spread is well approximated by a Gaussian so that $M_2 = \sigma_e^{-2}$, (b-a) = $6\sigma_E$ and n=120. As a result the error in measuring the average energy of the beam is expected to be less than or equal to 0.2 MeV.

This represents ∼10% of the smallest measurement made using the spectrometer. Furthermore, as outline below it is small compared to the energy jitter due to other sources in the linac and thusly shall be ignored.

The true challenge of the measurements presented here is the differentiation in average energy of a population of measurements which is subject to variations in the average energy for reasons other than the structure's presence in the beam path. These can include things like klystron interruption or general feedback manipulation. As the specific correction used depends on the properties of the measurement we wish to make, these effects will be taken into account and discussed during the presentation of individual measurements.

6.3.2 Mode Content of Cherenkov Radiation

Table 6.3: The frequency of the lowest four modes supported by the structures in this experiment. It is possible to have lower frequencies for small structures as in the 400/600 case due to changes in the ratio of outer/inner diameter b/a (see Figure 5.12) and changes to structures based on manufacturing tolerances.

Size [μm]	TM_{01} [GHz]	TM_{02} [GHz]	HEM_{11} [GHz]	HEM_{12} [GHz]
450/640	420	1240	372	625
400/600	392	1120	342	573
450/640	700	2140	632	1070

Figure 6.2.b) gives a visual account of the experimental layout for measuring the radiated wakefield. For this aspect of the experiment the radiated wakefield left by the beam in the structure is collected by an impedance matching horn and launched into free space. After traveling a distance of approximately

15 centimeters the radiation is collected and collimated by an off-axis parabolic mirror which completely subtends the solid angle represented by the launching horn. From there the radiation is transported to a scanning Michelson interferometer where an interferogram of the radiation is produced. A Fast Fourier Transform (FFT) of the interferogram is performed and the frequency content of the wakefield is obtained. Since the structure only supports very specific modes, c.f. Figure 5.7, the modes excited in the structure are in general unambiguous. This is not to say that the polarization of the modes was observed, just that the spectrum of each mode is distinct such that given a measured frequency the mode excited is obvious. While attempts to measure the polarization of Coherent Transition Radiation generate have proven successful [97], the devices used are extremely sensitive and prone to damage unless the source is extremely well characterized. Thusly, such measurements have been left for a later date.

An exception to the previous statement regarding the ambiguity of mode observation is made for the case in which the TM_{01} and HEM_{11} modes are very close to one another in frequency space. In such a case, as we will see in the Results section of this work, it is possible for a relatively weak HEM_{11} mode to be masked in the bandwidth of the TM_{01} mode.

6.4 Structure Fabrication

The procedure for producing the structures leverages previous work [82] and knowledge gained from work on other projects [98]. The process begins by purchasing off-the-shelf silicon dioxide and quartz capillaries. The structures are cleaved to lengths appropriate to fitting in the machines used later in the fabrication process and cleaned using acetone and methanol. The capillaries are then transferred to a physical vapor deposition system and a 30 nm seed layer of aluminum is deposited on the bare fibers followed by 500 nm of copper.

The seed layer of aluminum is necessary as the enthalpy of formation of aluminum oxide is lower than that of silicon dioxide, so bonds between the capillaries and the aluminum form readily. In contrast the enthalpy of formation for copper oxide is higher than that of silicon dioxide, so energy would be required to keep the bond stable [99]. While this is not the complete picture as the bond mixes silicon-oxygen-aluminum it does provide an explanation for the flaking and poor adhesion observed when attempting to deposit copper directly on silicon dioxide [100].

After the initial layer of 30 nm of aluminum and 500 nm of copper are vacuum deposited the capillaries are dipped in acetic acid to etch back the outer 10 nm of oxidation generated when the structures are removed from the deposition system and then dried in a pressurized nitrogen environment. The structures are then transferred to a 3D printed plating fixture and submerged in a sulfate-based copper electroplating bath and copper is further deposited to 15-50 μm thick. After electroplating the structures are transferred between various chemical baths to remove any remaining salts and chemicals. The structures are then dried in a vacuum desiccator, a picture of which is shown in Figure 6.3.

When dry the structures are aligned and mounted on a silicon wafer and an acetone soluble photoresist is used to hold them in place. The photoresist also provides support during the cutting process which helps prevent shatter of the structures. The structures are then cut to size using a diamond saw. This allows cutting to better than millimeter accuracy and leaves a flat, clean surface which is necessary for adequately coupling radiation out of the structure. After cutting, the photoresist is removed with acetone and several alternating chemical baths which leave the structures residue free.

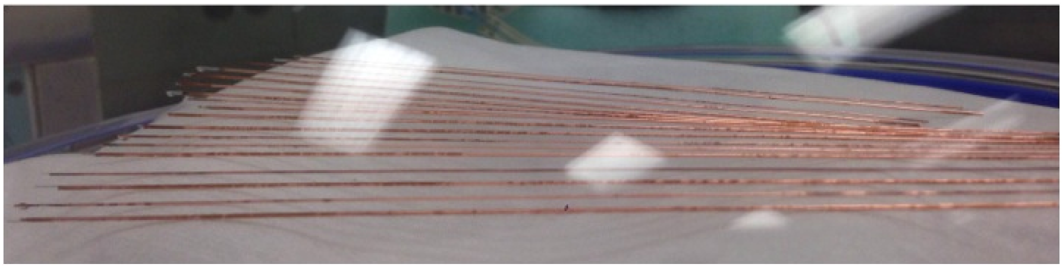

Figure 6.3: A picture of the a set of structures drying in a vacuum desiccator. The method of production is not unique to each size structure so that they can all be produced efficiently at the same time. Observable on the left side of the image is the uncoated ends which were covered during deposition and plating to hold the structures in place. These uncoated ends will be later cut off.

6.5 Structure Alignment

The alignment of the structure to the beam is a multistep process that makes use of a five-axis stage mounted on two orthogonal "long haul" stages. The long haul stages are used for gross alignment and quickly moving the structures in and out of the beam path. Once aligned it takes approximately 30 seconds to switch between structure in and structure out of the beam path. This fast switching is helpful in allowing us to interleave measuring sections so that systematic errors due to feedbacks and other effect like heat during time of day can be eliminated.

The ability to align such small structures as used in this experiment to an electron beam is a technical challenge solved by persistent effort. Many years of trial and error has lead to the following recipe for alignment. First the beam vector through the interaction region is taken. To do this it suffices to mark the beam position both upstream and downstream of the interaction point. Next, the beam is shut-off, or sent elsewhere, and a laser of appropriate Rayleigh length is aligned to the beam location marks. The structure is then aligned to the laser where laser beam quality and over all transmission are checked, an example showing the result at the end of this step is shown in Figure 6.4. Finally, the beam is returned to the interaction area and its location relative to the previous recorded location is checked. If the beam vector is still on, or close, to the vector used to align the structure, the structure is moved into the beam path.

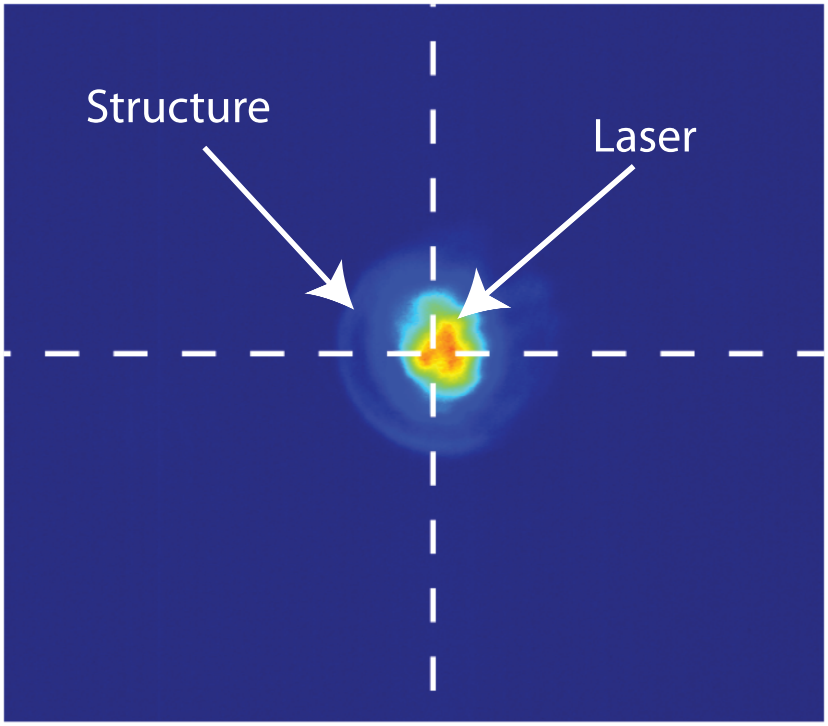

Figure 6.4: An example picture showing the alignment laser through one of the 10 cm structures used in this experiment. This image was taken of the downstream (radiating) surface of the structure.

To ensure beam is adequately transported through the structure integrated current transformers (ICT) are monitored during the experiment. Data is collected on ICTs both before and after the structure and also compared between structure in the beam path and structure out of the beam path. Furthermore, if a beam were to impact the structure, or its holder, the radiation generated is visible on Panofsky Long Ion Chamber (PLIC) radiation detectors [101] in the experimental hall. Beam-structure impacts are also observable on the spectrometer screen, after impact the beam shape is heavily distorted due to emittance degradation. All three methods of loss detection showed no loss of electrons during transport through the structure.

During the experiment it was necessary to verify the integrity of the structures to ensure the energy loss of the beam was due to the generation of a wakefield capable of acceleration. Prior experiments showed two methods of damage to dielectric wakefield structures [26]. The first is loss of the metal coating due to ablation. To ensure the structures retained their metal cladding a high resolution, long focal length optical diagnostic was used to monitor the state of the structures; bright flashes are visible when the metal coating is blown off the structures. The second damage mechanism is damage to the dielectric itself, described as browning and cracking. These two events were shown to affect the ability of the structures to transport light [26]. In case of dielectric damage a relative change in Cherenkov radiation signal would be expected due to disruption of the TM_{01} mode and the guiding in the structure. Furthermore, a change in signal would also be expected for a structure that is no longer capable of transporting the desired modes along the structure due to a loss of the metal coating. No such changes in Cherenkov signal were observed. Additionally, when the structures lose their metal coating light from the alignment laser leaks through the structure walls whereas an intact tube appears opaque. The alignment lasers transverse profile is expected to change when transported through a tube with a damaged dielectric. No such distortions in metal coating or laser profile were observed. This leads us to conclude that a wakefield capable of acceleration was present for all data collected during this experiment.

6.6 Data Analysis and Results

6.6.1 Coherent Cherenkov Radiation

We start our discussion of the results with the measurements made of the mode content of the radiation generated in the structure. A summary of the finding is shown in Figure 6.5. Figure 6.5.a) shows what a typical autocorrelation trace looks like for this experiment. In this case the plot shown is for a 1 cm long 450 μm/640 μm structure. Below that in b) is the spectral content of the trace shown in a). Directly observable is the TM_{01} at 422 GHz and the TM_{02} at 1.27 THz. This is the genesis of the use of these structures as sources of radiation in the THz regime. Figure 6.5.c) shows the spectral content of the radiation generated in a 10 cm long 450 μm/640 μm structure.

What the figure illustrates is two-fold. First, the fact that the radiation pulse length is proportional to the length of the structure means we would expect a smaller bandwidth for a longer structure. The length of the pulse is expected to be

$$L_r = L_s \frac{(1-\beta_g)}{\beta_g}, \tag{6.2}$$

where L_s is the length of the structure and β_g the group velocity of the mode normalized to the speed of light. This manifests itself as the spectral narrowing of the TM_{01} mode in Figure 6.5.c). The second observation is an illustration of the effect discussed earlier in which the longer structures make it more difficult to make a spectral measurement. In this case the energy is high enough to cause clipping of the waveform which results in signal leakage and the apparent loss of the TM_{02} mode. This is all despite the fact that the total energy radiated into the TM_{02} is increased by a factor of 10. Figure 6.5.d) shows the spectral content of the radiation generated as the beam passes through a 10 cm long 400 μm

steel structure. This is used as a control test and shows the broadband radiation present at 1 THz in all three cases is a product of some element in the beam path other than the dielectric lined waveguide.

Our earlier discussion of transition and diffraction radiation showed that both of these types of radiation should be smooth functions which are continuous to zero frequency. Thus, if radiation shown in Figure 6.5.d) is indeed related to either transition or diffraction radiation there is yet another effect that causes the spectrum of this particular radiation to truncate, while allowing the modes in the dialectic structure to pass. As the radiation around 1 THz does not shift with a change between dielectric structure and cylindrical waveguide it is not thought to be related to simple cylindrical TM modes.

If the pulses are assumed to be square pulses, the resulting bandwidth is a sinc function with a full-width-at-half-maximum bandwidth, for a given mode, equal to $f_{FWHM} = 3.8/(\pi T)$, where T is the length of the pulse in time. Such an estimate leads to a calculated bandwidth in the TM_{01} of 20 GHz (5%) in the the 1 cm length case and 2 GHz (0.5%) in the 10 cm case. Disagreement with the measured values of 14.6 % and 6.6 % are seen to be the result of a more detailed model necessary when calculating the bandwidth. From the autocorrelation alone it is seen that a decay constant that behaves like $e^{-\alpha t}$ is necessary. Moving then to a ramped pulse profile the full-width-at-half-maximum bandwidth of the TM_{01} mode is expected to be 76 GHz (18%) for the 1 cm case and 7.6 GHz (1.8%) for the 10 cm case. In both calculations the theoretical pulse length of 62 and 620 ps is used. The agreement is now seen to be much more reasonable. In order to properly resolve the bandwidth in the 10 cm case the Michelson interferometer would have to scan for a much longer range, thus increasing the resolution of the fast Fourier transform.

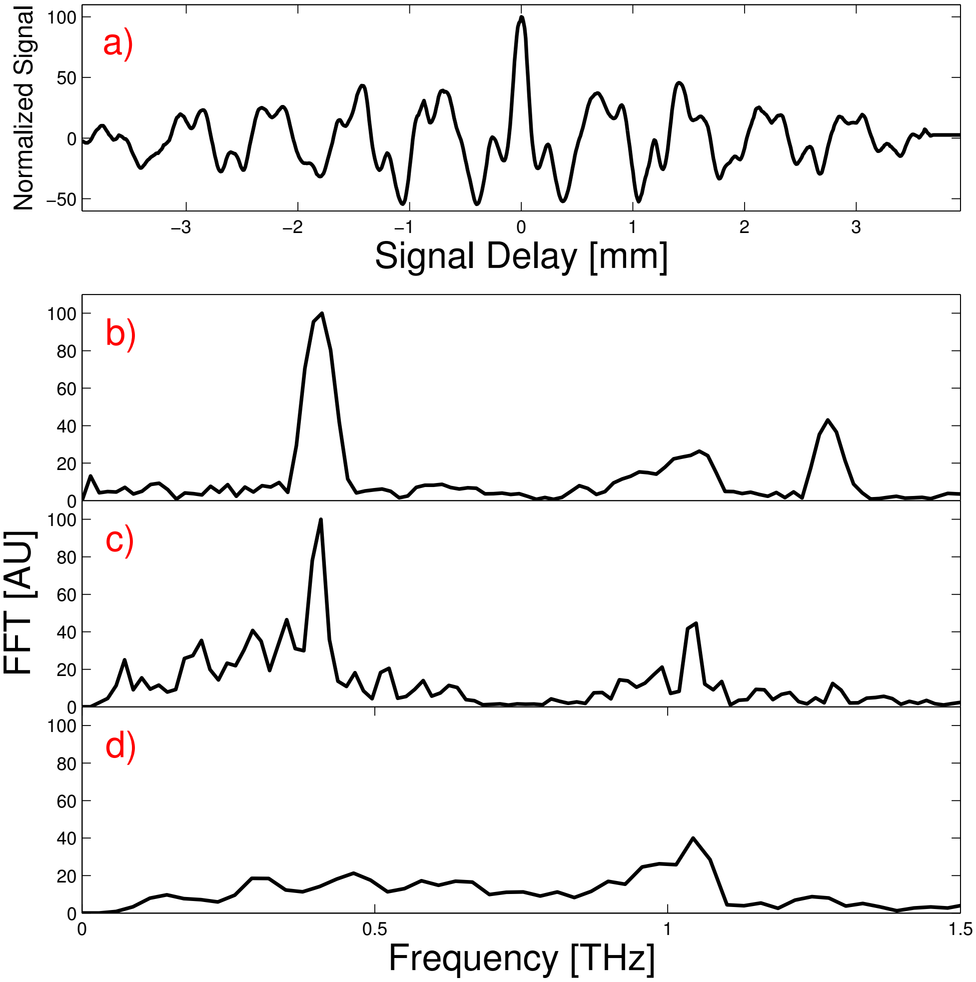

Figure 6.5: A sample of autocorrelation and spectral plots for several structure geometries. a) Shows an autocorrelation trace generated by a 1 cm long 450 $\mu m/640\ \mu m$ structure. b) Is the spectral content of the autocorrelation shown in a). Of note is the TM_{01} excited at 422 GHz and the TM_{02} at approximately 1.27 THz. c) Show the spectral content of a 10 cm long 450 $\mu m/640\ \mu m$ structure. d) Shows the spectral content of the radiation generated when the beam passes through a 10 cm long 400 μm steel structure, i.e. no dielectric.

Examination of Table 6.3 shows that the HEM_{11} mode is expected to be very close to the TM_{01} mode, so much so as to be inside the bandwidth of the TM_{01} mode. The resolution of the existence of the HEM_{11} mode is through looking for the HEM_{12} mode and at the beam deflection downstream. Furthermore, theory and simulation shows that energy coupled into the HEM modes is three orders of magnitude smaller than into the TM modes, when using a reasonable offset. This means that even if the modes were excited they are unlikely to be observable in the spectrum of the modes excited in the structure. Knowing this we look instead for movement of the beam on non-intercepting Beam Position Monitors (BPMS) and on the spectrometer screen. As no motion for the 450/640 case is observed it is safe to assume all energy loss is into the TM_{01} and TM_{02} modes. We examine the specific cases of HEM excitation for the smaller bore structures in the energy loss section.

6.6.2 Minimum Phase Reconstruction of the Coherent Cherenkov Wakefield

With the spectral composition of the radiation as generated in the wakefield known, it is possible to perform a minimum phase reconstruction of the pulse. This allows a view inside the structure at the pulse shape and field profile. While similar, this is not to be confused with the wake potentials [102]. An integral over the wake is not performed, thusly any slippage that may occur due to the differing group velocities for differing modes is not taken into account.

The reconstruction for the previously shown spectral data from the 1 cm a = 450 μm, b = 640 μm structure is shown in Figure 6.6. Here we have also added

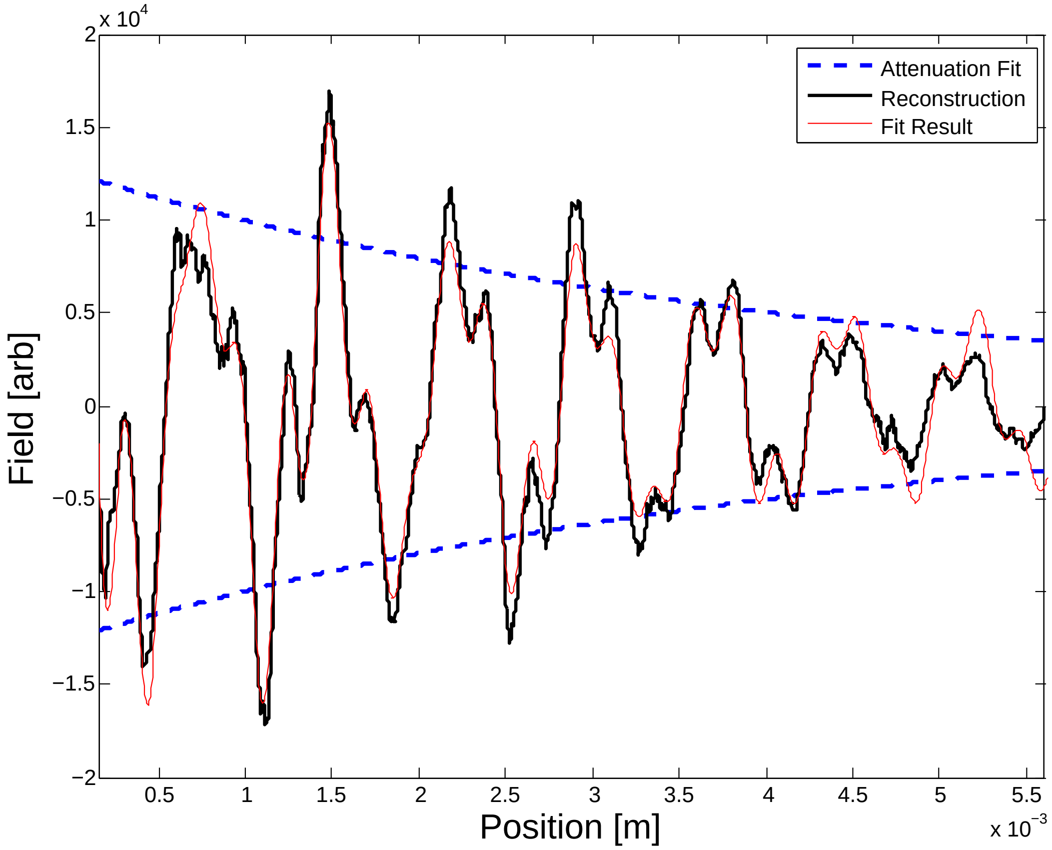

Figure 6.6: A plot showing the reconstruction of the 1 cm data previous described is shown in black. A fit to the data using Equation 6.3 is shown in red, while the resulting attenuation parameter α_1 for the TM_{01} mode is plotted in dashed blue.

a plot showing a three cosine fit using the function

$$fit(z) = C_1 \cos{(k_1 z + \phi_1)} e^{-\alpha_1 z} + C_2 \cos{(k_2 z + \phi_2)} e^{-\alpha_2 z} + C_3 \cos{(k_3 z + \phi_3)} e^{-\alpha_3 z}. \tag{6.3}$$

The results of the fit are shown in Table 6.4. It is seen that the first and last entries correspond to the wavelengths expected from theory (c.f. Table 6.2). The center point is the beam related radiation discussed in the previous section.

Table 6.4: The parameters resulting from a fit to the minimum phase reconstructed data using Eq. 6.3. The first and last match quite well the theoretically expected wavelengths for the TM_{01} and TM_{02} modes.

	C	λ [μm]	ϕ [rad]	α [1/m]
1	12500	738	-0.125	227
2	7500	258	4.97	632
3	5400	235	4.65	256

Of interest in the fit data are the attenuation parameters α. The model for a given waveguide system is, up to a factor of two [17, 103],

$$\frac{\mathrm{d}P}{\mathrm{d}z} = -\alpha P. \tag{6.4}$$

For a waveguide the rate of loss dP/dz can be calculated using a model of the field at the dielectric-metal boundary [14] including the expressions derived in Chapter 5. The result for the TM_{0n} modes of interest here is found to be

$$\frac{\mathrm{d}P}{\mathrm{d}z} = \frac{\omega^3 \delta \epsilon_r^2 \alpha_0}{4\mu_0 \kappa^2 c^4} (Y_1(\kappa b) J_0(\kappa b) - J_1(\kappa b) Y_0(\kappa b))^2. \tag{6.5}$$

where α_0 is the mode parameter as defined in Eq. 5.41 and δ is the skin depth of the metal, defined as

$$\delta = \left(\frac{2}{\mu_0 \omega \sigma} \right)^{1/2}, \tag{6.6}$$

with σ the conductivity of the metal which comprises the coating.

When these calculations are performed for the modes in question and the loss tangent of quartz is taken into account [104] the resulting expected parameters are α_1=40-70 m^{-1} and α_2=327-360 m^{-1}, where the range indicates pure copper for the lower value and pure aluminum for the upper, $\sigma_{Cu} = 5.8 * 10^7$ [S/m] and

$\sigma_{Al} = 3.8 * 10^7$ [S/m]. This range allows exclusion of uncertainly in aluminum thickness as a source of losses which are not accounted for. In the case of the TM_{02} mode the losses are dominated by the loss tangent in the dielectric material.

The sources for discrepancy between the measured and theoretical losses are uncertain. We ignore for a moment the possibilities of systematic errors in the measurement and expound on some observations made during experiment. First, the environment in the experimental chamber in close proximity to the beam is resplendent with radiation sources. In radioactive environments, both silicon dioxide and quartz are subject to conversion from relatively translucent materials to an opaque material which is called "smoky quartz". This is a result of breaking the bonds between the silicon and the oxygen, causing the material to turn black. Traditional uses for quartz and silicon dioxide are as transmissive optics, for such a use smoky quartz is useless and is relatively unstudied. Additionally, as shown in Figure 6.6, the total pulse length is on the oder of 5.5 mm whereas the expected length is 18mm. The apparent abrupt cut-off cannot entirely be attributed to increased loss parameter alone. Finally, the applicability of the Drude model [105] to systems involving very high frequency radiation is not as well understood as for standard radio frequency structures.

6.6.3 Beam Energy Loss

With the modes excited in the structures examined we now move on to an analysis of the energy lost by the beam as it traverses the structure. To reiterate, the histograms that will be shown here are a result of binning the average energy of individual beams.

For this measurement the spectrometer was set to an imaging condition. In the language of Chapter 2 this means that the R_{33} and R_{34} elements are much

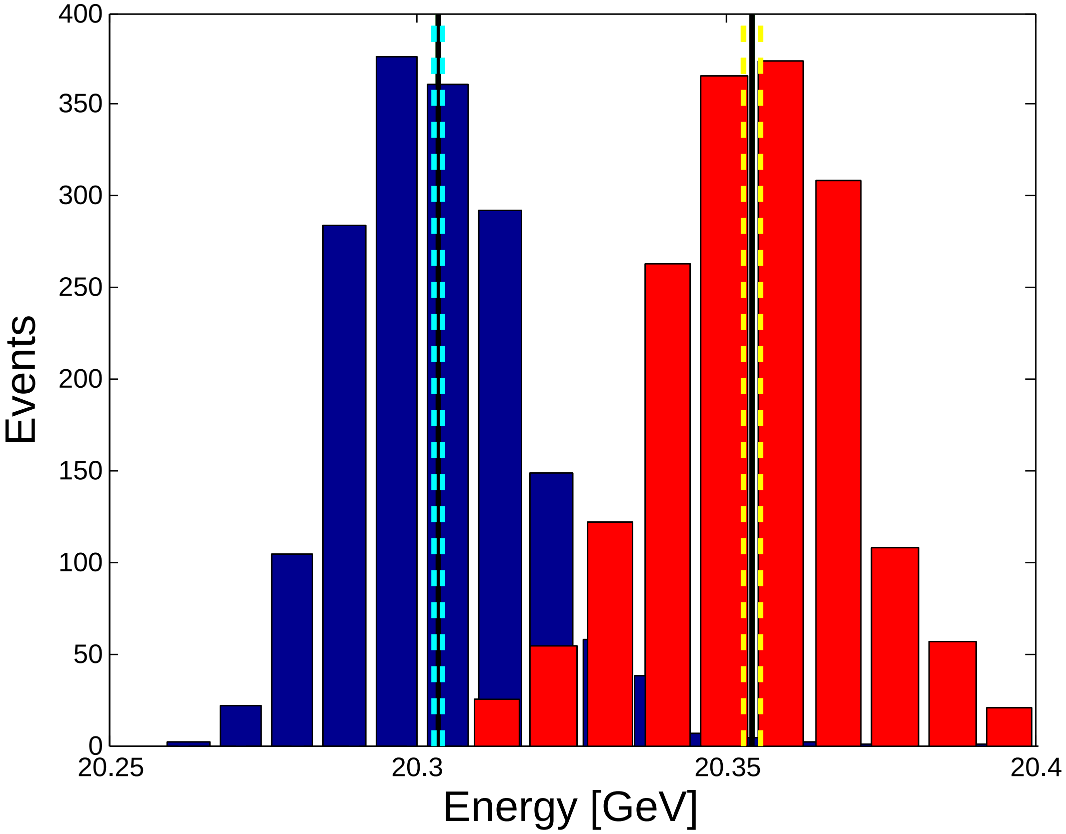

Figure 6.7: A histogram showing the average energy of the electron beam. The blue represents beam centroid energy measurements taken with the structure in the beam path and red represents no structure in the beam path, the difference is 50.9 ± 0.78 MeV . The black lines mark the means of the respective measurements and the yellow dashed lines the 95% confidence interval. The difference between the two data sets is 50.9 ± 0.78 MeV, leading to a total energy loss of 152 ± 2.3 mJ per electron bunch.

smaller than the R_{36} element so that dispersion dominates the beam's position on the spectrometer screen.

We begin with the "transition" structure for which both the CCR spectrum

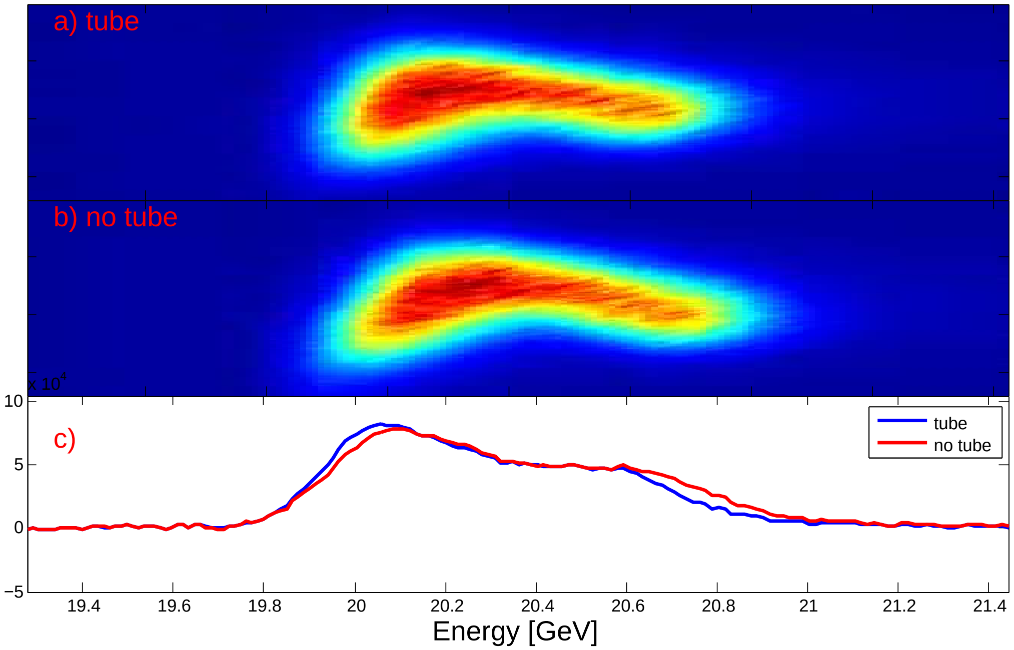

Figure 6.8: Example data showing the electron beam energy profile both with and without the structure. a) shows the beam after having passed through the dielectric waveguide. b) shows the beam with no structure in the beam path. c) shows the projection of the two images on to the energy axis.

and the energy loss can be reasonably expected to be measured. This is the case of a structure made of SiO_2 with parameters a = 450 μm, b = 640 μm and a length of 10 cm. The result of the measurement is shown in Figure 6.7. For this measurement 1400 shots were taken with the structure in the beam path and 1000 without, providing a reference measurement. What we show is an average energy change of 50.9 ± 0.78 MeV, which for a 10 cm long structure corresponds to a decelerating gradient of 509 ± 7.8 MVm^{-1}. If the fundamental theorem of beam loading is applied an accelerating gradient of around 1 GVm^{-1} can be expected. This can be compared with the simulation for such a structure as shown in Figure 5.13 which shows an average decelerating gradient of approximately 509 ± 7.8

MVm^{-1} and a peak accelerating gradient of approximately 1 GVm^{-1}.

The measured energy loss of the beam of 149 mJ is compared with the value expected through simulation and theoretical calculations of 130 mJ. The extra sources of loss are seen to be due to diffraction radiation at the entrance and exit of the structure. Thus the values measured are is close agreement with both simulation and theory.

Figure 6.8 shows an example of what the beam looks like on the spectrometer in both cases. For the examples presented the difference in average energy is 38 MeV. A comparison of the two individual measurements can be used to infer the quality of the beam after transport through the structure. In this case the beam is seen to be virtually unchanged and thus it is safe to say that its emittance has been preserved. Furthermore, information collected at the time from Beam Position Monitors (BPMs) indicates that any deflection of the beam that may have occurred is below measurement capabilities. The measurement system is capable of measuring the beam position to an accuracy of one third of a beam width, or 10 μm.

Next we discuss the measurements made of 15 cm quartz structures with parameters a = 400 μm and b = 600 μm. These structures allow us to make a comparison with the previously measured slighty larger bore structures and still admit relatively easy alignment. They are a step toward very small bore, high field structures. The result of the average, or centroid, energy measurement, as described above, are shown in Figure 6.9. A list of the modes excited and the calculated energy deposited into each mode is show in Table 6.5.

A plot of the calculated wakefield is shown in Figure 6.10. Here we see that, given the bunch length to $\sigma_z = 45$ μm, the wakefield excited is multimode, so that while the peak decelerating gradient is 800 MVm^{-1} the peak accelerating

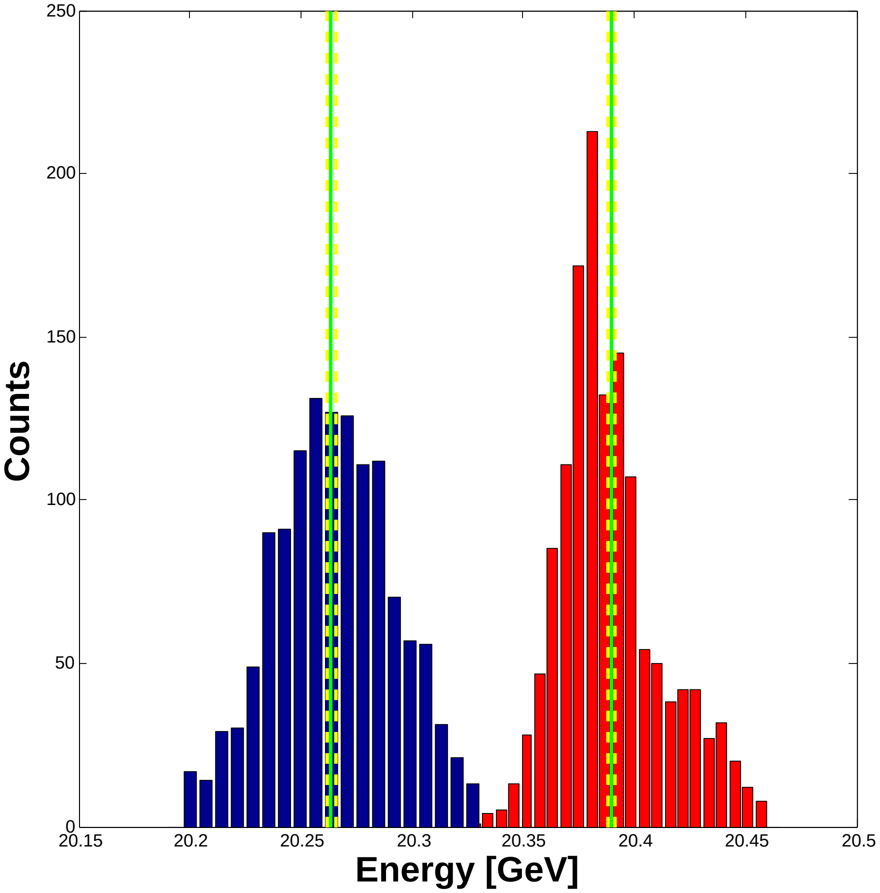

Figure 6.9: A histogram showing the raw average energy of the electron beam with and without the a/b = 400/600 μm structure. The blue represents beam centroid energy measurements taken with the structure in the beam path and red represents no structure in the beam path, the difference is 120 MeV. The black lines mark the means of the respective measurements and the yellow dashed lines the 95% confidence interval. An algorithm that uses BPM data to correct for transverse kicks in the beam indicates a total energy difference of 84 ± 2.34 MeV in 15 cm, which leads to a gradient of 560 ± 15.6 MVm^{-1}.

gradient is expected to be 1.3 GVm^{-1}. The deviation from the *Fundamental Theroem of Beam Loading* is due to the multimode nature of the wakefield. For

Table 6.5: A list of the TM modes excited and the expected energy deposited into each mode for the 400/600 μm, 15 cm experiment.

	TM_{01}	TM_{02}	TM_{03}
λ [μm]	763	267	154
Energy [mJ]	194	47	2.6

each given mode the theorem applies, the combination of modes adds in effects due to wavelength and phase differences.

For this measurement the spectrometer was not set to imaging, due to geometric constraints in the experimental hall. This means that in terms of the transport matrix the elements R_{33} and R_{34} cannot be ignored in favor of R_{36}. Given the nature of the measurement in that we are looking for small changes in average energy of the beam these effects must be taken into account. Quantitatively we can realistically expect beam kicks in the transverse dimension that approach 100 MVm^{-1}, depending on offset, c.f. Eq. 5.69. A relative transverse kick or momentum change of 20 MeV/c for a beam of energy 20.35 GeV/c is an angle y′ of 1 mrad. Thus even a relatively small transverse momentum kick and a modest non-zero R_{34} can lead to large apparent energy shift on the spectrometer.

The transport matrix for the spectrometer for this measurement is found to be

$$R = \begin{pmatrix} -12.72 & 7.134 & 0 & 0 \\ -0.95 & 0.48 & 0 & 0 \\ 0 & 0 & -0.82 & 0.27 \\ 0 & 0 & -0.42 & -1.09 \end{pmatrix}. \tag{6.7}$$

Where this matrix is fashioned as is typical for transport systems, specifically to

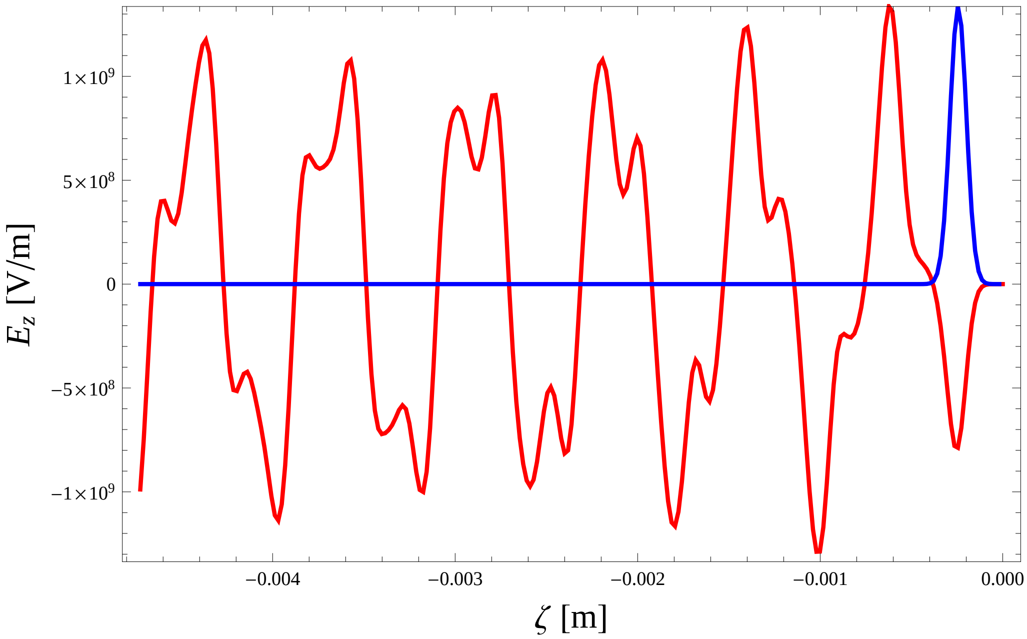

Figure 6.10: The calculated wakefield behind the electron bunch used in the 400/600 μm, 15 cm experiments. The wakefield is shown in red and the electron beam distribution is shown in blue. The electron beam has been scaled to fit the plot. For this measurement the beam had a length of approximately σ_z= 45 μm, short enough to excite the first three TM_{0n} modes. This means that the wakefield behind the electron bunch is subject to interference in the sum of the wake fields so while the decelerating gradient tends to peak of 800 MVm^{-1} and an average of 540 MVm^{-1}, the peak accelerating gradient behind the bunch is expected to be around 1.3 GVm^{-1}.

operate on the the following state vector,

$$\vec{x}_0 = \begin{pmatrix} x \\ x' \\ y \\ y' \end{pmatrix}. \tag{6.8}$$

What we see is that even a very small kick in the $\hat{x}$ direction will be amplified by a factor of 13 in position on the spectrometer. Thusly even small kicks will show up as offsets and more importantly the variation of the forces along the bunch (Equation 5.72) will show up as structure in the $\hat{x}$ direction due to the non-zero R_{12} element. These problems also will present, but to a lesser degree, in the $\hat{y}$ or energy measuring direction.

To account for the systematic difficulty present in this measurement a non-intercepting Beam Position Monitor (BPM) is used to measure the offset of the beam with and without the structure in the beam path. As the BPM is after a dispersive element, the change in its focal properties with energy must also be taken into account. Concretely, we may write the difference in the measured position on the spectrometer screen as

$$x_2 - x_{2,struct} = M_{11}(E_1)x_1 - M_{11}(E_2)x_{1,struct} + M_{12}(E_1)x'_1 - M_{12}(E_2)x'_{1,struct}, \tag{6.9}$$

where the subscript 2 is the position of the beam on the BPM and 1 is the position just after the structure, which is not measured. What is known is that before the structure the beam position is identical in both cases. In this case we represent the transport matrix between the structure and the BPM as M. This is in contrast to the transport matrix from the structure to the spectrometer screen, which is R. This can be incorporated into the analysis via a simple model which takes the motion of the beam in the transverse direction into account.

Solving for the change in angle of the bean after it has traversed the structure gives

$$\begin{aligned} x'_1 - x'_{1,struct} + \frac{M_{11}(E_2)}{M_{12}(E_2)}(x_1 - x_{1,struct}) = \\ \frac{1}{M_{12}(E_2)}(x_2 - x_{2,struct}) + \frac{\Delta M_{11}}{M_{12}(E_2)}(x_1) + \frac{\Delta M_{12}}{M_{12}(E_2)}(x'_1), \end{aligned} \tag{6.10}$$

where

$$\Delta M_{11} \equiv M_{12}(E_2) - M_{12}(E_1), \tag{6.11}$$

with equivalent expressions for the other terms. All that remains is to model the behavior of the beam in the structure. To do so we return to Chapter 5 and note that the forces in the transverse direction are proportional to the offset in that direction. This leads to a relation between the offset x and the angle x′ of $x_{1,struct} = x_0 + (\Delta x'/L)z^2$ in which $\Delta x' = x'_{1,structure} - x'_1$ is the total angle change over the course of the structure and L is the length of the structure. We are then able to perform the substitution $(x_1 - x_{1,struct}) = -\Delta x' L$, which gives,

$$\begin{aligned} x'_1 - x'_{1,struct}\left(1 + \frac{M_{11}(E_2)}{M_{12}(E_2)}L\right) = \\ \frac{1}{M_{12}(E_2)}(x_2 - x_{2,struct}) + \frac{\Delta M_{11}}{M_{12}(E_2)}x_1 + \frac{\Delta M_{12}}{M_{12}(E_2)}x'_1. \end{aligned} \tag{6.12}$$

This then is a function that gives us a measure of the angle and offset after the structure as a measure of only the relative shift in the beam position on the BPM. A further assumption which is made is that the beam is otherwise on the nominal beam trajectory. That is to say that the second and third terms on the right hand side of the above equation can be ignored. It is also noted that the difference between E_1 and E_2 is so small that using the ”uncorrected” value for E_2 or the ”corrected” value makes no difference.

The remaining task is to determine how the usage of the BPM affects the error in the measured energy. This can be done by taking a simple sum of squares of the standard deviations of each measurement [106],

$$\sigma_T = \sqrt{\sigma_E^2 + \sigma_{BPM}^2} \tag{6.13}$$

The contribution due to the BPM, σ_{BPM} is calculated using

$$\sigma_{BPM} = \left| \frac{R_{34}}{M_{12} + LM_{11}} \sigma_{y,BPM} \frac{15}{25} \right| = 23MeV. \tag{6.14}$$

Where $\sigma_{y'}$ is the measured r.m.s. deviation in the position of the beam at the BPM and the fraction 15/25 is the measured calibration of the spectrometer.

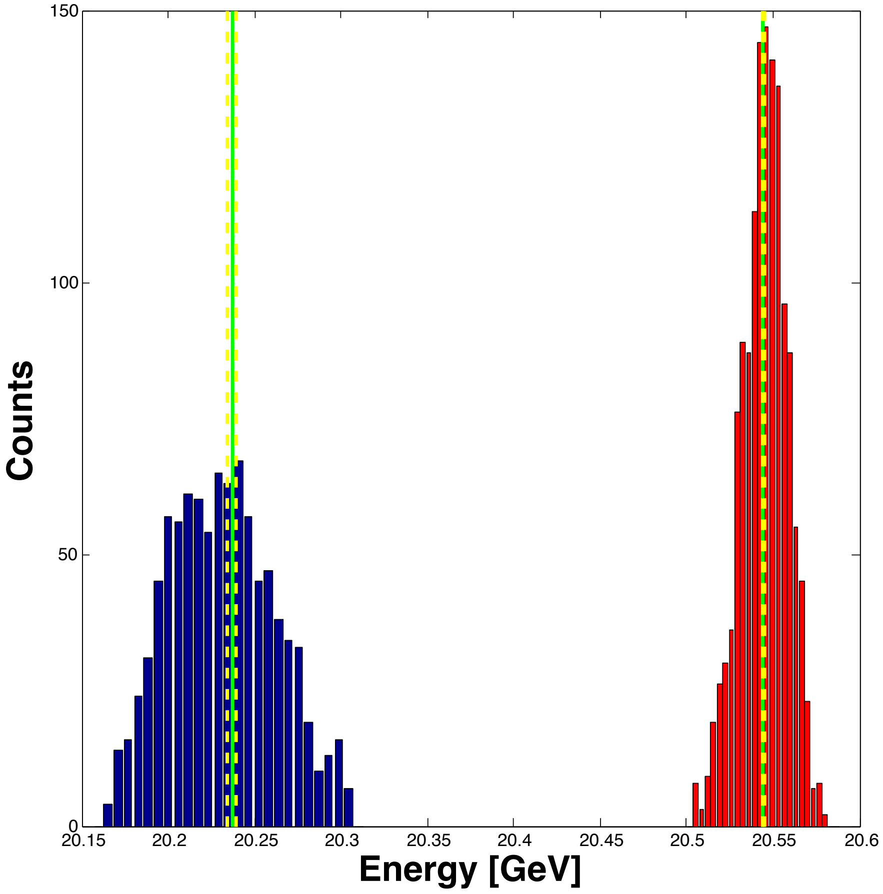

Figure 6.11: A histogram showing the raw average energy of the electron beam with and without the a/b = 300/400 μm structure. The blue represents beam centroid energy measurements taken with the structure in the beam path and red represents no structure in the beam path, the difference is 300 MeV. The black lines mark the means of the respective measurements and the yellow dashed lines the 95% confidence interval. An algorithm that uses BPM data to correct for transverse kicks in the beam indicates a total energy difference of 202 ± 2.97 MeV in 15 cm, which leads to a gradient of 1347 ± 19.8 MVm^{-1}.

This means that the standard deviation of the mean of the histogram, for the case of the beam traveling through the structure, is found to be

$$\frac{\sigma_T}{\sqrt{N}} = \frac{\sqrt{38.3^2 + 23^2}}{\sqrt{N}} = \frac{44.7}{\sqrt{1400}}\, MeV = 1.9\, MeV. \tag{6.15}$$

This is seen to still be extremely small, owing to the number of data points collected. Finally then the measured energy loss of the beam in the structure is found to be 84 ± 2.34 MeV, where the error bars are defined as the 95% confidence interval.

We now turn our attention to the last energy loss measurement made using an a = 300 μm, b = 400 μm structure which is 15 cm long. This data is shown in Figure 6.11. The analysis proceeds identically to that which was just described for the previous structure. In the end we find that the measured gradient is 1347 ± 19.8 MVm^{-1}. This represents a gradient more than 50 times larger than is present in conventional RF accelerators.

Table 6.6: A list of the TM modes excited and the expected energy deposited into each mode for the 300/400 μm, 15 cm experiment.

	TM_{01}	TM_{02}	TM_{03}
λ [μm]	428	140	80
Energy [mJ]	478	140	8

At this point evoking the fundamental theorem of beam loading may seem prudent but the beam used to excite the wakes for the last data set was extremely short, $\sigma_z = 20\ \mu m$. This means that the wakefield contains many modes, so it is difficult to say through rules of thumb what gradient to expect behind the beam. A plot of a simulation of the wakefield is shown in Figure 6.12. What is shown is that the wakefield is multimode and thus subject to destructive interference

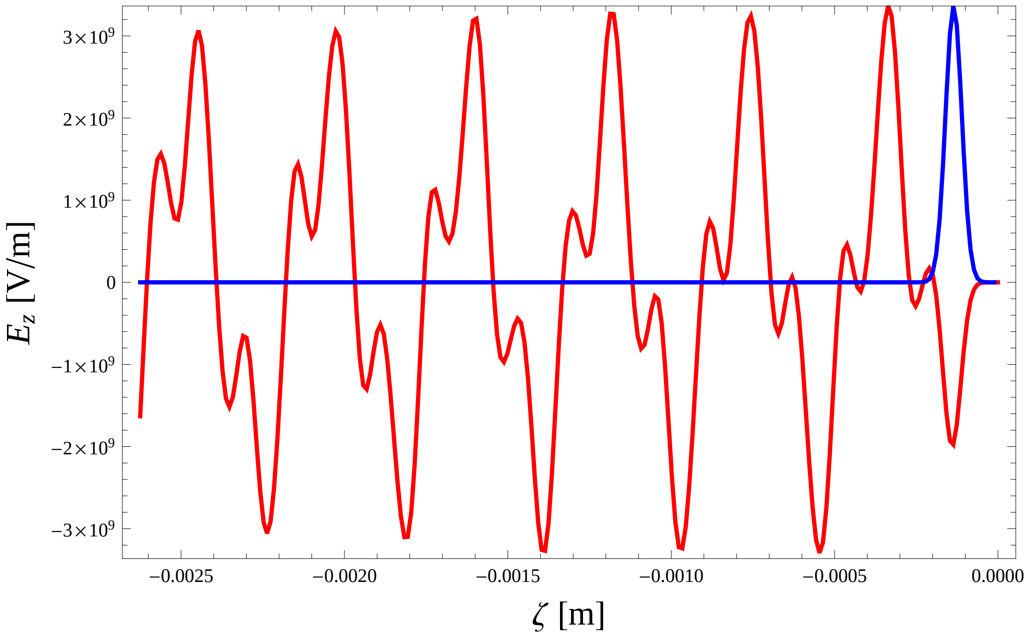

Figure 6.12: The calculated wakefield behind the electron bunch used in the 300/400 μm, 15 cm experiments. The wakefield is shown in red and the electron beam distribution is shown in blue. The electron beam has been scaled to fit the plot. For this measurement the beam had a length of approximately σ_z= 20 μm, short enough to excite the first three TM_{0n} modes. This means that the wakefield behind the electron bunch is subject to interference in the sum of the wake fields so while the decelerating gradient tends to peak of 2 GVm^{-1} and an average of 1.33 GVm^{-1}, the peak accelerating gradient behind the bunch is expected to be around 3 GVm^{-1}.

between the modes. This interference leads to a peak accelerating gradient of 5 GVm^{-1}

Of qualitative interest is the broadening of the jitter in the average energy of the beam. Comparison of the data taken with various structures in the beam path (blue histograms) in Figures 6.7, 6.9, 6.11, shows that as the structures get longer and smaller bore the energy given up by the beam to the wake fields is much more sensitive to variations in the beam parameters. For example, the energy given up is proportional to charge squared with a multiplicative factor which depends on the transverse dimensions of the structure, the coupling factor.

Given the charge of the beam (3 nC) the energy extracted for the smaller bore structures is on the order of 600 mJ. As of the publication of this document the most THz energy measured is approximately 4 mJ, also at FACET. This radiation is produced via transition radiation off a foil, so is inherently broadband, unlike the radiation produced using the structures in these experiments which is quite narrowband, as discussed above.

CHAPTER 7

Conclusion

We have shown here decelerating gradients on the order or 1.35 GV/m. This represents over a 50 fold improvement in sustainable gradient when compared with conventional radio-frequency accelerators. When the *Fundamental Theorem of Beam Loading* is invoked the expected accelerating gradient can be expected to be greater than 2 GV/m. This is seen to be of the order of magnitude of recent plasma based experiments [2, 3] which understandably are creating a great deal of excitement in the field of accelerator physics. The measurements made in this work represent only what is the current step in the evolution of dielectric wakefield accelerators and much remains to be done.

First, the wakefield behind the drive bunch must be probed using a witness bunch. The reconstruction of the wake using a minimum phase approximation is a first, typical advanced acceleration structures do not admit such reconstructions, but the proof of the pudding is in the eating and a direct measurement of the wake potential behind the drive beam is necessary. Furthermore, the use of cylindrical structures in this experiment are seen as a means to an end. In this case we wished to show that dielectric structures can support gradients which make them competitive with other nascent technologies, not necessarily that the geometry used is the best for the job. Slab symmetric and other exotic structures, as discussed earlier, are seen to have very desirable properties. Demonstration of sustained gradients in dielectric structures in excess of a GV/m will hopefully spur investigation of other geometries and increase activities centered around dielectric structures as sources of both high-energy particles and high-energy THz.

The potential applications of the high energy THz possible in the structures described and tested in this work are diverse. Narrowband terahertz sources are "crucial to high-resolution spectroscopy" [107]. The especially high-energy possible in the system presented here is especially after for the investigation of semiconductors [108, 109]. There is, however, much work to be done before such a system as used here could be used experimentally for other work. The absolute energy extracted and transported to a given plane must be measured. More so, the sources of losses must be accounted for before truly large energy THz radiation pulses can be brought to experiments.

APPENDIX A

A.1 Derivation of $A_{2m+1,n}$ Coefficients Recursion Relation

$$\phi_B(x,y,s) = \sum_{m=0}^{\infty}\sum_{n=0}^{\infty} A_{2m+1,n}(s)\frac{x^n}{n!}\frac{y^{2m+1}}{(2m+1)!} \tag{A.1}$$

$$\nabla^2\phi(x,y,s) = \frac{\partial^2\phi}{\partial x^2} + \frac{h}{1+hx}\frac{\partial\phi}{\partial x} + \frac{\partial^2\phi}{\partial y^2} + \frac{1}{(1+hx)^2}\frac{\partial^2\phi}{\partial s^2} - \frac{h^{'}x}{(1+hx)^3}\frac{\partial\phi}{\partial s} = 0 \tag{A.2}$$

$$(1+hx)^3\frac{\partial^2\phi}{\partial x^2} + h(1+hx)^2\frac{\partial\phi}{\partial x} + (1+hx)^3\frac{\partial^2\phi}{\partial y^2} + (1+hx)\frac{\partial^2\phi}{\partial s^2} - h^{'}x\frac{\partial\phi}{\partial s} = 0 \tag{A.3}$$

$$\frac{\partial\phi}{\partial x} = \sum_{m=0}^{\infty}\sum_{n=0}^{\infty} A_{2m+1,n}(s)\frac{x^{n-1}}{(n-1)!}\frac{y^{2m+1}}{(2m+1)!} \tag{A.4}$$

$$\frac{\partial^2\phi}{\partial x^2} = \sum_{m=0}^{\infty}\sum_{n=0}^{\infty} A_{2m+1,n}(s)\frac{x^{n-2}}{(n-2)!}\frac{y^{2m+1}}{(2m+1)!} \tag{A.5}$$

$$\frac{\partial^2\phi}{\partial y^2} = \sum_{m=0}^{\infty}\sum_{n=0}^{\infty} A_{2m+1,n}(s)\frac{x^{n}}{(n)!}\frac{y^{2m-1}}{(2m-1)!} \tag{A.6}$$

$$\frac{\partial\phi}{\partial s} = \sum_{m=0}^{\infty}\sum_{n=0}^{\infty} A^{'}_{2m+1,n}(s)\frac{x^{n}}{(n)!}\frac{y^{2m+1}}{(2m+1)!} \tag{A.7}$$

$$\frac{\partial^2\phi}{\partial s^2} = \sum_{m=0}^{\infty}\sum_{n=0}^{\infty} A^{''}_{2m+1,n}(s)\frac{x^{n}}{(n)!}\frac{y^{2m+1}}{(2m+1)!} \tag{A.8}$$

Proceeding to derive the five pieces of the above Laplacian gives:

$$\begin{aligned} h^{'}x\frac{\partial\phi}{\partial s} &= h^{'}\sum_{m=0}^{\infty}\sum_{n=0}^{\infty} A^{'}_{2m+1,n}(s)\frac{x^{n+1}}{(n)!}\frac{y^{2m+1}}{(2m+1)!} \\ &= nh^{'}\sum_{m=0}^{\infty}\sum_{n=1}^{\infty} A^{'}_{2m+1,n-1}(s)\frac{x^{n}}{(n)!}\frac{y^{2m+1}}{(2m+1)!} \end{aligned} \tag{A.9}$$

If we use the restriction that the coefficients are not allowed to have negative indexes and indexes which produce powers of x or y which are not physical (i.e. $\frac{1}{x}$) we can extend all sums to n=0 and m=0 and write:

$$h^{'}x\frac{\partial\phi}{\partial s} = nh^{'}\sum_{m=0}^{\infty}\sum_{n=0}^{\infty}\left(nh^{'}A^{'}_{2m+1,n-1}(s)\right)\frac{x^n}{(n)!}\frac{y^{2m+1}}{(2m+1)!} \tag{A.10}$$

We can then do the same for all components of the Laplacian.

$$\begin{aligned}(1+hx)\frac{\partial^2\phi}{\partial s^2} &= (1+hx)\sum_{m=0}^{\infty}\sum_{n=0}^{\infty}A^{''}_{2m+1,n}(s)\frac{x^n}{(n)!}\frac{y^{2m+1}}{(2m+1)!}\\ &= \sum_{m=0}^{\infty}\sum_{n=0}^{\infty}\left(A^{''}_{2m+1,n}(s)+nhA^{''}_{2m+1,n-1}(s)\right)\frac{x^n}{(n)!}\frac{y^{2m+1}}{(2m+1)!}\end{aligned} \tag{A.11}$$

$$\begin{aligned}(1+hx)^3\frac{\partial^2\phi}{\partial x^2} &= (1+3hx+3h^2x^2+h^3x^3)\sum_{m=0}^{\infty}\sum_{n=0}^{\infty}A_{2m+1,n}(s)\frac{x^n}{(n)!}\frac{y^{2m+1}}{(2m+1)!}\\ &= \sum_{m=0}^{\infty}\sum_{n=0}^{\infty}\Big(A_{2m+1,n+2}(s)+3hnA_{2m+1,n+1}(s)\\ &+3h^2n(n-1)A_{2m+1,n}(s)+h^3n(n-1)(n-2)A_{2m+1,n-1}(s)\Big)*\\ &\frac{x^n}{(n)!}\frac{y^{2m+1}}{(2m+1)!}\end{aligned} \tag{A.12}$$

$$\begin{aligned}(1+hx)^3\frac{\partial^2\phi}{\partial y^2} &= (1+3hx+3h^2x^2+h^3x^3)\sum_{m=0}^{\infty}\sum_{n=0}^{\infty}A_{2m+1,n}(s)\frac{x^n}{(n)!}\frac{y^{2m-1}}{(2m-1)!}\\ &= \sum_{m=0}^{\infty}\sum_{n=0}^{\infty}\Big(A_{2m+3,n}(s)+3hnA_{2m+3,n-1}(s)\\ &+3h^2n(n-1)A_{2m+3,n-2}(s)+h^3n(n-1)(n-2)A_{2m+3,n-3}(s)\Big)\\ &\frac{x^n}{(n)!}\frac{y^{2m+1}}{(2m+1)!}\end{aligned} \tag{A.13}$$

$$
\begin{aligned}
h(1+hx)^2\frac{\partial\phi}{\partial x} &= h(1+2hx+h^2x^2)\sum_{m=0}^{\infty}\sum_{n=0}^{\infty}A_{2m+1,n}(s)\frac{x^{n-1}}{(n-1)!}\frac{y^{2m+1}}{(2m+1)!}\\
&= \sum_{m=0}^{\infty}\sum_{n=0}^{\infty}\Big(hA_{2m+1,n+1}(s)+2h^2nA_{2m+1,n}(s)\\
&+h^3n(n-1)A_{2m+1,n-1}(s)\Big)\frac{x^n}{(n)!}\frac{y^{2m+1}}{(2m+1)!}
\end{aligned}
\tag{A.14}
$$

Since the Laplacian is defined to be equal to zero, all identical elements from across the above 5 terms can be dropped leaving, after some collection of like coefficients:

$$
\begin{aligned}
&A''_{2m+1,n}+hnA''_{2m+1,n-1}-nh'A'_{2m+1,n-1}+A_{2m+1,n+2}+\\
&\qquad h(3n+1)A_{2m+1,n+1}+h^2n(3n-1)A_{2m+1,n}+h^3n(n-1)^2A_{2m+1,n-1}\\
&+A_{2m+3,n}+3hnA_{2m+3,n-1}+3h^2n(n-1)A_{2m+3,n-2}+h^3n(n-1)(n-2)A_{2m+3,n-3}=0.
\end{aligned}
\tag{A.15}
$$

References

[1] I. Blumenfeld, C. E. Clayton, F.-J. Decker, *et al.*, “Energy doubling of 42 gev electrons in a metre-scale plasma wakefield accelerator,” *Nature*, vol. 445, no. 7129, pp. 741–744, 2007.

[2] M. Litos, E. Adli, W. An, *et al.*, “High-efficiency acceleration of an electron beam in a plasma wakefield accelerator,” *Nature*, vol. 515, no. 7525, pp. 92–95, 2014.

[3] W. Leemans, B. Nagler, A. Gonsalves, *et al.*, “Gev electron beams from a centimetre-scale accelerator,” *Nature physics*, vol. 2, no. 10, pp. 696–699, 2006.

[4] G. Andonian, D. Stratakis, M. Babzien, *et al.*, “Dielectric wakefield acceleration of a relativistic electron beam in a slab-symmetric dielectric lined waveguide,” *Physical review letters*, vol. 108, no. 24, p. 244801, 2012.

[5] G. Andonian, O. Williams, X. Wei, *et al.*, “Resonant excitation of coherent cerenkov radiation in dielectric lined waveguides,” *Applied Physics Letters*, vol. 98, no. 20, p. 202901, 2011.

[6] S. Antipov, C. Jing, M. Fedurin, *et al.*, “Experimental observation of energy modulation in electron beams passing through terahertz dielectric wakefield structures,” *Physical review letters*, vol. 108, no. 14, p. 144801, 2012.

[7] J. Rosenzweig, G. Andonian, P. Bucksbaum, *et al.*, “Teravolt-per-meter beam and plasma fields from low-charge femtosecond electron beams,” *Nuclear Instruments and Methods in Physics Research Section A: Accelerators, Spectrometers, Detectors and Associated Equipment*, vol. 653, no. 1, pp. 98–102, 2011.

[8] C. Joshi and T. Katsouleas, “Plasma accelerators at the energy frontier and on tabletops,” *Physics Today*, vol. 56, no. 6, pp. 47–53, 2003.

[9] T. P. Wangler, *RF Linear accelerators.* John Wiley & Sons, 2008.

[10] C. Geddes, C. Toth, J. Van Tilborg, *et al.*, “High-quality electron beams from a laser wakefield accelerator using plasma-channel guiding,” *Nature*, vol. 431, no. 7008, pp. 538–541, 2004.

[11] D. Mittleman, M. Gupta, R. Neelamani, *et al.*, “Recent advances in terahertz imaging,” *Applied Physics B*, vol. 68, no. 6, pp. 1085–1094, 1999.

[12] C. Sutton, "Accelerators come into focus in dresden," in *Cern Courier*, August 2014.

[13] D. W. Dupen, "The story of stanfords two-mile-long accelerator may 1966," *SLAC*, 1966.

[14] J. D. Jackson, *Classical Electrodynamics, 3rd edition.* Hamilton Printing Company, 1999.

[15] D. S. H. Schmickler and N. Toge, "A multi-tev linear collider based on clic technology: Clic conceptual design report," in *CLIC Conceptual Design Report* (M. Aicheler, P. Burrows, M. Draper, *et al.*, eds.), 2012. CERN-2012-007.

[16] N. Phinney, N. Toge, and N. Walker, "Ilc reference design report volume 3-accelerator," *arXiv preprint arXiv:0712.2361*, 2007.

[17] D. H. Whittum, "Introduction to electrodynamics for microwave linear accelerators," *Proceedings of the US-CERN-Japan School on RF Engineering for Particle Accelerators,(KEK, Tsukuba, to be published), SLAC-PUB-7802*, 1998.

[18] J. Arthur *et al.*, "Linac coherent light source (lcls) conceptual design report," *SLAC-R-593*, 2002.

[19] D. McGinnis, "New design approaches for high intensity superconducting linacs - the new ess linac design," in *Proceeding of the 2014 International Particle Accelerator Conference*, www.jacow.org, 2014.

[20] R. Bonifacio, C. Pellegrini, and L. Narducci, "Collective instabilities and high-gain regime in a free electron laser," *Optics Communications*, vol. 50, no. 6, pp. 373–378, 1984.

[21] R. Tatchyn, J. Arthur, M. Baltay, *et al.*, "Research and development toward a 4.5- 1.5 å linac coherent light source (lcls) at slac," *Nuclear Instruments and Methods in Physics Research Section A: Accelerators, Spectrometers, Detectors and Associated Equipment*, vol. 375, no. 1, pp. 274–283, 1996.

[22] H. N. Chapman, P. Fromme, A. Barty, *et al.*, "Femtosecond x-ray protein nanocrystallography," *Nature*, vol. 470, no. 7332, pp. 73–77, 2011.

[23] W. Ackermann, G. Asova, V. Ayvazyan, *et al.*, "Operation of a free-electron laser from the extreme ultraviolet to the water window," *Nature photonics*, vol. 1, no. 6, pp. 336–342, 2007.

[24] G. R. Neil, C. Behre, S. Benson, *et al.*, "The jlab high power erl light source," *Nuclear Instruments and Methods in Physics Research Section A: Accelerators, Spectrometers, Detectors and Associated Equipment*, vol. 557, no. 1, pp. 9–15, 2006.

[25] M. Tonouchi, "Cutting-edge terahertz technology," *Nature photonics*, vol. 1, no. 2, pp. 97–105, 2007.

[26] M. Thompson, H. Badakov, A. Cook, *et al.*, "Breakdown limits on gigavolt-per-meter electron-beam-driven wakefields in dielectric structures," *Physical review letters*, vol. 100, no. 21, p. 214801, 2008.

[27] J. B. Rosenweig, *Fundamentals of Beam Physics.* Oxford University Press, 2003.

[28] K. Wille, *The Physics of Particle Accelerators.* Oxford, 2000.

[29] A. W. Chao and M. Tigner, *Handbook of Accelerator Physics and Engineering.* World Scientific, 1999.

[30] G. B. Arfken and H. J. Weber, *Mathematical Methods for Physicists, 5th Edition.* Harcourt Academic Press, 2001.

[31] P. Chen, "A possible final focusing mechanism for linear colliders," *Particle Accelerators*, vol. 20, p. 171, 1987.

[32] H. Wiedemann, *Particle accelerator physics*, vol. 2. Springer, 2003.

[33] M. Kardar, *Statistical Physics of Particles.* Cambridge University Press, 2007.

[34] E. Courant and H. Snyder, "Theory of the alternating-gradient synchrotron," *Annals of physics*, vol. 3, no. 1, pp. 1–48, 1958.

[35] H. Wiedemann, *Particle accelerator physics*, vol. 1. Springer, 2003.

[36] A. E. Siegman, "Lasers. mill valley," 1986.

[37] M. L. Ter-Mikaelian, *High-Energy Electromagnetic Processes in Condensed Media.* Interscience Tracts on Physics and Astronomy, No. 29, 1972.

[38] A. W. Chao, K. H. Mess, M. Tigner, and F. Zimmermann, "Handbook of accelerator physics and engineering," *Handbook of Accelerator Physics and Engineering (2nd Edition). Edited by Chao Alexander Wu et al. Published by World Scientific Publishing Co. Pte. Ltd., 2013. ISBN# 9789814415859*, vol. 1, 2013.

[39] M. H. A. Kramer, “La diffusion de la lumire par les atomes,” *Atti. Congr. Int. Fis. Como*, vol. 2, pp. 545–557, 1927.

[40] R. d. Kronig, “On the theory of dispersion of x-rays,” *JOSA*, vol. 12, no. 6, pp. 547–556, 1926.

[41] D. W. Rule and R. B. Fiorito, “Imaging micron-sized beams with optical transition radiation,” in *Accelerator instrumentation*, pp. 315–321, AIP, 1991.

[42] D. W. Rule and R. B. Fiorito, “Beam profiling with optical transition radiation,” *Proc. 1993 Particle Accelerator Conf.*, 1993.

[43] V. L. Ginzburg and V. N. Tsytovich, “Transition radiation and transition scattering-some questions regarding the theory,” *Moscow Izdatel Nauka*, vol. 1, 1984.

[44] V. L. Ginzburg, “Transition radiation and transition scattering,” *Physica Scripta*, vol. 1982, no. T2A, p. 182, 1982.

[45] GRADSHTEYN-RYZHIK, *Tables on integrals, series, and products.* Academic Press, 1965.

[46] M. Castellano, A. Cianchi, G. Orlandi, and V. Verzilov, “Effects of diffraction and target finite size on coherent transition radiation spectra in bunch length measurements,” *Nuclear Instruments and Methods in Physics Research Section A: Accelerators, Spectrometers, Detectors and Associated Equipment*, vol. 435, no. 3, pp. 297–307, 1999.

[47] S. Casalbuoni, B. Schmidt, P. Schmüser, T. Collaboration, *et al.*, “Far-infrared transition and diffraction radiation part i: Production, diffraction effects and optical propagation,” Tech. Rep. TESLA Report 2005-15, Citeseer, 2005.

[48] S. Casalbuoni, B. Schmidt, P. Schmüser, T. Collaboration, and B. Steffen, “Far-infrared transition and diffraction radiation part ii: The thz beamline at the vuv-fel linac,” Tech. Rep. TESLA-FEL 2006-04, Citeseer, 2006.

[49] J. V. Jelley, “Cerenkov radiation and its applications,” *British Journal of Applied Physics*, vol. 6, no. 7, p. 227, 1955.

[50] J. V. Jelley, *Cerenkov radiation and its applications.* Pergamon Press, 1958.

[51] M. Abele, “The cerenkov effect in optics and in the microwave region,” *Nuovo Cimento*, vol. 9, no. suppl 3, pp. 207–213, 1952.

[52] I. Frank and I. Tamm, “Coherent visible radiation from fast electrons passing through matter,” *CR Acad. Sci. USSR*, vol. 14, pp. 109–114, 1937.

[53] R. Ischebeck, M. Berry, I. Blumenfeld, *et al.*, “A meter-scale plasma wakefield accelerator,” in *AIP Conference Proceedings*, vol. 877, p. 3, IOP INSTITUTE OF PHYSICS PUBLISHING LTD, 2007.

[54] D. R. Nicholson, *Introduction to Plasma Theory.* John Wiley & Sons, Inc, 1983.

[55] H. Ferwerda, B. Hoenders, A. Walther, *et al.*, *Inverse source problems in optics.* Springer, 1978.

[56] J. S. Toll, “Causality and the dispersion relation: logical foundations,” *Physical Review*, vol. 104, no. 6, p. 1760, 1956.

[57] M. V. Klibanov, P. E. Sacks, and A. V. Tikhonravov, “The phase retrieval problem,” *Inverse problems*, vol. 11, no. 1, p. 1, 1995.

[58] E. J. Akutowicz, “On the determination of the phase of a fourier integral, i,” *Transactions of the American Mathematical Society*, pp. 179–192, 1956.

[59] E. J. Akutowicz, “On the determination of the phase of a fourier integral, ii,” *Proceedings of the American Mathematical Society*, vol. 8, no. 2, pp. 234–238, 1957.

[60] R. Lai and A. Sievers, “Phase problem associated with the determination of the longitudinal shape of a charged particle bunch from its coherent far-ir spectrum,” *Physical Review E*, vol. 52, no. 4, p. 4576, 1995.

[61] R. Lai and A. Sievers, “On using the coherent far ir radiation produced by a charged-particle bunch to determine its shape: I analysis,” *Nuclear Instruments and Methods in Physics Research Section A: Accelerators, Spectrometers, Detectors and Associated Equipment*, vol. 397, no. 2, pp. 221–231, 1997.

[62] T. J. Maxwell, C. Behrens, Y. Ding, *et al.*, “Coherent-radiation spectroscopy of few-femtosecond electron bunches using a middle-infrared prism spectrometer,” *Phys. Rev. Lett.*, vol. 111, p. 184801, Oct 2013.

[63] S. I. Bajlekov, M. Heigoldt, A. Popp, *et al.*, “Longitudinal electron bunch profile reconstruction by performing phase retrieval on coherent transition radiation spectra,” *Phys. Rev. ST Accel. Beams*, vol. 16, p. 040701, Apr 2013.

[64] R. Trebino, K. W. DeLong, D. N. Fittinghoff, *et al.*, "Measuring ultrashort laser pulses in the time-frequency domain using frequency-resolved optical gating," *Review of Scientific Instruments*, vol. 68, no. 9, pp. 3277–3295, 1997.

[65] A. A. Michelson and E. W. Morley, "On the relative motion of the earth and the luminiferous ether," *American journal of science*, no. 203, pp. 333–345, 1887.

[66] J. Miao, D. Sayre, and H. Chapman, "Phase retrieval from the magnitude of the fourier transforms of nonperiodic objects," *JOSA A*, vol. 15, no. 6, pp. 1662–1669, 1998.

[67] S. Smale *et al.*, "The fundamental theorem of algebra and complexity theory," *Bull. AMS*, vol. 4, no. 1, 1981.

[68] H. Stark, *Image recovery: theory and application.* Elsevier, 1987.

[69] J. Fourier, *Theorie analytique de la chaleur, par M. Fourier.* Chez Firmin Didot, père et fils, 1822.

[70] E. C. Titchmarsh, *Introduction to the theory of Fourier integrals.* Clarendon Press Oxford, 1948.

[71] H. Nussenzveig, "Phase problem in coherence theory," *Journal of Mathematical Physics*, vol. 8, no. 3, pp. 561–572, 1967.

[72] N. Solyak *et al.*, "Gradient limitations in room temperature and superconducting acceleration structures," in *AIP Conf. Proc*, vol. 1086, pp. 365–372, 2009.

[73] P. B. Wilson, "High energy electron linacs: Applications to storage ring rf systems and linear collider," *SLAC-PUB-2884*, Nov 1991.

[74] W. K. H. Panofsky and W. A. Wenzel, "Some considerations concerning the transverse deflection of charged particles in radio-frequency fields," *Rev. Sci. Instrum.*, vol. 27, p. 967, July 1956.

[75] B. O'Shea, J. Rosenzweig, S. Barber, *et al.*, "Transformer ratio improvement for beam based plasma accelerators," *AIP Conference Proceedings*, vol. 1507, no. 1, pp. 606–611, 2012.

[76] K. L. Bane, P. B. Wilson, and T. Weiland, "Wake fields and wake field acceleration," tech. rep., Stanford Linear Accelerator Center, CA (USA), 1984.

[77] J. B. Rosenzweig, *Plasma Wake-fields in High Energy Physics: An Experimental and Theoretical Investigation.* PhD thesis, University of Wisconsin, Madison, 1988.

[78] G. Andonian. Private Communication.

[79] K. L. Bane, P. Chen, and P. Wilson, "Collinear wake field acceleration," tech. rep., Stanford Linear Accelerator Center, CA (USA), 1985.

[80] J. R. Carson, S. P. Mead, and S. A. Schelkunoff, "Hyper?frequency wave guides—mathematical theory," *Bell System Technical Journal*, vol. 15, no. 2, pp. 310–333, 1936.

[81] C. Chang and J. W. Dawson, "Propagation of Electromagnetic Waves in a Partially Dielectric Filled Circular Waveguide," *Journal of Applied Physics*, vol. 41, no. 11, pp. 4493–4500, 1970.

[82] A. Cook, *Generation of Narrow-Band Terahertz Coherent Cherenkov Radiation in a Dielectric Wakefield Structure.* PhD thesis, University of California, Los Angeles, 2009.

[83] R. Keinings and M. E. Jones, "The cherenkov wakefield accelerator," *Part. Accel.*, vol. 24, pp. 223–229, 1989.

[84] H. Eom, "Electromagnetic wave theory for boundary-value problems," *Springer, NewYork NY*, vol. 2, p. 4, 2004.

[85] S. Park and J. Hirshfield, "Theory of wakefields in a dielectric-lined waveguide," *Physical Review E*, vol. 62, no. 1, p. 1266, 2000.

[86] J. Power, W. Gai, and P. Schoessow, "Wakefield excitation in multimode structures by a train of electron bunches," *Physical Review E*, vol. 60, no. 5, p. 6061, 1999.

[87] A. W. Chao, *Physics of collective beam instabilities in high energy accelerators.* Wiley, 1993.

[88] J. Lim, P. Frigola, G. Travish, *et al.*, "Adjustable, short focal length permanent-magnet quadrupole based electron beam final focus system," *Physical Review Special Topics-Accelerators and Beams*, vol. 8, no. 7, p. 072401, 2005.

[89] A. Tremaine, J. Rosenzweig, and P. Schoessow, "Electromagnetic wake fields and beam stability in slab-symmetric dielectric structures," *Physical Review E*, vol. 56, no. 6, p. 7204, 1997.

[90] X. E. Lin, "Photonic band gap fiber accelerator," *Physical Review Special Topics-Accelerators and Beams*, vol. 4, no. 5, p. 051301, 2001.

[91] B. Cowan, "Photonic crystal laser-driven accelerator structures," in *Particle Accelerator Conference, 2005. PAC 2005. Proceedings of the*, pp. 731–733, IEEE, 2005.

[92] G. Andonian, "Bragg experiment," *TBD*, vol. 1, no. 1, p. 1, 2012.

[93] S. Wolfram, *The mathematica book.* Wolfram Media, Incorporated, 1996.

[94] M. U. Guide, "The mathworks," *Inc., Natick, MA*, vol. 5, 1998.

[95] C. Nieter and J. R. Cary, "Vorpal: a versatile plasma simulation code," *Journal of Computational Physics*, vol. 196, no. 2, pp. 448–473, 2004.

[96] M. Hogan, T. Raubenheimer, A. Seryi, *et al.*, "Plasma wakefield acceleration experiments at facet," *New Journal of Physics*, vol. 12, no. 5, p. 055030, 2010.

[97] Z. Wu, A. S. Fisher, J. Goodfellow, *et al.*, "Intense terahertz pulses from slac electron beams using coherent transition radiation," *Review of Scientific Instruments*, vol. 84, no. 2, p. 022701, 2013.

[98] J. Rosenzweig, E. Arab, G. Andonian, *et al.*, "The galaxie all-optical fel project," in *ADVANCED ACCELERATOR CONCEPTS: 15th Advanced Accelerator Concepts Workshop*, vol. 1507, pp. 493–498, AIP Publishing, 2012.

[99] R. C. Weast, M. J. Astle, and W. H. Beyer, *CRC handbook of chemistry and physics*, vol. 69. CRC press Boca Raton, FL, 1988.

[100] C. R. Grovenor *et al.*, *Materials for semiconductor devices.* Institute of Metals London;, 1987.

[101] J. Rolfe *et al.*, "Long ionisation chamber system for the slc," tech. rep., SLAC-PUB-4925, 1989.

[102] P. B. Wilson, "Introduction to wakefields and wake potentials," tech. rep., Stanford Linear Accelerator Center, Menlo Park, CA (USA), 1989.

[103] D. M. Pozar, *Microwave engineering.* John Wiley & Sons, 2009.

[104] D. Grischkowsky, S. Keiding, M. v. Exter, and C. Fattinger, "Far-infrared time-domain spectroscopy with terahertz beams of dielectrics and semiconductors," *JOSA B*, vol. 7, no. 10, pp. 2006–2015, 1990.

[105] M. Ordal, L. Long, R. Bell, *et al.*, "Optical properties of the metals al, co, cu, au, fe, pb, ni, pd, pt, ag, ti, and w in the infrared and far infrared," *Applied Optics*, vol. 22, no. 7, pp. 1099–1119, 1983.

[106] P. R. Bevington and D. K. Robinson, *Data reduction and error analysis for the physical sciences*, vol. 336. McGraw-Hill New York, 1969.

[107] B. Ferguson and X.-C. Zhang, "Materials for terahertz science and technology," *Nature materials*, vol. 1, no. 1, pp. 26–33, 2002.

[108] M. C. Hoffmann, J. Hebling, H. Y. Hwang, K.-L. Yeh, and K. A. Nelson, "Thz-pump/thz-probe spectroscopy of semiconductors at high field strengths [invited]," *JOSA B*, vol. 26, no. 9, pp. A29–A34, 2009.

[109] R. Huber, F. Tauser, A. Brodschelm, *et al.*, "How many-particle interactions develop after ultrafast excitation of an electron–hole plasma," *Nature*, vol. 414, no. 6861, pp. 286–289, 2001.